THERMAL MODULATION OF MICROFABRICATED CANTILEVER-BASED CHEMICAL SENSORS FOR IMPROVED SELECTIVITY

A Dissertation
Presented to
The Academic Faculty

By

Patrick T. Getz

In Partial Fulfillment
of the Requirements for the Degree
Doctor of Philosophy in the
School of Electrical and Computer Enineering

Georgia Institute of Technology
May 2018

THERMAL MODULATION OF MICROFABRICATED CANTILEVER-BASED CHEMICAL SENSORS FOR IMPROVED SELECTIVITY

Approved by:

Dr. Oliver Brand, Advisor
School of Electrical and Computer Engineering
Georgia Institute of Technology

Dr. Azadeh Ansari
School of Electrical and Computer Engineering
Georgia Institute of Technology

Dr. F. Levent Degertekin
School of Electrical and Computer Engineering
Georgia Institute of Technology

Dr. Todd Sulchek
School of Mechanical Engineering
Georgia Institute of Technology

Dr. A. Fatih Sarioglu
School of Electrical and Computer Engineering
Georgia Institute of Technology

Date Approved: February 19, 2018

Around here, however, we don't look backwards for very long. We keep moving forward, opening up new doors and doing new things, because we're curious...and curiosity keeps leading us down new paths.

Walt Disney

A good engineer is always a wee bit conservative, at least on paper.

Montgomery Scott

To my parents, to whom I am eternally grateful for their love and support.

ACKNOWLEDGEMENTS

I, first and foremost, would like to express my gratitude to Dr. Oliver Brand for his unwavering encouragement and support as my adviser. It is because of his guidance, patience, correction, encouragement and advice that I have grown throughout my PhD. I consider myself very fortunate and blessed to be a part of his group.

I would like to thank Dr. Levent Degertekin, Dr. Fatih Sarioglu, Dr. Azadeh Ansari and Dr. Todd Sulchek for taking the time to serve on my thesis committee. I appreciate the time they have invested in reviewing my work and providing advice.

This work would not have been possible without the cleanroom staff at the Georgia Tech Institute for Electronics and Nanotechnology. I would especially like to thank Gary Spinner, Tran-Vinh Nguyen, Thomas Averette-Johnson, Dr. Mikkel Thomas, Richard Schafer, Dr. Chris (Yeyuan) Yang, Eric Woods, Todd Walters, and Dean Sutter. Without their hard work and support, the tools and processes in the cleanroom would cease to function and the research that it enables would come to a halt.

As my former mentor in the lab, I would like to thank Dr. Christopher Carron for his wise training and guidance in the cleanroom, lab and outside the lab. I am also grateful for Choong-soon Kim's work on redesigning the closed-loop resonant board. My deepest gratitude to all lab group members, Dr. Jin-Jyh Su, Dr. Christopher Carron, Dr. Spyridon Pavlidis, Hommood Alrowais, Choong-soon Kim, Mingu Kim and Devin Brown, for their support, advice, ideas and help.

Special thanks to Purnima Sharma for her help managing the day-to-day administrative work within the lab, without her help many tasks would be impossible. I also thank Bob Rose and Paul Turgeon for their assistance keeping the lab in working order and preventing the ceiling from falling down.

I would also like to thank the many users of the cleanroom, who I have interacted with, for their help and support, especially when procedures do not go as planned. I would

especially like to thank Dr. Harley Hayden and Mason Chilmonczyk for their assistance with various tools in the cleanroom.

I have been blessed to have had many close friendships while pursuing my PhD, all of whom helped keep me grounded and having fun throughout my studies. My adventurous friends with whom I have explored the trails, canals, swamps and caves of the South including Dr. Alicia Cutler, Brandon Carroll, Robert Frost Jr., William Johnson and Dr. Devin Butler; the ”Red Robin crew” comprising of Dr. Connie Arthur, Alex Kimble and Victoria Getz; and friends who have consistently supported me including Sara Lewis, Bryan Blankenagel, Omar Valverde, Thomas Kwok and Greg Chipman.

Most importantly, I would like to thank my family for their love, support and encouragement. My wonderful parents, who have raised me to be the person that I am today and taught me how to better myself for tomorrow. I am deeply grateful for everything that they have done for me and my siblings, who are my best friends, throughout our lives. Finally, I could never fully express my love and appreciation to my wife, Victoria Getz, for her ever-cheerful, loving support.

TABLE OF CONTENTS

LIST OF TABLES

LIST OF FIGURES

LIST OF ABBREVIATIONS

μGC micro-gas chromatography.

ACGIH American Conference of Governmental Industrial Hygienists.

BOE buffered oxide etch.

BOX buried oxide.

BTX benzene, toluene and xylene.

CMOS Complementary metal-oxide-semiconductor.

DRIE deep reactive-ion etch.

EPA Environmental Protection Agency.

GC gas chromatography.

GC-MS gas chromatography-mass spectroscopy.

IC integrated circuit.

ICP inductively coupled plasma.

LOD limit of detection.

MEMS microelectromechanical systems.

MS mass spectroscopy.

NEMS nanoelecromechanical systems.

NIOSH National Institute for Occupational Safety and Health.

OECD Economic Co-operation and Development.

OSHA Occupational Safety and Health Administration.

OV-1 dimethylsilicone gum.

PCA principal component analysis.

PECVD plasma-enhanced chemical vapor deposition.

PIB poly(isobutylene).

ppb parts per billion.

ppm parts per million.

ppt parts per trillion.

Q-factor quality factor.

SAW surface acoustic wave.

SINR signal-to-interference-plus-noise ratio.

SOI silicon on insulator.

VOC volatile organic compound.

LIST OF SYMBOLS

C Analyte concentration in the sensing film.

C_A Analyte concentration in gas phase.

D Fick's law diffusivity coefficient.

D_0 Diffusion rate constant for the polymer-analyte pair.

E Apparent activation energy for an Arrhenius relationship.

f Resonance frequency.

Δf_{min} Minimum detectable frequency shift.

ΔH_{Mix} Enthalpy of mixing.

ΔH_{Vap} Enthalpy of vaporization.

K Partition coefficient.

K_{eff} Effective spring constant of a resonant structure.

M Sensor mass change per unit surface area.

m_a Analyte mass.

M_{eff} Effective mass of a resonant structure.

M_∞ Sensor mass change per unit surface area at equilibrium.

R Gas constant, 8.314 J/(mol K).

S Chemical sensor sensitivity.

τ Analyte characteristic diffusion time constant in a sensing film.

T_B Analyte boiling temperature.

SUMMARY

Microelectromechanical systems (MEMS)-based chemical sensors are becoming an increasingly popular platform for portable and low-power chemical detection as an inexpensive alternative to larger, bench-top systems. This work investigates the integration of heaters on polymer-coated, microfabricated mass-sensitive resonant cantilever sensors for gas-phase chemical detection of volatile organic compounds (VOCs). Because polymer sensing films are only partially selective to any analyte, with each analyte-polymer pair having specific partition and diffusion coefficients, previous sensors relying on analyte absorption into the polymer sensing film, at fixed temperatures (typically ambient), as a method for analyte discrimination face inherent uncertainty. Thus, this work aims to develop a novel resonant-cantilever sensing system through the analysis of sorption kinetics at different temperatures to discriminate between similar analytes.

This thesis demonstrates that temperature control of a sensing film can indeed be used on a microfabricated sensor to discriminate between analytes. Heating pulses applied to the resonant structures cause an estimated 3 °C to 30 °C rise in the sensing film temperature and, thus, a change in partition coefficient and diffusion coefficient. Two aspects of the sorption kinetics and system analysis are considered: 1) the steady-state frequency shifts and 2) the transient response.

In the first task, the influence of the vaporization enthalpy, a known physical property for each analyte, on the heated steady-state sensor response is shown to provide distinct discriminatory ability for the chemical sensor system. The system responses to multiple analytes, with vaporization enthalpies ranging from 31 kJ/mol to 42 kJ/mol, are measured and successfully distinguished. Moreover, an OV-1-coated device successfully measures the vaporization enthalpy of benzene, toluene and o-xylene with an average error of less than 1%.

The second task shows that diffusion coefficients as a function of temperature can be extracted from the signal transients, yielding an Arrhenius-type relationship whose coefficients can be used for analyte discrimination.

Pursuant to these tasks, this thesis also demonstrates improved frequency stability, in the presence of environmental variations, through decreases in the Allan deviations, thus, improving the limits of detection (665 ppb for benzene, 158 ppb for toluene and 41 ppb for o-xylene) of the polymer-coated mass-sensitive sensors. To counteract the effects of self-heating on the sensor output (not related to analyte absorption), methods to remove the effect of self-heating are presented and successfully decrease the impact of a 600 Hz frequency shift from self-heating to less than 10 Hz.

Finally, this thesis shows that the data acquired with this novel application of heating pulses can be successfully used as an input for machine learning to generate classification predictors, leading to analyte discrimination, independent of analyte concentration.

CHAPTER 1
INTRODUCTION

1.1 Motivation

Chemical sensors are pervasive in modern society, providing information about pollutants in the air [1, 2], water quality [3, 4], various health factors obtained from exhaled breath and blood samples [5–9], and the presence of explosives or drugs at security checkpoints [10, 11]. The International Union of Pure and Applied Chemistry defines a chemical sensor as "a device that transforms information, ranging from the concentration of a specific sample component to total composition analysis, into an analytically useful signal. The chemical information, mentioned above, may originate from a chemical reaction of the analyte or from a physical property of the system investigated" [12]. VOCs are common pollutants from manufacturing and consumer industries (contained in potable water, building materials, adhesives, paints, and clothing) [13, 14] and are a by-product of many biological pathways [7, 8, 15], making a quantitative analysis of their presence in many samples imperative. Thus, VOCs constitute one of the main classes of analytes in the aforementioned applications for chemical sensors.

In the presence of sunshine, VOCs react with nitrous oxide to form ozone and smog [16]. Emission reports from members of the Organization for Economic Co-operation and Development (OECD) show an estimated steady decline of VOC emissions, from 40 teragrams in 1990 to about 25 teragrams in 2014 [17]. However, many emission reports are built off of models, due to a lack of field-sampled data [18]. This can lead to inaccuracies in policy making and efforts to combat pollution worldwide. Despite the declining emissions from reporting OECD nations, new emissions from countries such as China and India have grown and are expected to continually increase with the construction of megacities [19].

Figure 1.1: *A group of tourists is shown taking a photograph against a printed background instead of the polluted scenery in China. Volatile organic compounds can react with nitrous oxide to form the visible smog. Growing volatile organic compound emissions, especially in industrial countries, contribute towards degrading air quality across the globe.* © *Nature Publishing Group, reprinted with permission*

China's estimated emission output of 30 teragrams in 2014 is expected to grow exponentially without modifications to existing regulations, which would dwarf reductions made by OECD reporting nations. Understanding the impacts of these emissions on the environment requires advances in sensor technology to acquire concentrations of various chemicals from locations previously unreachable due to sensor cost and portability limitations [20].

Not only are VOCs common pollutants, they also present health and safety hazards [21, 22]. Indoor concentrations of various VOCs can exceed outdoor levels by up to five times [14] and in newly constructed buildings the concentrations can be an order of magnitude greater than older buildings due to volatile organics in construction materials degassing. Prolonged exposure to even low levels of volatile organics in an indoor or outdoor setting has been linked to cancer and other adverse health effects [21, 23–25]. An estimated 3.3 million people die prematurely from outdoor air pollution each year, and this number could double by 2050 if emissions continue their current trend [19]. Of the 3.3 million premature deaths due to pollution each year, China and India account for 1,360,000 and 645,000

respectively. In China, besides the outdoor pollution being 10-100 times higher than in European and North American countries (seen in Figure 1.1), the indoor pollution levels are 100-1000 times greater than their equivalent European homes [20].

The United States Occupational Safety and Health Administration (OSHA), National Institute for Occupational Safety and Health (NIOSH), and the American Conference of Governmental Industrial Hygienists (ACGIH) regulate exposure and set safety limits for various air contaminants in the US workplace [22, 26], with the Environmental Protection Agency (EPA) setting guidelines on how to test for indoor pollutants [27]. Table 1.1 summarizes a few of these VOC limits [26]. Similar to environmental monitoring, current in-situ detection for the workplace or other indoor settings is limited as equipment is expensive, limited in portability, or lacks selectivity [22, 28].

Passive sampling is a key component to studies on volatile organic pollution's effect on health, as it allows researchers inexpensive means to reach otherwise inaccessible locations. However, this sampling methodology cannot detect an acute exposure and its corresponding risk assessment [24]. Thus, active sensors are required [36], but must be provided via technologies that overcome traditional limits with respect to detection limit, selectivity and stability in a cost effective manner. Typically, gas chromatography (GC) units are utilized to measure the concentrations of VOCs. While this technology has existed for over 50 years [37, 38], its application outside of a controlled environment is limited [28].

Table 1.1: *United States VOC safety limits from various regulatory agencies. Data acquired from [26].*

Compound	NIOSH Limit (ppm)	ACGIH Limit (ppm)	OSHA Limit (ppm)
Toluene [29]	100	20	200
Xylene [30]	100	100	100
Pentane [31]	120	600	1000
Hexane [32]	500	50	500
Ethyl Benzene [33]	100	20	100
Chloroform [34]	2	10	50
Benzene [35]	0.1	0.5	1

1.2 Survey of Volatile Organic Compound Detection Methods

A wide variety of transduction mechanisms have been explored for chemical sensors, with a variety of trade-offs that optimize their performance for different analytes or chemical species of interest [39]. These transduction mechanisms either utilize surface or bulk interactions of the analytes with the sensor [40–42] and typically fall under one of four categories: thermal, mass, electrochemical, or optical [43, 44]. The interaction mechanisms and types limit the sensitivity, selectivity, and stability of the device and set the limit of detection (LOD) for the particular analyte or chemical species of interest [12].

Figure 1.2 shows a typical transduction mechanism for converting a chemical signal to a readable output. Analyte in the gas phase is evenly distributed within air or another surrounding medium. A sensitive layer ad/absorbs this chemical to the sensor where chemical or physical properties of the analyte are transduced by the sensor into a readable output. This measurement can be displayed directly to a user, used as an input in a control loop, or stored for future processing as a digital signal.

Trends towards mobile and remote applications limit the available resources (e.g. power, size, time), while generally increasing the noise and interference sources [46]. Device arrays of partially selective sensors form complex analytical tools that overcome fundamental limits of single sensor systems [47]; however, increasing the selectivity of single elements

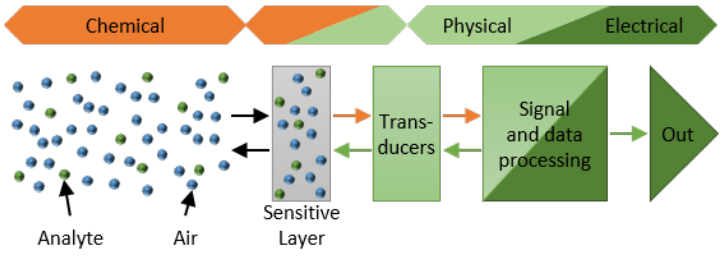

Figure 1.2: *A transduction diagram for chemical gas detection. Analyte diffuses through a carrier gas to the surface of the absorbing film. Diffusion into the sensing film transduces the chemical concentration into a new energy domain, which the sensor can sample and convert into an electrical signal for logging, and downstream processing. Adapted from [45].*

within a sensing system remains a crucial component towards developing accurate and precise measurements of the chemical and biological environment.

1.2.1 Traditional Detection

The standard measurement system for low concentration, parts per million (ppm) and below, detection of VOCs is gas chromatography [48–51]. This system can be coupled with a variety of detectors to meet application requirements. Typically, the detector utilizes mass spectroscopy (MS) [10, 52–54] and/or flame ionization techniques to achieve the detection of target molecules at low concentrations [55, 56]. The limit of detection for these systems varies by analyte from parts per trillion (ppt) to parts per billion (ppb). For analytes at concentrations below the limit of detection solid-phase micro-extraction techniques and pre-concentrators are used to temporarily increase the concentration of trace analytes to above the detection limits [50]. Additional detectors added to the gas chromatography-mass spectroscopy (GC-MS) system further increase the analytical discrimination ability, e.g. proton-transfer-reaction time-of-flight MS has demonstrated low ppt sensitivities with high selectivity [57].

While the performance of GC systems has improved drastically since their invention in 1952 [37], the operating principle remains relatively unchanged. A carrier gas transports an injected sample through a drift column (maintained at a constant temperature), spacing the different chemicals in the column over time based on their drift coefficients, to the detector. This laboratory standard system still requires large footprints and budgets to operate [38, 58]. As even the newest gas chromatography systems from Agilent Technologies (see Figure 1.3b) require a stable environment, carrier gases in the form of gas cylinders, and a reliable power supply [59], samples must be brought into a lab for testing, removing point-of-care or in-situ testing options [60]. For in-situ environmental monitoring, absorption tubes are placed in test locations to sample analyte concentrations. While providing accurate long-term averages, these systems cannot resolve sudden changes in an-

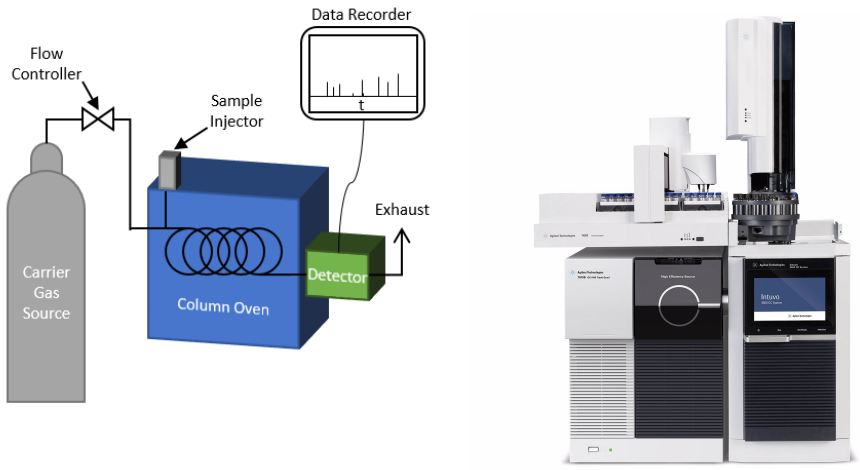

Figure 1.3: *(a) Schematic diagram of a GC system. The carrier gas source, stored in a high pressure canister, provides a supply of gas to the system. The mass flow controller sets the carrier gas flow rate through the column. The chemical species from a sample mixture, injected through the sample injector, are separated in their timing at the detector by their differing drift velocities. (b) A modern gas chromatography coupled with mass spectrometer system for use in forensics, pharmacology, food processing, and environmental monitoring Agilent Technologies.*

alyte concentration. Thus, any change during the course of a measurement is diluted by the long-term averaging. While many applications require the ppb detection that traditional lab based testing methods enable [50], some applications with more relaxed limits of detection or stability requirements allow for the introduction of less expensive and more portable sensors [61].

Microfabrication technologies are reducing the footprint of these, traditionally large, devices into much smaller microsystems. μGC has begun to show promising results towards replacing GC systems for some applications [62–64]. However, full portability and ease of use by reducing the size, complexity, and power of these microsystems, while retaining the selectivity, sensitivity and stability requirements has remained a challenge [2, 28].

1.2.2 Chemical Sensing Microsystems

With the obvious lack of portability for bench-top GC units, progress has been made towards miniaturizing various components of the gas chromatography system with limitations arising as the need for a compressed carrier gas and power source cannot be miniaturized in the form of integrated components [65]. Micro-fabricated columns significantly reduce the size and power requirements of traditional GC [66] and state-of-the-art "portable" systems allow for a multi-dimensional analysis of the sample. This enables the separation of numerous analytes in a short time window, but many systems occupy 30 L, which is far removed from the size required for integration in consumer level devices [67]. The most recent work has a MEMS preconcentrator, MEMS separation column and CMOS detector integrated in a $<$2 L package; however, Figure 1.4 shows the macroscopic components size requirements overshadowing the MEMS components [60, 68, 69].

Complementary metal-oxide-semiconductor (CMOS) and other integrated circuit (IC) compatible sensors are a promising solution to increase portability. Possible sensing devices include Rayleigh surface acoustic wave devices, mass or stress sensitive micromachined cantilevers (static or resonant mode), pellistors, Seebeck-effect sensors, Fabry-Perot

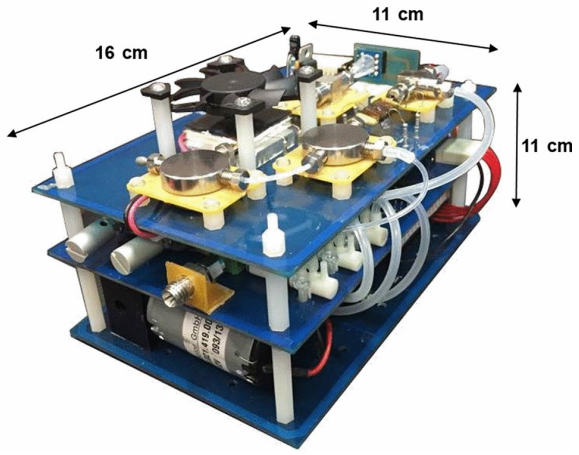

Figure 1.4: *Prototype μGC system. The MEMS preconcentrator, MEMS separation column and CMOS detector sizes are overshadowed by the large macroscopic components linked to carrier gas flow and temperature control [60].* © *2016 IEEE, Reprinted with permission.*

microspectrometers, voltammetric/amperometric sensors, chemotransistors, and conductometric sensors [70]. Many of these devices are referred to as MEMS, microelectromechanical systems, that combine electrical and non-electrical functionality in a miniaturized format.

While such MEMS-based devices and chemical sensors typically cannot rival the precision and accuracy of laboratory-based devices, such as GC-MS, applications where system requirements exclude traditional instruments due to high cost, limited portability, or high power requirements can make effective use of MEMS technology [2, 71, 72]. They allow for co-integration with other sensors and supporting circuitry in one system, while maintaining system sensitivity requirements, with or without chromatography techniques [73, 74]. Integration can reduce the measurement chamber volume, resulting in a proportional reduction in both the amount of analyte needed for detection in a fixed volume and an improved response time of the system [40, 75, 76]. MEMS chemical detectors coupled with a μGC column, for analyte separation, further increase system performance (while maintaining pseudo portability as it is still limited by the container size of a carrier gas source) [62, 77–85]. Additionally, CMOS or MEMS sensors are inexpensive compared to traditional devices, as they rely on batch fabrication using established IC processes, reducing individual device cost [86, 87]. On chip data acquisition allows for an increased signal-to-noise ratio [88] and provides for a multidimensional analysis without adding large hardware components. Typically, in these sensors, the analyte either absorbs into a sensing film on the device or adsorbs to the sensor-environment interface surface causing a response proportional to the analyte concentration. The partition coefficient, K, describes the thermodynamic equilibrium of the analyte in gas phase to the ad/absorped state on the sensing surface/film [43, 89]. A few chemical sensor types are briefly discussed in the following.

Hot-bead pellistors are the most common detection method for combustible gases in industrial settings [90]. The sensors incorporate a catalyst that allows for analyte (such as hydrogen or methane) oxidation below the lower explosive limit, thus detecting poten-

tial hazardous conditions [91]. MEMS technology helped miniaturize these sensors and expanded their ability to discriminate between the heat of catalytic oxidation allowing for higher specificity [92], but applications are limited to flammable analytes [43]. While still measuring thermal properties, thermal conductivity detectors (TCD) do not require analyte reactions with a catalyst, as they sample the thermal conductivity of the environment [93]. While offering quick sensor responses, TCD sensors suffer from cross sensitivity to various analytes and some, similar to GC-MS systems, require a carrier gas with a stable flow and constant temperatures to operate [77, 94].

Metal oxide semiconductor sensors have shown low ppb detection limits towards select VOCs as conductometric transducers, but typically require high-temperature operation, thus increasing power consumption [95, 96]. The devices can be co-integrated with CMOS circuitry using post-CMOS fabrication steps to create suspended micro-hot plates, to reduce power consumption, and to deposit the sensing film [97]. Different semiconducting metal oxides such as $\mathrm{SnO_2}$, CuO, $\mathrm{Cr_2O_3}$, and $\mathrm{TiO_2}$ can be used as the sensing layer to target specific analytes [98, 99], but material cross sensitivities still exist [94].

Advances in polymer science have allowed for low-power and room-temperature measurements using polymeric sensing films [98–100]. Polymer sensing films enable absorption sensing, and can be combined with a wide variety of transducers. Sensors employing these films suffer from interference sources as the absorbing film is sensitive to multiple analytes. Thus sensing systems built using these devices must develop techniques to distinguish between an interfering source and the analyte of interest [101].

Chemicapacitors are one class of MEMS devices that utilize polymeric sensing films, exhibiting LODs in the low ppm range towards certain analytes, while typically maintaining low power requirements [102]. Changes in the dielectric constant (ε_r) of the sorbing material with analyte interaction cause a proportional change in capacitance [70]. While the fabrication of these devices can be performed with steps already contained within the standard CMOS process [103], chemicapacitors are limited to applications where the ana-

lytes of interest have distinct ε_r from the polymer film and from each other [104]. Because of the high dielectric constant of water, capacitive sensors are commonly employed for humidity sensing [105, 106].

Mass-based sensors form an attractive sensing platform for absorption sensing using polymer films, as any potential molecule of interest has a well-defined mass [107]. Generally, mass-based sensors utilize a resonant mechanical structure, where the mass change induces a change in the structures resonance frequency.

Surface acoustic wave (SAW) devices are a common sensing platform for mass based sensing and have already been commercialized [108, 109]. Typically operating between 100 MHz to 300 MHz [110], special circuitry or reference devices are often required to make accurate measurements [70, 111]. SAW sensors, typically a quartz crystal microbalance (QCM), have a similar gas-phase limits of detection as cantilevers [40].

Polymer-coated cantilevers, operated as a dynamic beam, where the resonant frequency is a function of mass, are also popular chemical sensors. The well-understood physics governing cantilever beams provides a platform for mass sensing that cannot be replicated with acoustic resonators [112]. Additionally, they are more easily integrated into CMOS compatible MEMS devices and do not require any exotic material or piezoelectric stacking [107].

Table 1.2 compares a subset of IC compatible sensing techniques for volatile organic sensing against traditional sensing mechanisms. As each system has advantages and disadvantages towards specific analytes within the VOC class of compounds and as different detectors coupled with MS and gas chromatography can significantly change LOD and selectivity, this table only provides a generalized comparison of the techniques.

Analytical systems, shown in the first four rows typically provide excellent LOD, stability and selectivity. This is generally achieved with high power requirements, a large desktop footprint with gas cylinders, and at high cost. Conversely, sensor technologies (enabled in part by MEMS) are typically low power and benefit from batch fabrication techniques,

Table 1.2: *Generalized comparison of volatile organic sensing techniques. Data tabulated from [2, 28, 98].*

Technology	LOD	Stability	Selectivity	Power	Portability	Cost
Mass Spectrometry	++	++	++	–	–	–
Bench-Top Gas Chromatography	++	++	++	–	-	–
Portable Gas Chromatography	+	+	+	-	Not in-situ	-
μGas Chromatography	+	+/-	+	+		Under Development
Polymer-Based Chemiresistor	-	-	-	++	++	++
Metal-Oxide Semiconductor	++ (combustible gases)	–	+	+	+	+
Polymer-Based Acoustic Sensor	+/-	-	-	+	+	++
Polymer-Based Static Cantilever	+/-	+/-	-	+	+	++
Polymer-Based Resonant Cantilever	+	-	-	+	+	++

which decrease the cost of single chips. As many sensor technologies are CMOS compatible or can be integrated closely with a CMOS chip, the space required to operate the sensor device is minimal. This, when combined with a low power requirement, enables sensor portability. However, these devices can be far less sensitive, stable and selective compared to the traditional analytical systems near the top of the table.

1.2.3 Cantilever Sensors

Cantilevers are well known MEMS structures and the physics governing their behavior is well understood and documented. As such, the applications space for cantilever technology is vast, with cantilevers being used in temperature sensors, 3-D AFM mapping, environmental gas and liquid sensors, film stress detectors, accelerometers, and electromechanical electrodes [113]. In the case of environmental sensing, transducing a chemical signal utilizes either a static bending of the beam [114] or a resonant frequency shift [115] due to stress or mass changes in the sorption film.

The mass change resulting from sorption of an analyte in the sensing film can be readily detected by resonant cantilevers as with other mass sensitive sensors. However, analyte identification is difficult to achieve as the sensing film (traditionally a polymer, metal oxide, or self-assembled monolayer) adds only partial selectivity to the device and interfering analytes also cause a mass change [116]. Most sensing systems detect the absolute mass gained as a function of time, which, for a given device, is proportional to three independent

variables: the ratio of analyte within the sensing film to the gas phase, described by the analyte-polymer-specific partition coefficient (K), the analyte concentration in gas phase (C_A), and the analyte mass (m_a) [89]. For example, PIB is a common polymer for detecting toluene [61], with a partition coefficient of approximately 1030, but it is also highly sensitive towards benzene ($K = 360$), n-octane ($K = 1720$), tetrachloroethene ($K = 2060$), m-xylene ($K = 3400$), and pyrrole ($K = 810$) [117]. This cross sensitivity decreases the specificity of a device for a given response, but can be overcome by utilizing arrays coated with different partially selective films [114, 115, 118]. The cross sensitivity can also enable measurements of many analytes, so long as there are techniques for discriminating between them in post-processing of data or pre-separating the sample (similar to a CG column).

As each measurement is proportional to K, C_A and m_a, accurately measuring all three variables to identify the analyte(s) and concentration(s) necessitates the use of arrayed devices. In this case, each sensor is coated with different partially selective coatings, creating an "artificial nose". A principal component analysis (PCA) utilizes the partial orthogonality of the sensing films towards various analytes to remove the ambiguity caused by the multiple degrees of freedom in the system. This post-processing technique leads to accurate identification and quantification for the analytes in the system [119–121]. A PCA utilizes *m*-sensors' responses (where each sensor is coated with a different partially selective film) on a known data space to reduce the acquired data set into a manageable dimensional space for analysis. Ideally, this analysis is able to extract uncorrelated and orthogonal properties of the analyte [121]. Current technology has demonstrated up to 1024 cantilevers on a single chip integrated with CMOS circuity [122], and while most chemical sensing applications do not require such large arrays, this demonstrates the flexibility and scalability of arrayed cantilevers. Other mass based sensors, such as QCMs have not demonstrated the arrayed system to the extent of cantilevers because of integration challenges [123].

Resonant mass sensing using cantilevers has demonstrated detection limits below that of pure deflection techniques [123] and is the primary sensor utilized in this thesis. The

resonant frequency of a cantilever beam can be expressed as

$$f = \sqrt{\frac{K_{eff}}{M_{eff}}} \tag{1.1}$$

where M_{eff} is the beam's effective mass [124, 125] and K_{eff} is the effective spring constant of the beam. Mass changes in the beam are approximated by a proportional resonance frequency shift

$$\frac{\Delta f}{f} \approx -\frac{1}{2}\frac{\Delta m}{m_{beam}} \tag{1.2}$$

where Δm and m_{beam} represent any change in mass due to sorption and the beam mass, respectively [126].

The limit of detection for a resonant mass sensor is defined as

$$\text{LOD} = 3\frac{\Delta f_{min}}{S}, \tag{1.3}$$

where Δf_{min} is the minimum detectable frequency shift and S is the chemical sensor sensitivity $\partial f/\partial C_A$ [45, 127]. The technology has matured from detecting sub-nanograms with MEMS technology [128] to attograms with nanoelecromechanical systems (NEMS) technology [129]. This sensitivity is attractive for gas sensing applications that require low detection limits [130]. While NEMS exhibits ultra high sensitivities, it requires overcoming issues with fabricating nanometer scale devices and coupling the mechanical properties of that device into a measurable physical signal [129], thus current technology favors the practicality of MEMS cantilevers for gas sensing.

Mass changes measured as frequency shifts within a system bring additional system complexity, as most naturally occurring systems do not rapidly change analyte concentrations in a step function, but rather increase or decrease concentration slowly. Therefore, in order to measure the mass change from a known reference to the analyte loaded states, a refresh or purging cycle is introduced with a reference gas or liquid [101, 131]. This addition

removes many advantages of integrated MEMS, as the supporting hardware and reference gas increases the size and the power requirements, limiting portability of the system.

Compared to traditional state-of-the-art analytical instruments, in particular MS and GC, resonant cantilevers have an inferior LOD and their selectivity is determined by the aforementioned polymer coating [28]. Additionally, the long-term stability of a cantilever depends largely on environmental effects [132]. In a GC equivalent system, the supporting hardware maintains a constant environment, but adds to the total size of the system [133]. A cantilever system can utilize uncoated reference cantilevers or different resonant modes with known temperature dependencies to remove environmental effects and other effects not directly related to the analyte-polymer interaction [132]. This allows a cantilever system to be integrated with other sensors in an uncontrolled environment and allow for long term measurements. Additionally, unlike GC/MS, cantilevers can be operated in a highly portable unit as they have been shown to not require the complex gas flows to generate transients needed for analyte analysis [61].

1.3 Sorption Characteristics

Similar to MEMS pellistors increasing selectivity by analyzing the heat of catalytic oxidation [92], assessing sorption kinetics through the governing physics and analyte specific constants (i.e. Fick's laws of diffusion, partition coefficients, and diffusivity coefficients) allows for increased selectivity. This can be used in lieu of or complimentary to arrays with partially orthogonal sensing films [134, 135].

For simplicity the polymer dimensions in $\hat{x}$ and $\hat{y}$ are assumed to be much larger than in $\hat{z}$, so one dimensional Fickian diffusion in the film is assumed and can be expressed as

$$\frac{\partial C(z,t)}{\partial t} = D(T)\frac{\partial^2 C(z,t)}{\partial z^2}, \tag{1.4}$$

where $C(z,t)$ is the analyte concentration in the film at time t and z is distance from

the polymer and gas interface. The boundary conditions are $C(0,t) = K(T) \cdot C_A$ and $\partial C(z,t)/\partial z|_{z=h} = 0$, with $K(T)$ and h being the partition coefficient at the given film temperature and the film thickness respectively, while the initial concentration within the film $C(z,0)|_{z \in film} = 0$ [135].

The solution of this differential equation gives the analyte concentration in the film $C(z,t)$ as a function of time and spatial coordinate z. The mass sensor, however, measures the overall mass change $M(t)$ (per surface area) in the film at time t, which is proportional to the integral of $C(z,t)$ over the film thickness. $M(t)$ normalized by the final mass change (M_∞) at equilibrium, is given by

$$\frac{M(t)}{M_\infty} = 1 - 8 \sum_{n=0}^{\infty} \frac{1}{[(2n+1)\pi]^2} e^{-(t/4\tau)[(2n+1)\pi]^2}, \tag{1.5}$$

where $\tau = h^2/D(T)$ is the characteristic diffusion time constant with the diffusion coefficient $D(T)$ at film temperature T [101, 134]. This infinite sum can be approximated as

$$\frac{M(t)}{M_\infty} = \frac{2}{h}\sqrt{\frac{D(T) \cdot t}{\pi}} \tag{1.6}$$

for $M(t)/M_\infty \leq 0.5$. Thus, measuring $M(t)/M_\infty$ as a function of the square-root of time allows for simple diffusivity measurements that might otherwise by infeasible due to available computational power [101]. Of note is, the temperature dependence of both partition coefficient (measured at equilibrium) and diffusivity (measured during the transient response) allow for analyte discrimination and lead to a more specific system. While various methods exist to model and measure diffusion coefficients, typically utilizing a stationary gas chromatography or MS system [136–139], this work focuses on resonant cantilever sensors with absorbing polymer sensing films.

The equilibrium response of a cantilever is directly proportional, in a first order approximation, to the analyte mass, analyte concentration and partition coefficient. This has traditionally been analyzed to determine the analyte concentration [70, 140]. Signal pro-

cessing and neural networks can be used with sensor arrays to identify gas components in the aforementioned "electronic nose" [114, 115]. While the analyte mass is fixed and concentration typically remains constant over short periods of time, the partition coefficient is polymer and temperature dependent and is defined as

$$K(T) = \frac{C_{poly}(T)}{C_A}, \tag{1.7}$$

thus the equilibrium mass gain, per unit area, in the sensing film being

$$M(T) = K(T) \cdot C_A \cdot m_a. \tag{1.8}$$

Expressed as a first order approximation in terms of thermodynamical constants as a function of temperature and considering the most dominant temperature-dependent term only, the partition coefficient is given by

$$\log K(T) = \alpha + \frac{\Delta H_{Vap}}{2.303 \cdot RT}, \tag{1.9}$$

where ΔH_{Vap} is the enthalpy of vaporization for the analyte, R is the gas constant, T is the absolute temperature, and α is considered a constant associated with the analyte-polymer pair [141] in this simplified model. ΔH_{Vap} has a temperature dependence, but can be considered constant over small temperature ranges [142]. α also has temperature-dependent terms, but is similarly considered constant over small temperature changes [143].

Increasing the film temperature exploits the volatile nature of VOCs towards desorbing from the sensing film. Whereas traditional valve systems change the concentration in the sensing chamber to zero for reference measurements, decreasing the partition coefficient to near zero through thermal modulation has the same impact on the added mass in the sensing film (see Equation 1.8) [28]. Expelling the absorbed analytes via heat utilizes the principle of this equation [28, 61, 107, 139]; however, controlling the heating power, and

thus the applied temperature (such that $M(T) \not\to 0$), would allow for analyte identification through extracting its analyte-polymer thermodynamic constants.

As prior research has shown, resistive heating elements embedded into a resonant piezoresistive cantilever, enable thermal modulation to exploit the volatility of VOCs and "purge" the film of analyte [61]. This allows for more portable devices, since complex valve switching systems with reference gases are no longer required [61].

As lower power sensors are vital for incorporating chemical sensors in portable electronics, lower temperature and shorter heating pulses are desirable. However, with low heating powers and/or shorter pulse durations, the analyte diffusion is too slow causing the system to not reach steady-state, $C(r,t,T)|_{r\in Film} \neq K(T)\cdot C_A$ as the analyte is still redistributing within thick sensing films. Thus, low-power measurements are limited to long pulse durations to assure steady-state conditions. As such, the total energy expenditure of the system can be optimized for either high power pulses of short duration or longer low power pulses [107]. Prior research on cantilevers only examined the dynamics of re-absorption after steady-state, but if the heating temperature is not sufficient such that $K_{\text{heated}} \ll K_{\text{initial}}$, a measurable amount of analyte remains in the film. Equation 1.9 suggests this can be exploited as the partition coefficient ratio at two temperatures can reveal thermodynamic constants specific to the analyte.

Diffusivity is an independent source of information that can aid in analyte discrimination since steady-state signals alone often do not provide sufficient data or the thermodynamic constants overlap [144]. Metal oxide and cantilever sensors have shown the effectiveness of discriminating between similar analytes based on the diffusion time (e.g. $t_{90} - t_{10}$) within a film [134] or fitting to solutions of Fick's law [101]. Analytical diffusion time constant models for polymer-analyte systems enable accurate predictions made for temperature and concentration variations [145]. Approximated as a function of temperature, the models show an Arrhenius relationship between temperature and diffusivity:

$$D(T) = D_0 e^{-E/RT}, \tag{1.10}$$

where D_0 is a diffusion rate constant for the polymer-analyte pair, E is the apparent activation energy and T is temperature in Kelvin [134].

As heating pulses remove the dependence on valve systems to generate transients [61, 101], they also enable modulations to the boundary conditions that were not possible with valves. For example, varying the heating pulse frequency to a point where the analyte absorption-desorption can no longer occur quickly enough acts as a low pass filter, with a characteristic response that is solely dependent on the diffusion time constant and can further be used for analyte discrimination and mimics valve base measurements from literature [134]. This analysis technique, which has signal processing roots in Laplace and Fourier frequency analysis, can be enhanced through the use of heaters to vary the frequency at which the system can no longer respond, further aiding in analyte identification without adding additional mechanical hardware. Prior research theorized about improving the selectivity of cantilever sensors with such heating techniques, but did not begin an investigation into how these types of measurements would be collected or analyzed [107].

1.4 Thesis Objective

The review of chemical sensing technology shows several opportunities in current state-of-the-art technology and techniques for detecting gas phase volatile organic compounds that motivate this thesis. These can be summarized as follows:

1. Traditional gas chromatography and mass spectroscopy units are limited in their applications due to low portability and high cost.

2. Passive sensing through absorption tubes allows for inexpensive sampling of volatile organics in remote locations, but removes any time dependency from acquired data and the ability to observe acute exposures.

3. MEMS and IC compatible sensors, such as resonant cantilever sensors, allow for the various types of chemical sensors to be produced inexpensively. These can be highly portable and low power, but are limited with respect to selectivity, sensitivity (LOD) and stability.

4. Both the transient and steady-state absorption characteristics of sensing films have a temperature dependency and can be utilized to increase the acquired data to aid in analyte discrimination.

5. Modulating the sorption material temperature in a GC-MS column yields information about the enthalpy of vaporization for downstream analysis by the detector.

Considering these opportunities, the objective of this thesis it to develop a novel resonant-cantilever chemical sensing system to discriminate between VOCs without need for an array of cantilevers or a reference gas/valve system. This will be achieved through focusing on temperature modulation schemes applied a heated cantilever through integrated heating resistors and appropriate data processing techniques with analytical models of the cantilever and analyte-sorption film interactions will aid in this pursuit. The research will characterize system responses to an analyte by extracted thermodynamic and absorption coefficients, which will lead to improved selectivity through data processing techniques. Additionally, the proposed research will investigate methods to remove environmental effects on the cantilever and improve long term stability and reliability of the device.

1.5 Thesis Outline

This thesis is organized into the following chapters:

Chapter 2 introduces the temperature dependent sorption properties of polymeric sensing films. The equations governing sorption are described and simulations are presented with applications to chemical sensors

Chapter 3 describes the cantilever sensor used in this thesis including its design, fabrication procedure, and fundamental device characterization. Methods to reduce environmental and self-heating effects are also described.

Chapter 4 investigates the steady-state sensor response at different temperatures for extracting the enthalpy of vaporization, ΔH_{Vap}, from applied heating pulses. The effect of concentration and different polymers on the results is also investigated.

Chapter 5 analyzes the transient response of the sensor for various heating powers. Additionally, the effects of various linear and non-linear temperature modulation schemes are examined.

Chapter 6 investigates more complex environments and combines the analysis from chapters four and five to express the full analyte response within the sensing film due to heating effects. These parameters are analyzed to form a basis for pattern recognition from a multicomponent analysis.

Chapter 7 concludes the thesis by summarizing the contributions made and discusses future extensions to this work.

CHAPTER 2

TEMPERATURE INDUCED ANALYTE SORPTION

Building on the simplified one-dimensional diffusion models described in Chapter 1, this chapter lays the theoretical ground work for the temperature-dependent analyte sorption into the polymeric sensing films studied in this thesis. To this end, the temperature dependent sorption properties, in particular the partition coefficient $K(T)$ and the diffusion coefficient $D(T)$ are introduced and the steady-state and transient sensor responses are investigated, both analytically and with the help of finite element simulations. It should be noted that in this respect, the analyte concentration in the surrounding gas is considered constant and sensor signal changes are initiated by rapid temperature changes of the sensing film.

2.1 General Absorption Equations

The one-dimensional diffusion equation introduced in Section 1.3 is generalized in three dimensions as Equation 2.1.

$$\frac{\partial C(r,t,T)}{\partial t} = D(T) \cdot \nabla^2 C(r,t,T) \tag{2.1}$$

with the analyte concentration $C(r,t,T)$ in the sensing film depending on location r, time t, and temperature T. Naturally, T, is a function of time and spatial coordinate. For simplicity, it is assumed that the diffusion coefficient D depends on temperature, but is independent of the analyte concentration. This is typically justified at low analyte concentrations. Moreover, we generally assume that the temperature is constant throughout the sensing film for a given experiment, e.g. during analyte desorption at T_1 after rapidly heating the sensor from $T_0 \rightarrow T_1$ or analyte re-absorption at T_0 after turning off the heater and rapidly cooling the

analyte from $T_1 \rightarrow T_0$.

Assuming that the analyte concentration is initially zero in the sensing film, the boundary conditions accounting for lateral diffusion from the polymer sidewalls and regions of surface topology become

$$\begin{aligned} C(r,t,T)|_{r\in\text{film-analyte interface}} &= K(r,t,T)\cdot C_A \\ C(r,0,T)|_{r\in\text{film}} &= 0 \\ \frac{\partial C(r,t,T)}{\partial z}|_{z=h} &= 0 \end{aligned} \tag{2.2}$$

where C_A is the (constant) analyte concentration in the surrounding gas, $K(T)$ is the temperature-dependent partition coefficient for the analyte/polymer combination, and $z = h$ describes the interface between sensing film and silicon-based sensor. If the sensor has reached equilibrium at a certain temperature, the analyte concentration is generally not zero in the sensing film, but equal to the product of the partition coefficient at that temperature and analyte concentration in the gas phase. This fact, however, does not change the shape of the recorded transients, but only the magnitude of the recorded signal change.

From Equation 2.1 and Equation 2.2, the steady-state ($dC/dt = 0$) concentration in the sensing film simply becomes

$$C(r,t,T)|_{t\rightarrow\infty} = K(r,t,T)\cdot C_A \tag{2.3}$$

i.e it depends on $K(T)$ only if C_A is constant. The transient concentration $C(r,t,T)$ is far more complicated to analyze and best assessed with the help of finite-element simulations. However, assuming concentration independent diffusion coefficients, the steady-state analyte concentration in the sensing film will be proportional to $K(T)\cdot C_A$ and the signal transient will depend on $D(T)$. Thus, by dividing the transient analyte concentration by the steady-state analyte concentration, we obtain a signal that depends on the diffusion coefficient only.

In the following section, the resulting transient and steady-state analyte concentrations in the sensing film are investigated in detail, as are the resulting sensor responses in case of the mass-sensitive sensor platform. The general conclusions, of course, also apply to other transducers and transduction mechanisms. For the mass-sensitive sensor, the recorded frequency change is proportional to the total mass change in the sensing film, i.e. the sensor signal integrates over the total analyte concentration in the sensing film:

$$\Delta f \propto \iiint_{r \in \text{film}} w(r) \cdot C(r,t,T) dr. \tag{2.4}$$

In the case of polymer-coated cantilevers, the weighting function $w(r)$ is one. This is not the case for other transduction mechanisms such as chemicapacitors and chemiresistors. In these cases, analyte interaction with the electric field lines or current density varies as function of distance to the metal electrodes, thus further motivating mass sensing.

Ultimately, this chapter shows how both, temperature-induced signal transients and steady-state signals, provide identifying information about an unknown analyte, potentially even without needing a prior calibration measurement. The combination of both analysis methods can even further improve analyte discrimination.

2.2 Steady-State Response

As seen from Equation 2.3 the steady-state analyte concentration in the sensing film at constant analyte concentration in the gas phase is proportional to the sensing film temperature through the temperature-dependent partition coefficient $K(T)$.

The partition coefficient $K(T)$ is given by [143]:

$$\log K(T) = \log \frac{\Delta H_{Mix} T}{V_{Poly}^{i,Mol}} - \frac{\Delta H_{Vap}}{2.303 \cdot R T_B} + \frac{\Delta H_{Vap}}{2.303 \cdot R T}, \tag{2.5}$$

where ΔH_{Vap} is the enthalpy of vaporization for the analyte, R is the gas constant, T is the absolute temperature, T_B is the boiling temperature and $V_{Poly}^{i,Mol}$ is the molar volume of the

polymer. This can also be expressed as

$$\log K(T) = \left(\frac{\Delta H_{Vap} - \Delta H_{Mix}}{2.303 \cdot RT}\right) - \left(\frac{\Delta S_{Vap} - \Delta S_{Mix}}{2.303 \cdot R}\right), \tag{2.6}$$

where ΔH_{Mix} is the enthalpy of mixing, ΔS_{Vap} is the entropy of vaporization, and ΔS_{Mix} is the mixing entropy [143, 146].

Considering the most dominant temperature-dependent term in Equation 2.5 only, the partition coefficient, $K(T)$, can be approximated by:

$$\log K(T) = \alpha + \frac{\Delta H_{Vap}}{2.303 \cdot RT} \text{ [141, 147, 148]} \tag{2.7}$$

where the coefficient α is only weakly temperature dependent. If one now assesses the partition coefficient at two temperatures, Equation 2.7 can be written as

$$\log \frac{K(T_0)}{K(T_1)} = \log K(T_0) - \log K(T_1) \tag{2.8}$$

$$= \alpha + \frac{\Delta H_{Vap}}{2.303 \cdot RT_0} - \left[\alpha + \frac{\Delta H_{Vap}}{2.303 \cdot RT_1}\right] \tag{2.9}$$

$$= \frac{\Delta H_{Vap}}{2.303 \cdot R}\left(\frac{T_1 - T_0}{T_1 T_0}\right) \tag{2.10}$$

$$\tag{2.11}$$

Thus, providing a direct relationship between the partition coefficient ratio at two temperatures and the enthalpy of vaporization:

$$\Delta H_{Vap} = 2.303 \cdot R\left(\frac{T_1 T_0}{T_1 - T_0}\right) \cdot \log \frac{K(T_0)}{K(T_1)} \tag{2.12}$$

Equation 2.12 highlights that by measuring a sensor signal that is proportional to $K(T)$ at two distinct temperatures, we can ideally extract a first order approximation to an analyte's enthalpy of vaporization and use this information to distinguish between analytes

independent of the polymer used. The measured steady-state frequency change of the polymer-coated mass-sensitive sensor at two temperatures $\Delta f(T_0)$ and $\Delta f(T_1)$ would provide such an opportunity. Clearly, there are some limitations to this technique and we should not use it to exactly measure ΔH_{Vap}, but to distinguish between analytes. Firstly, and most importantly, the analysis hinges on the fact that only the third term on the right hand side of Equation 2.5 is temperature dependent, which is not true; however, this term has the dominant temperature dependence. Looking at Equation 2.6 instead, the dominant temperature term (first term on right-hand side) depends on $\Delta H_{Vap} - \Delta H_{Mix}$; while the enthalpy of vaporization is generally dominating for the tested analyte/polymer combinations, the analyte/polymer-specific mixing enthalpy may impact the results and ΔH_{Vap} extracted for a given analyte from Equation 2.12 may slightly depend on the polymer used through the impact of the mixing enthalpy. Moreover, as is shown below, the enthalpy of vaporization really also depends on temperature. However, even with all that said and the result of Equation 2.12 in reality not being exactly the analyte-specific enthalpy of vaporization, the analysis method can likely be used for analyte discrimination, particularly if paired with appropriate calibration measurements.

While some chemicals have similar and overlapping enthalpies of vaporization, it is only one metric for discrimination taken at steady-state and can be used in conjunction with diffusivity data obtained from the transient response. Table 2.1 shows enthalpy of vaporization constants from literature and the expected partition coefficient change with a

Table 2.1: *Enthalpy of vaporization coefficients for common VOCs [149] and the corresponding change in partition coefficient from room temperature to a* 30 °C *rise in film temperature.*

Analyte	ΔH_{Vap} [kJ/mol]	$K(293)/K(323)$	Analyte	ΔH_{Vap} [kJ/mol]	$K(293)/K(323)$
Isopropanol	45 ± 3	5.56	o-Xylene	42 ± 5	4.96
Methanol	37.6 ± 0.5	4.20	Toluene	37 ± 3	4.10
Ethanol	42.3 ± 0.4	5.02	Pentane	26.5 ± 0.6	2.75
Acetone	31.27	3.30	Hexane	31 ± 1	3.26
Chloroform	31.32 ± 0.08	3.30	Heptane	36 ± 3	3.95

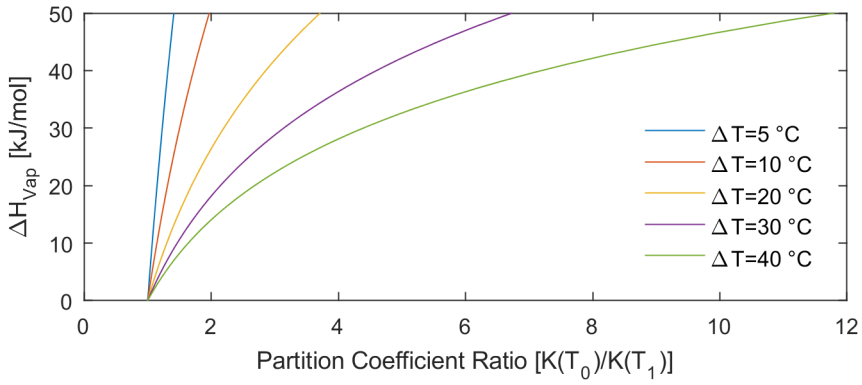

Figure 2.1: *Enthalpy of vaporization as a function of partition coefficient ratio for five different temperature increases from Equation 2.12. The initial temperature, T_0, is set to* 20 °C.

30 °C film temperature increase.

Figure 2.1 shows the enthalpy of vaporization ΔH_{Vap} extracted from Equation 2.12 as a function of the partition coefficient ratio $K(T_0)/K(T_1)$ for different temperature differences, $\Delta T = T_1 - 20\,°\text{C}$, ranging from 5 °C to 40 °C. With enthalpies of vaporization for typical analytes ranging from 20 kJ/mol to 50 kJ/mol, temperature differences in the range of 20 °C affect the partition coefficient sufficiently so that the analyte-specific vaporization constants could be extracted from the partition coefficient ratio. With the above range of vaporization enthalpies, differences in the detected signal from the modulated partition coefficient must be sufficient for detection. Higher heating temperatures allow for increased differentiation with a fixed minimum detectable frequency shifts.

Considering the extracted enthalpy of vaporization being both a function of the temperature difference and the partition coefficient ratio at the two temperatures, Figure 2.1 transforms into Figure 2.2. Here, the x-axis is the partition coefficient ratio for partition coefficients measured at 20 °C and 20 °C + ΔT, the y-axis represents ΔT and the z-axis is the calculated ΔH_{Vap}. Equipotential lines represent a specific analyte (or multiple analytes if they share the same enthalpy of vaporization). Repeated measurements taken at the same or additional temperatures can help reduce measurement errors. While T_0 in this simulation is 20 °C, the presented analysis method could similarly be performed at any

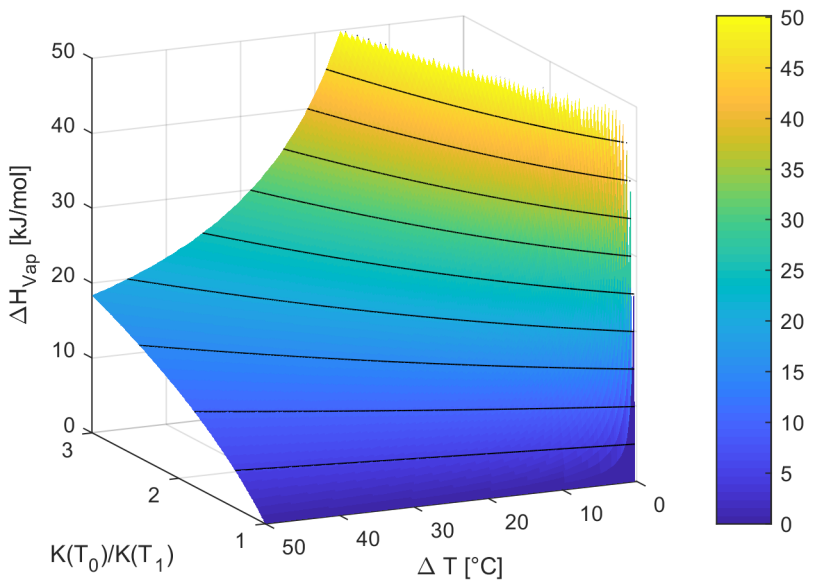

Figure 2.2: *Expanded version of Figure 2.1, where the enthalpy of vaporization from Equation 2.12 is shown as a function of partition coefficient and temperature increase from* 20 °C.

two temperatures. However, practically, the initial temperature should minimized to maximize the initial partition coefficient. This being the case, measurements starting at room temperature are primarily investigated in the absence of active cooling techniques for the piezoresistive MEMS devices.

The temperature T_1 (assuming $T_0 = 20\,°\text{C}$) necessary to achieve a certain partition coefficient ratio for different ΔH_{Vap} can be extracted from Figure 2.3. For temperature rises of 50 °C (from 20 °C to 70 °C), the film's partition coefficient will be reduced from its value at room temperature by a factor of five to twenty for typical VOCs. For smaller temperature differences, the reduction is less drastic, with partition coefficient ratios of two to four for the 20 °C temperature increase above room temperature. As the minimum detectable frequency shift improves, the required temperature difference to discriminate between the enthalpy of vaporization for various analytes will likewise decrease.

Low melting point polymers present a challenge for sensors with low sensitivities as the temperature difference required for accurate discrimination between vaporization enthalpies likely approaches or exceeds the polymer melting point. Resonant mechanical

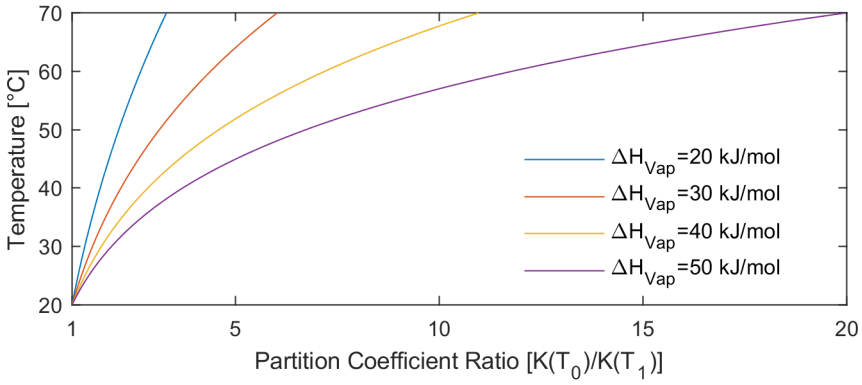

Figure 2.3: *Temperature required to achieve a specified partition coefficient ratio for four different vaporization enthalpies assuming the original measurement was conducted at room temperature (*20 °C*). The sensor response to the sample analyte, which is a function of the room temperature partition coefficient, analyte measurand, and concentration, coupled with the minimum detectable frequency shift sets the limit of detection. This heating measurement scheme decreases the limit of detection, as the increased temperature decreases the partition coefficient (shown along the x-axis).*

structures exacerbate this issue as forces from device motion redistribute the softened polymer. Thus, selecting high melting point polymers and increasing the resolution of a resonant cantilever sensors are paramount for system performance and identification of analytes. For applications that require low melting point polymers, alternate transduction methods such as static cantilevers or polymer coated capacitors are viable options.

Equation 2.12 assumes that the enthalpy of vaporization is constant over temperature; however, as this is only an approximation, the impact of the temperature dependence of ΔH_{Vap} on the proposed measurement techniques is analyzed in the following. The dependence of the vaporization enthalpy on temperature is a function of the analyte's critical temperature T_c and three correlation parameters, A, a and β [142]:

$$\Delta H_{Vap}(T) = A \exp\left(-\frac{aT}{T_c}\right)\left(1-\frac{T}{T_c}\right)^{\beta} \text{ [142, 144, 149].} \tag{2.13}$$

Figure 2.4 shows the vaporization enthalpy changes according to Equation 2.13 from their values at 20 °C over a 50 °C interval for select VOCs. Clearly, for the subset of VOCs highlighted in Figure 2.4, the vaporization enthalpy change with temperature is very similar

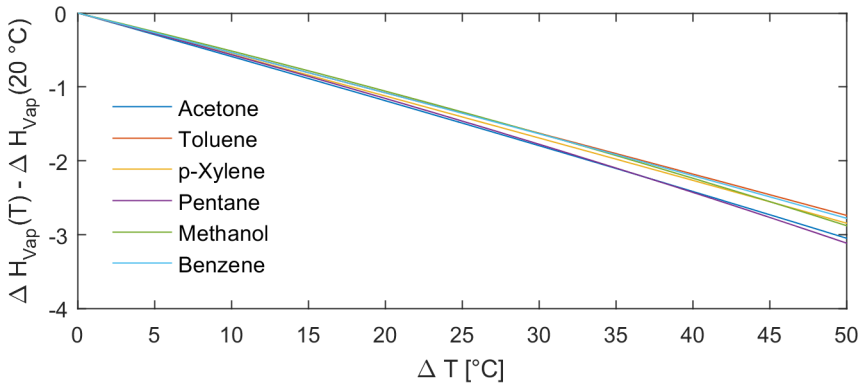

Figure 2.4: *Analytical change in enthalpy of vaporization at* 20 °C *over a temperature increase for six analytes. The variations of vaporization enthalpies between analytes at each temperature is less than 1%. Compensating for this shift is essential to discriminate between analytes and extract reliable vaporization enthalpies.*

and can be approximated by a linear relationship over small temperature changes. For the chosen analytes, the slopes change from 0.0548 kJ/(mol °C) to 0.0623 kJ/(mol °C), with an average slope of 0.059 kJ/(mol °C).

Equation 2.12 can be adjusted for the temperature dependence in ΔH_{Vap} as follows. From Equation 2.13, the enthalpy of evaporation at the two temperatures, T_0 and $T_1 = T_0 + \Delta T$ can be written as

$$\Delta H_{T_0} = A \exp\left(-\frac{aT_0}{T_c}\right)\left(1 - \frac{T_0}{T_c}\right)^{\beta} \tag{2.14}$$

and

$$\Delta H_{T_1} = A \exp\left(-\frac{aT_1}{T_c}\right)\left(1 - \frac{T_1}{T_c}\right)^{\beta}, \tag{2.15}$$

ΔH_2 can also be written as

$$\Delta H_{T_0+\Delta T} = A \exp\left(-\frac{a(T_0+\Delta T)}{T_c}\right)\left(1 - \frac{T_0+\Delta T}{T_c}\right)^{\beta} \tag{2.16}$$

or

$$\Delta H_{T_0+\Delta T} = A \exp\left(-\frac{aT_0}{T_c}\right)\exp\left(-\frac{a\Delta T}{T_c}\right)\left(1 - \frac{T_0+\Delta T}{T_c}\right)^{\beta}. \tag{2.17}$$

The Maclaurin series expansion of the binomial term in Equation 2.17 is represented as

$$\left(1 - \frac{T_0 + \Delta T}{T_c}\right)^{\beta} = \sum_{k=0}^{\infty} \binom{\beta}{k} \left(\frac{-T_0 + \Delta T}{T_c}\right)^{k} \tag{2.18}$$

$$= 1 + \beta \left(\frac{-T_0 + \Delta T}{T_c}\right) + \frac{\beta(\beta+1)}{2} \left(\frac{-T_0 + \Delta T}{T_c}\right)^{2} + \cdots. \tag{2.19}$$

For $\frac{\Delta T}{T_0} \ll 1$, this expansion results in

$$= 1 + \beta \left(\frac{-T_0}{T_c}\right) + \frac{\beta(\beta+1)}{2} \left(\frac{-T_0}{T_c}\right)^{2} + \cdots, \tag{2.20}$$

which is the same series expansion as the third term in Equation 2.14. Thus, Equation 2.17 is equivalent to

$$\Delta H_{T_0+\Delta T} = \Delta H_1 \exp\left(-\frac{a\Delta T}{T_c}\right) \tag{2.21}$$

or further approximated as

$$\Delta H_{T_0+\Delta T} = \Delta H_{T_0} \left(1 - \frac{a\Delta T}{T_c}\right). \tag{2.22}$$

Thus, modifying the analytical expression for measured enthalpy change from Equation 2.12 to be

$$\Delta H_{Vap} = 2.303 \cdot R \left(\frac{T_1 T_0}{T_1 - T_0 \exp\left(\frac{-a\Delta T}{T_c}\right)}\right) \cdot \log \frac{K(T_0)}{K(T_1)}, \tag{2.23}$$

or

$$\Delta H_{Vap} = 2.303 \cdot R \left(\frac{T_0 \cdot (T_0 + \Delta T)}{\Delta T \cdot (1 + T_0 \cdot \frac{a}{T_c})}\right) \cdot \log \frac{K(T_0)}{K(T_0 + \Delta T)}, \tag{2.24}$$

for small temperature increases. While this adds an analyte specific term to the right hand side of the equation (a and T_c), with respect to Figure 2.4, the effect of this addition is similar across a wide variety of analytes. Figure 2.5 displays the compensation ratio α/T_c for a few analytes. With a T_0 of 293 K, the scaled compensation factor $T_0 \cdot \alpha/T_c$ is approximately $0.4 - 0.6$.

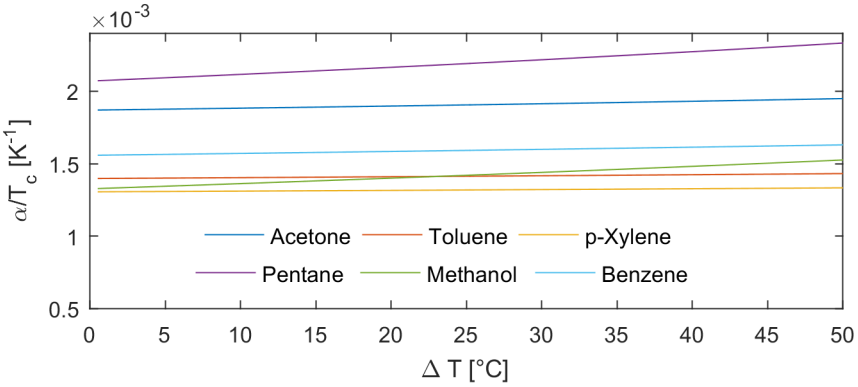

Figure 2.5: *α/T_c ratio over a temperature increase for six analytes to compensate for a vaporization enthalpy temperature dependency in Equation 2.24.*

2.3 Transient Response

Transient data was traditionally acquired via a rapid change in analyte concentration using a high-speed valve to switch between analyte and reference gas. In this thesis, signal transients will also be enabled by heating pulses. The transient response of the sensor can be decoupled from the partition coefficient by normalizing the change in frequency at any time by the steady-state frequency shift. In this case, all responses transition from $0 \rightarrow 1$ for either desorption or absorption. Prior research has utilized rise times (t_{10}, t_{50}, t_{80} and t_{90}) for simplicity [134] in lieu of curve fitting with a diffusivity parameter analysis as in the case of Equation 1.5 and Equation 1.6. While this method does provide discrete data points for analysis, fitting to a curve provides a more robust analytical technique in applications where computational power is available.

Table 2.2 summarizes the results from a COMSOL investigation on a 6 µm film with three previously measured analytes paired with PIB as the sensing film [101]. The model uses one-dimensional Fickian diffusion into the film, with one side held at a constant analyte concentration and the other set to no flux through the node.

As the characteristic diffusion time constant is dependent on the square of the thickness of the film, an appropriate balance is essential to assure that the analyte transients are distinguishable from one another while enabling reasonably short measurement cycles, as

Table 2.2: *Measured diffusivity coefficients for three analytes in a PIB sensing film. In lieu of curve fitting, response times to various predetermined values can distinguish between analytes.*

Analyte	Diffusivity $[cm^2/sec]$	t_{10}	t_{50}	t_{80}	t_{90}
Benzene	11.9×10^{-10} [101]	2	60	172	257
Toluene	10.4×10^{-10} [101]	3	68	196	294
m-Xylene	8.2×10^{-10} [101]	3	86	249	372

sufficient time has to pass to reach equilibrium. In the instance of the aforementioned simulations, an analyte sorption time in excess of six minutes is required for this analysis as the maximum mass gained (i.e. the maximum frequency shift) is necessary so that appropriate normalizations can occur. This long pulse duration would require substantial power in a device, but allows for distinct time constants to be extracted.

Free-volume theory [145] predicts the polymer-solvent diffusivity as a function of temperature as

$$D(T) = D_1(T)\left(1-\phi_1\right)^2\left(1-2\chi\phi_1\right)$$
$$D_1(T) = D_0 \exp\left(\frac{-E}{RT}\right)\cdot \exp\left[\frac{-\left(\omega_1\hat{V}_1^* + \omega_2\xi\hat{V}_1^*\right)}{\omega_1\left(\frac{K_{11}}{\gamma}\right)(K_{21}-T_{g1}+T)+\omega_2\left(\frac{K_{12}}{\gamma}\right)(K_{22}-T_{g2}+T)}\right] \tag{2.25}$$

where

$D(T)$ diffusivity, cm^2/sec;

D_0 constant pre-exponential factor, cm^2/sec;

$D_1(T)$ solvent self-diffusion coefficient, cm^2/sec;

T absolute temperature, K;

T_{g1} solvent glass transition temperature, K;

T_{g2} polymer glass transition temperature, K;

E energy required to overcome attractive forces from neighboring

molecules, cal/mol;

R gas constant, $1.987 \quad cal/mol \cdot K$;

$\hat{V}_1^*$ solvent specific critical hole free volume, cm^3/g;

ξ ratio of solvent and polymer jumping units;

K_{11} solvent free-volume parameter, $cm^3/g \cdot K$;

K_{12} polymer free-volume parameter, $cm^3/g \cdot K$;

K_{21} solvent free-volume parameter, K;

K_{22} polymer free-volume parameter, K;

ω_1 solvent weight fraction;

ω_2 polymer weight fraction;

γ overlap factor which accounts for shared volume;

χ Flory-Huggins polymer/solvent interaction parameter;

ϕ_1 solvent volume fraction;

ϕ_2 polymer volume fraction [150].

While not purely Arrhenius $\left(D(T) \approx D_0 \exp\left(\frac{-E}{RT}\right)\right)$, the primary temperature dependence in $D_1(T)$ can be approximated as such. Prior research predicts high degrees of variation between the diffusivity of various analyte-polymer systems, which can aid in identifying a specific analyte given known diffusivity values [150]. Additionally, fitting to the temperature dependence of the diffusivity allows extraction of both the activation energy E and the pre-exponential factor D_0, and both can be used for analyte identification.

The deposition uniformity of the sensing polymer on the device is an important factor when modeling diffusivity coefficients. Non-uniform films present hurdles as unknown and varying thicknesses increase the measured diffusivity coefficient as the higher surface area

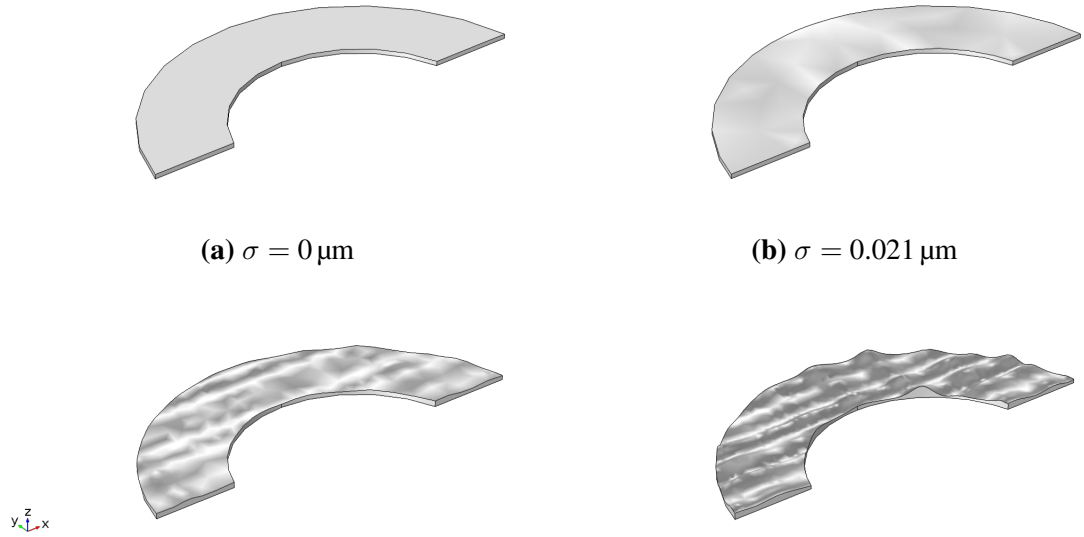

(a) $\sigma = 0\,\mu m$ **(b)** $\sigma = 0.021\,\mu m$

(c) $\sigma = 1.21\,\mu m$ **(d)** $\sigma = 2.56\,\mu m$

Figure 2.6: *COMSOL simulation rendering of four surface topologies with identical volumes (*301 pL*), and increasing film thickness standard deviations (*$\sigma = 0\,\mu m$ *to* $2.56\,\mu m$*). The bottom film boundary is set as a no flux boundary with all other surfaces set to a constant analyte concentration. Analyte diffusion into the sensing film was analyzed using a Fickian diffusion model.*

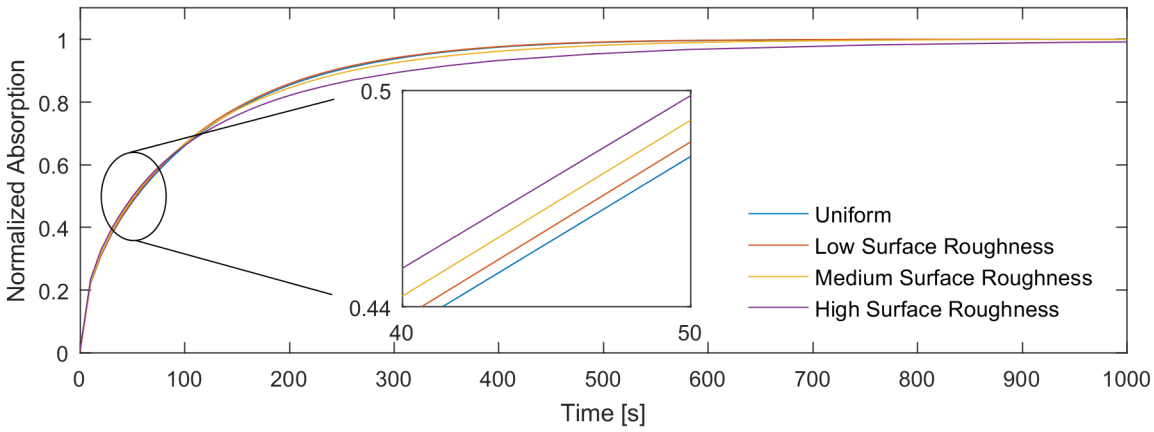

Figure 2.7: *Normalized absorption transients into a sensing film with constant total volume but different thickness variations. While initially the higher surface roughness films have a faster diffusivity coefficient, they tend to slow down the average absorption rate as the diffusion time constant is proportional to the thickness squared.*

accelerates initial diffusion, but this effect diminishes as the thickness squared effect begins to dominate diffusion throughout the film. To investigate the impact of sensing thickness

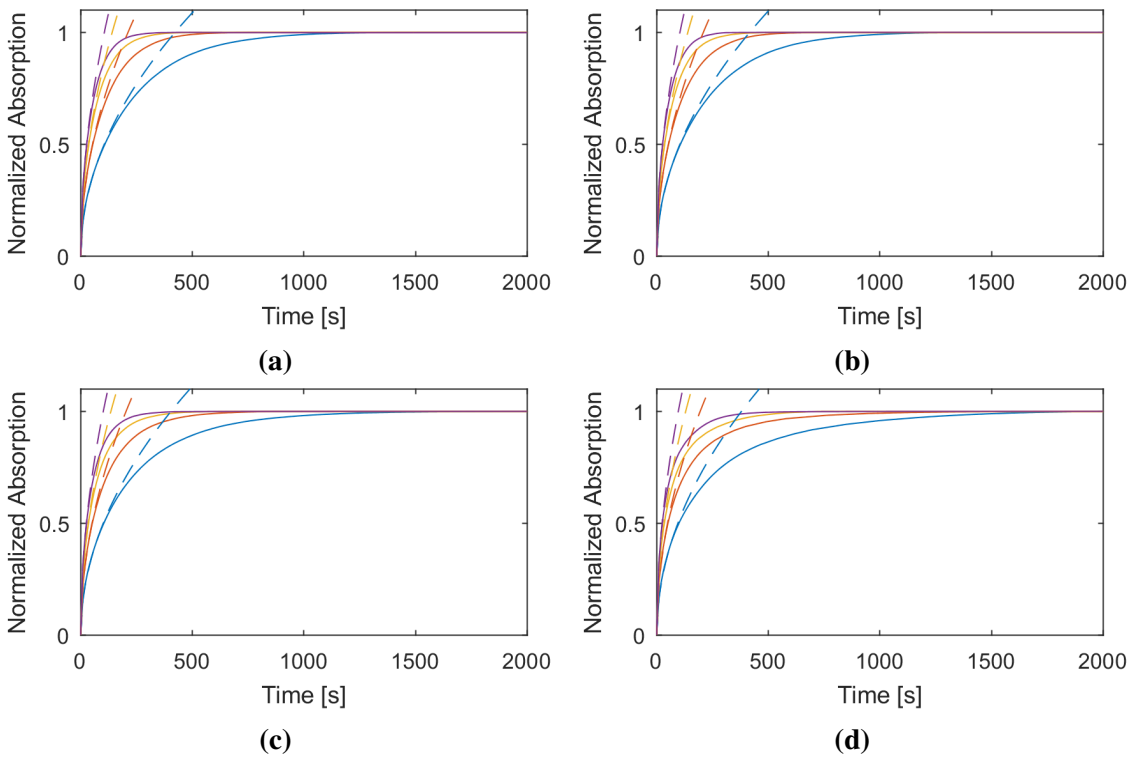

Figure 2.8: *Simulated normalized absorbed mass for the four geometries from Figure 2.6 and four diffusivity coefficients:* 5×10^{-10} cm^2/s, 10×10^{-10} cm^2/s, 15×10^{-10} cm^2/s *and* 20×10^{-10} cm^2/s. *The solid lines represent the COMSOL simulated absorption, while the dashed lines represent the fit for* $M/M_\infty \leq 0.5$ *from [101].*

variations on the diffusion time constants, COMSOL simulations were performed on sensing films with constant volume but different thickness variations. Figure 2.6 compares the four surface topographies; the model simulates four 301 pL film topologies with increasing top surface randomness. The top and side surfaces are exposed to a uniform analyte concentration with a diffusivity coefficient of 1×10^{-9} cm^2/s.

Figure 2.7 shows the variations in the absorption transient due to the thickness variations, with thicker sensing film parts slowing down the analyte absorption. A film with constant thickness (assuming constant film volumes) shows the slowest diffusivity. While this analysis departs slightly from the one-dimensional approximation in Equation 1.5, the non-uniform effects remain constant measurement-to-measurement so long as the film coating on the device remains unchanged.

Figure 2.8 shows how the diffusivity time constants change for the geometrical ar-

rangements in Figure 2.6. Analyzing the simulated absorption transients into the sensing film according to the technique demonstrated by Su et al., where the effective film thickness is extracted using a linear fit with the square root of time for $M/M_\infty \leq 0.5$, results in Table 2.3 [101]. While the film volumes in each simulation are equivalent, the effective thickness for diffusion changes as the surface roughness varies. The modeled effective thickness decreases slightly with increasing surface roughness from the uniform distribution condition. However, as evident from Figure 2.7 near $M/M_\infty = 0.6$ the higher surface roughness diffusion rates slow. This is from the thicker regions of the film beginning to dominate the absorption rates as the time constant is proportional to the thickness of the film squared. Thus, fitting for $M/M_\infty \leq 0.5$ in this manner yields a faster time constant for higher surface roughness, when the true time constant is longer.

Table 2.3: *Effective thickness of films from the varying degrees of uniformity (in Figure 2.6) estimated from* $\frac{M}{M_\infty} = \frac{2}{h}\sqrt{\frac{Dt}{\pi}}$ *[101]. Even with high surface roughness variability, the film absorption time coefficients fluctuate by only a few percent.*

Diffusivity	Uniform	Low Roughness	Medium Roughness	High Roughness
5×10^{-10} cm^2/s	5.186 µm	5.149 µm	5.074 µm	4.916 µm
10×10^{-10} cm^2/s	5.194 µm	5.156 µm	5.084 µm	4.978 µm
15×10^{-10} cm^2/s	5.189 µm	5.156 µm	5.082 µm	4.977 µm
20×10^{-10} cm^2/s	5.188 µm	5.143 µm	5.073 µm	4.958 µm

CHAPTER 3

DEVICE FABRICATION AND CHARACTERIZATION

Pursuant to the system sensing and heating requirements of Chapter 1 and Chapter 2, this chapter introduces the design, fabrication and characterization of the sensor used in this thesis. Additionally, this chapter introduces the measurement and post-processing procedure for collecting and analyzing acquired data.

3.1 Resonant Sensor Design

This research utilizes a thermally actuated and piezoresistively sensed resonant cantilever with heating elements embedded into a near semi-circular head region [61, 107]. An SEM micrograph of the device (in Figure 3.1) shows the cantilever design. Fabricated out of the 20 µm to 25 µm thick device layer of a silicon on insulator (SOI) wafer, the device

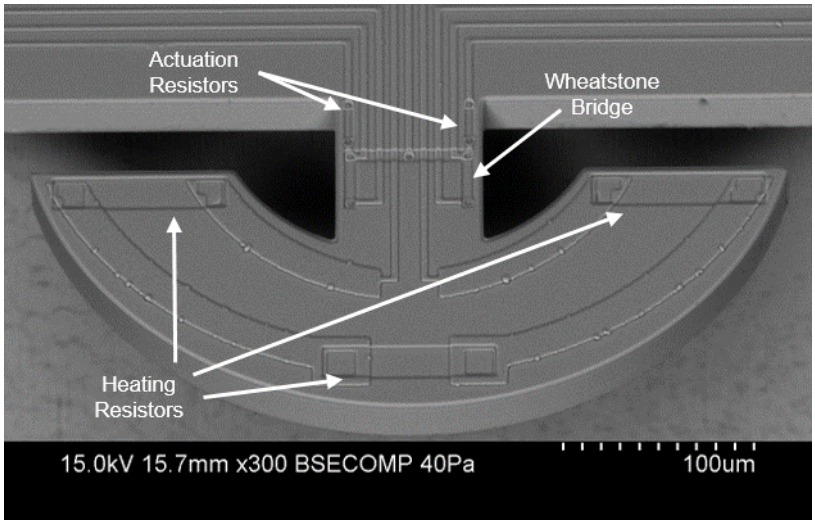

Figure 3.1: *SEM micrograph of the resonant microstructure with a near-semicircular head of radius* 200 µm *supported by a* 75 µm *wide,* 100 µm *long cantilever. Resistors for thermal excitation and piezoresistive detection of in-plane vibrations are located at the cantilever base. Three heating resistors, for rapid and uniform thermal modulation, connected in series are clearly visible on the head region.*

consists of the near semicircular head region, to be coated with an absorbing polymer layer of varying thickness, with an inner radius of 100 µm and an outer radius of 200 µm. This hammerhead-like structure is anchored to the substrate via a 100 µm long, 75 µm wide beam with actuation heating elements and a piezoresistive Wheatstone bridge near the anchor point. The head region focal point is centered on the beam-anchor interface. The semicircle shape has a 44.5 µm air gap from the anchor wall that prevents polymer from bridging the space, resulting in a damped resonator and a decreased quality factor (Q-factor). The integrated heaters for temperature modulation of the head region are connected in series along three locations at the edge of the hammerhead.

From previous research, the sensitivity is independent of lateral dimensions for a given layer sandwich [127]; as a result, the lateral device dimensions can be chosen to optimize other device properties such as the Q-factor (see below). Moreover, any reduction in device dimensions, while increasing the mass sensitivity of the cantilever, will not -to first order- improve the sensor's chemical sensitivity, because the polymer mass and thus the mass uptake in the sensing film decrease in a similar to the cantilever mass [127]. The hammerhead shape limits polymer deposition on regions with high strain, thus maintaining a high Q-factor even with thick polymer coatings [140] and allows for uniform heating [61]. The device thickness balances fabrication yield (thicker devices are more robust to process variations), device stability (thinner devices are more likely to fail during testing) and beam mass (thinner beams allow for higher sensitivity as $\delta f \propto \delta m/m_{beam}$) [107]. Thus the 20 µm to 25 µm thick hammerhead is a compromise between high Q-factors, sensitivity, stability and thermal properties.

3.1.1 Thermal Design

The analysis from Chapter 2 introduces various system requirements for the sensing system stemming from an analysis of both the transient (Equation 2.1) and steady-state (Equation 2.2) response. First, the device coated with its sorbing film must have a short thermal

time constant, well below the diffusion time constant of the analyte into the polymer. This assures that no measurable transient heating effects will influence the ab/de-sorption into the sensing film. Second, the diffusion coefficients must be uniform throughout the film which requires the film temperature to be uniform. This ensures no concentration gradients exist due to a partition coefficient fluctuation or sorption diffusivity variation in $\hat{x}$, $\hat{y}$, or $\hat{z}$. Thus, Equation 2.1 for the three-dimensional diffusion can be reduced into a simpler one dimensional problem (Equation 1.4). Finally, in order to be considered for future portable sensing applications, the device must have a high heating power efficiency.

Three different designs for a heated cantilever, modified from cantilever designs in prior work [140, 151], were simulated for their heating effectiveness. Thereby, the primary design presented in this work is compared to two other designs that utilize a prismatic cantilever beam that is 75 µm wide, 326.5 µm long, and 20 µm thick. These structures (shown in Figure 3.2) have similar finite element model (FEM) simulated resonant frequencies as the hammerhead design.

The hammerhead design sets the heaters (90 µm long and 20 µm wide) in three locations along the outside edge of the hammerhead structure. The two prismatic cantilever designs locate the heaters (70 µm long and 20 µm wide) at either the anchor point of the beam or at three uniform locations starting from the proximal end of the beam. These two locations seek to optimize either the temperature uniformity along the length of the active sensing region or heating power efficiency of the microstructure.

In the COMSOL model, the resonant structure is anchored to a 500 µm thick and 1000 µm wide substrate with a fixed 20 °C temperature at the outer boundary. The remaining sides are encapsulated in a 1 mm^3 air cube that is also fixed to 20 °C at the model boundary. For simulations that incorporate multiple heating sources, the power is equally divided between the heating elements. The transient simulations shown in Figure 3.3, utilize the same boundary conditions as the static models, but a 10 ms long heating pulse of 10 mW is applied to the heating resistors, showing the thermal time constants for the sensing area.

While the temperature rise times are equivalent with equal heating power (see Figure 3.3), the temperature increase for the single heater beam is significantly reduced compared to the other two designs, which are more efficient, but at the expense of uniformity as shown in Figure 3.2. The heater placement on the hammerhead design maintains a high degree of uniformity compared to the prismatic beam with distributed heaters. The prismatic beam with a single heater at the anchor point has the advantage of a uniform temperature profile along the beam's length. This is at the expense of a high power requirement for a given temperature increase, (0.186 °C/mW), as shown in Figure 3.3. This design's extreme temperatures at the anchor point (the area of highest stress-strain) also adds substantial variations to the resonant frequency of the device, due to the temperature dependent Young's modulus of silicon. While the heating power efficiency for the prismatic beam with distributed heaters is similar to the hammerhead design (0.741 °C/mW vs. 0.824 °C/mW respectively), the temperature variance along the length of the prismatic beam (i.e. the active region with polymer) adds uncertainty to the effective temperature of the film. This leads to inaccuracies in the sorption kinetics' predictions and modeling.

Prior research has shown that signal transients, sufficient for analyte discrimination,

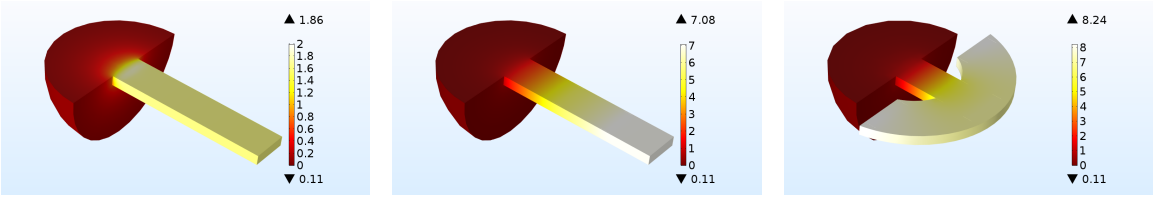

(a) **(b)** **(c)**

Figure 3.2: *Temperature profile from finite element simulations of three* 20 µm *thick microresonantors with similar in-plane resonant frequency due to* 10 mW *of heating applied to the heating resistors: (a) The prismatic cantilever beam design incorporates the heater located at clamped edge to maintain a uniform temperature profile throughout the beam. (b) The prismatic cantilever beam design that uses multiple heaters evenly spaced to increase the heating efficiency from (a), but with reduced temperature uniformity. (c) The hammerhead structured resonator incorporates three heaters at the distal ends of the device to achieve a relatively uniform temperature increase on the head region with lower power consumption than a prismatic beam design.*

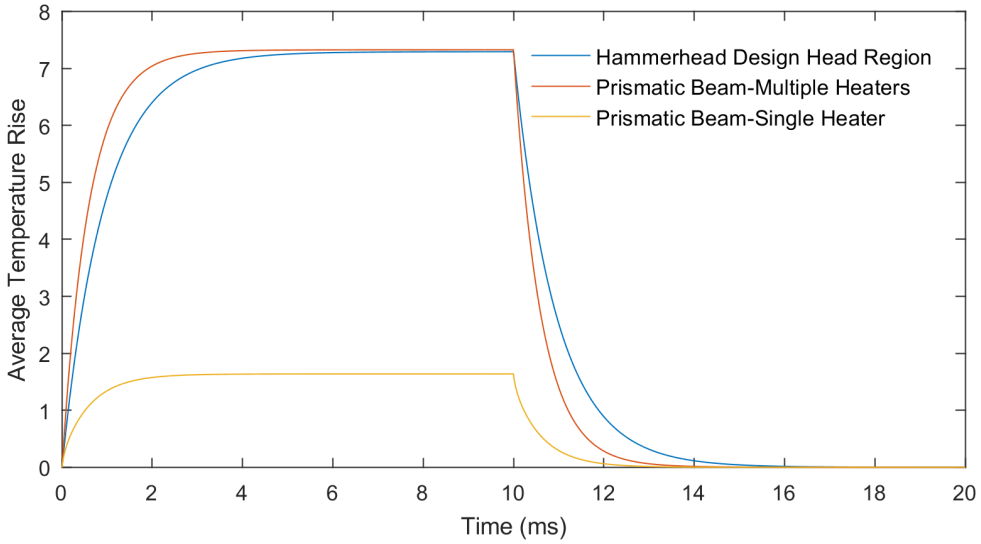

Figure 3.3: *Finite element simulated thermal rise time for the average temperature of the sensing region for three microresonator geometries due to a* 10 ms *long heating pulse of* 10 mW *total applied heating power.*

occur within 1-10 seconds for modest film thicknesses ($\approx 4\,\mu\mathrm{m}$) [101]; this requires that any method of generating transients occur at time scales significantly shorter than 1 s. The 90% rise and fall times for the three geometries are within 2.5 ms (see Figure 3.3). This is also significantly faster than the 10 Hz to 20 Hz sampling rate (introduced in Section 3.4) and not significantly different from each other (the hammerhead design rise time is 0.8 ms longer than the prismatic beam due to the added thermal mass). Thus, the heated hammerhead structure introduced by Carron et al. exhibits the desired time constant response and maintains a high degree of temperature uniformity across the sensing region, where the film is locally deposited. This design also limits the temperature rise at the base, reducing the resonance frequency shift due to heating [61].

Additional COMSOL simulations of the hammerhead structure show the effect of a 5 µm PIB film on the steady-state (Figure 3.4) and transient thermal (Figure 3.5) characteristics of the sensor. These simulations also investigate variations in thickness of the SOI device layer, where it is either 20 µm or 25 µm thick.

With 50 mW of total applied heating power, Figure 3.4b shows the film temperature

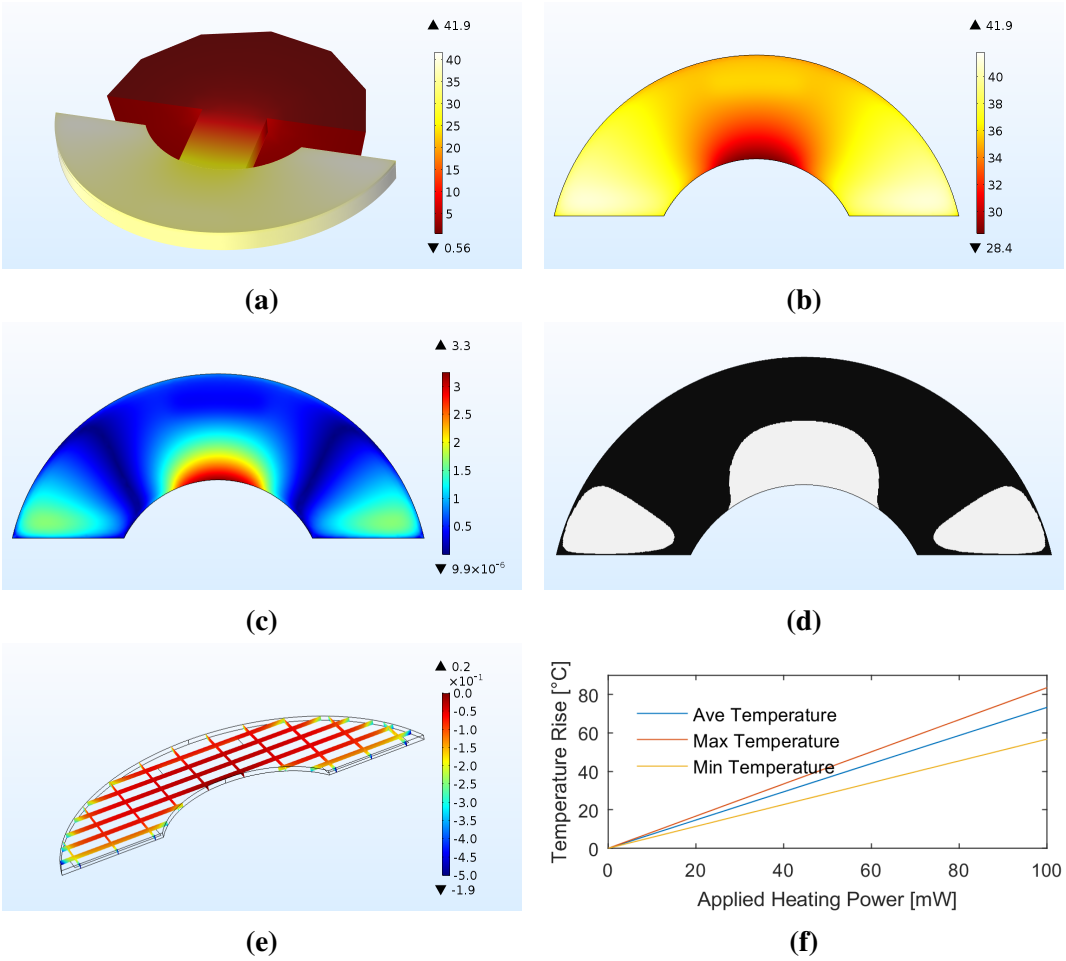

Figure 3.4: *Temperature FEM analysis of the cantilever structure (*25 µm *silicon thickness), film (*5 µm *PIB sensing film covering head region only), and surrounding medium (hidden) subject to* 50 mW *of applied heating power: (a) simulated temperature increase of hammerhead resonator and surrounding silicon support structure indicating the uniform temperature of the head region; (b) simulated temperature increase of head region only; (c) deviation in percentage from average film surface temperature; (d) filtered image of (c) highlighting all areas in black that are within 1% of the mean temperature; (e) temperature "cross-sectional" plot indicating minimal temperature gradients in the vertical direction in* °C/µm*; (f) temperature rise of the sensing film (average, minimum and maximum film temperature) as a function of the applied heating power.*

as not entirely uniform in $(\hat{x}, \hat{y})$. Finite element analysis shows $<$1% deviation from the mean temperature rise for 66% of the film and a $<$3% deviation from the mean temperature rise for 99.8% of the film, ensuring that, while not entirely uniform, a fairly uniform partition coefficient exists throughout the film. As expected, the temperature gradient in $\hat{z}$ direction is negligible, with most of the temperature gradients in the system occurring in

the surrounding air or the extreme corners of the hammerhead. The temperature gradient will vary slightly with differing polymers, but not significantly as to affect the uniformity assumptions.

Modeling the temperature dependency for the Young's modulus of silicon into thermo-mechanical models show a linear decrease in resonant frequency of 7 Hz/mW or roughly 8.5 Hz/°C within the sensing film. The simulated frequency shift corresponds to about −11.6 ppm/°C, while a standard silicon beam would have a shift of approximately −30 ppm/°C. This decrease of temperature's influence on the resonance frequency is due to the localized heating, away from the beam's high strain regions. However, this heating-induced frequency shift will still have to be removed for accurate chemical measurements and will be discussed in Subsection 3.4.2.

Figure 3.5 shows the resulting time-dependent simulation for the average temperatures of the beam and film when the hammerhead structure is coated with 5 µm of PIB. Whereas the initial time constant with no film is 0.98 ms, as expected with the additional thermal mass, simulations with the added polymer show an increased time constant on the hammerhead surface and polymer volume of 1.18 ms and 1.28 ms, respectively. However, most

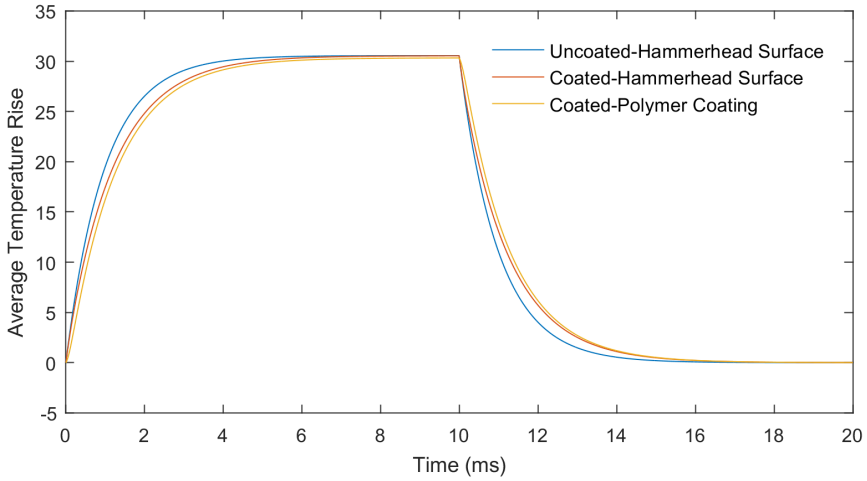

Figure 3.5: *Simulated thermal response, i.e. temperature increase, of the hammerhead resonator with and without a* 5 µm *polymeric film coating to a* 10 ms *long heating pulse of* 10 mW.

importantly the time constants are still on the order of one millisecond, which is significantly faster than diffusion within the sensing film. Time constant differences between a 20 µm and 25 µm device are minimal, with the simulated thermal time constants changing for the 20 µm device by only 10 ns to 30 ns. Additionally, no significant difference in heating power efficiency exists when a polymer film is added to the hammerhead sensing region, assuming no polymer is deposited on the supporting beam.

The resistor near the base, used for electrothermal excitation contributes only 0.15 °C/mW of an added temperature rise to the hammerhead's active region. Thus, a normal excitation signal of 2 V_{pp} offset by 1 V_{DC} through a 500 Ω to 800 Ω resistor results in a 0.6 °C to 0.9 °C temperature increase of the sensing region. This temperature rise is considered minimal and will not affect the initial sorption temperature nor heating power efficiency significantly.

3.1.2 Mechanical Design

The design ensuing from a thermal analysis promotes investigation of the hammerhead shape from previous research [107, 152, 153]. Visualized in Figure 3.6, COMSOL simulations show the first resonant out-of-plane, torsional, in-plane modes have a nominal resonance frequency of 394 kHz, 396 kHz, and 760 kHz, respectively, when the design is

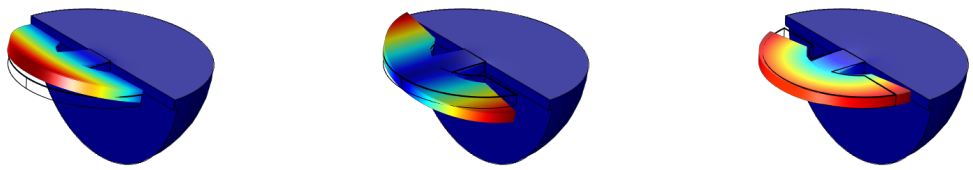

(a) **(b)** **(c)**

Figure 3.6: *Simulated mode shapes for the hammerhead cantilever design: (a) first out-of-plane mode, (b) first torsional mode, (c) first in-plane mode.*

aligned with the $\langle 110 \rangle$ axis of a 25 µm thick SOI (100) device layer with added dielectric passivation layers (totaling 1.5 µm of silicon dioxide and 0.5 µm of silicon nitride) contributing to an increased effective mass detailed in Section 3.2. The silicon structure was modeled as an anisotropic material and the remaining layers were modeled as isotropic. The added mass was simulated as a distributed mass solely on the head region. While in reality limited quantity of polymer is deposited on the supporting beam, a majority of the added mass is on the head region.

Figure 3.7 shows the effect of mass loading from a polymer film located on the head region. Due to its shape, the design cannot be analytically modeled strictly as a lumped mass with the relative resonance frequency shift being given by,

$$\frac{\Delta f}{f} \approx -\frac{1}{2}\frac{\Delta m}{m_{beam}}, \tag{3.1}$$

where f is the resonance frequency, Δf is the change in resonance frequency, m_{beam} is the starting mass of the cantilever, and Δm is the added mass. A linear fit still provides a good approximation to the device behavior over small mass changes. This being the case,

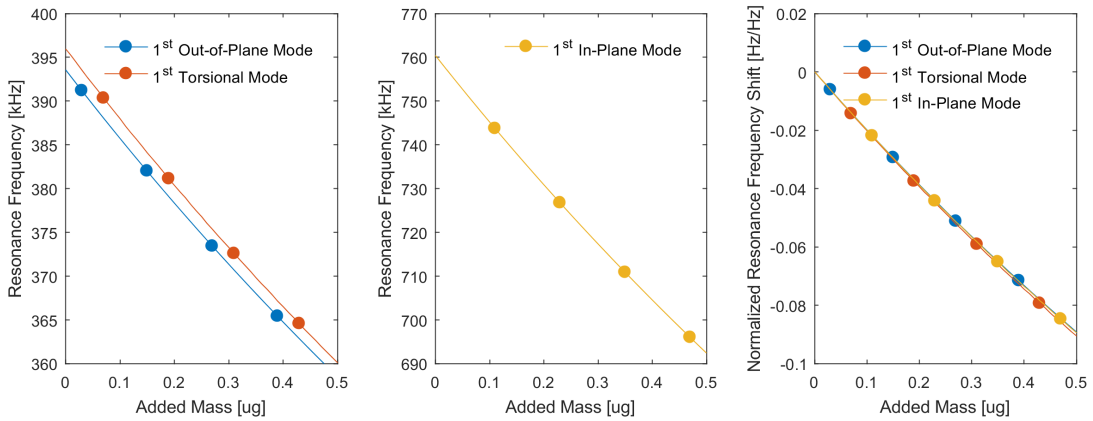

Figure 3.7: *Simulated resonance frequency for the cantilever design as a function of a uniformly distributed added mass on the semicircular head region: (a) first out-of-plane and first torsional resonance modes, (b) for first in-plane mode, (c) normalized resonance frequency shift ($\Delta f / f$).*

finite element models show an expected sensitivity of 70.0 Hz/ng to 78.4 Hz/ng, 71.6 Hz/ng to 80.3 Hz/ng, and 135 Hz/ng to 153 Hz/ng for the three fundamental modes depending on the fitting regions. A U-shaped Wheatstone bridge near the beam's base selectively amplifies in-plane motion while rejecting out-of-plane signals. Sensing using the in-plane mode limits the effect of dampening due to viscous drag on the Q-factor [151] and will be the resonant mode utilized throughout this work.

3.2 Fabrication

The device fabrication is similar to prior work, with the diffused silicon Wheatstone bridge and thermal excitation resistors being located at the center and corner of the supporting beam anchor point, respectively [101, 140, 151, 154]. The added heating elements for temperature modulation of the head region are also diffused resistors in the silicon substrate doped simultaneously with the excitation and Wheatstone bridge resistors, adding no additional steps to fabrication. The designed resistance of the three heating resistors connected in series is approximately 1 kΩ, allowing for significant temperature elevation with low milliampere level current. A detailed process flow utilizing the facilities at the Georgia Tech Institute for Electronics and Nanotechnology's cleanroom is contained in Appendix A.

The device fabrication follows an established procedure within the iSenSys group [107] with slight modifications to the metal patterning procedure. First, a 1 µm silicon dioxide layer is thermally grown in a wet oxidation furnace at 1050 °C as a front-side mask for boron diffusion and a back-side mask for the deep reactive-ion etch (DRIE) release. After patterning the oxide mask, a two-step pre-deposition and drive-in diffusion creates the p-type Wheatstone bridge piezoresistors, thermal actuation resistors, and device heating resistors. The pre-deposition diffusion uses boron solid sources at 930 °C for 40 min. Afterwards the front-side oxide is removed with buffered oxide etch (BOE), while the back-side oxide is protected during the acid etch with photoresist. The drive-in follows in a two temperature oxidation step. The first oxidation at 950 °C has a short 5 min dry oxidation fol-

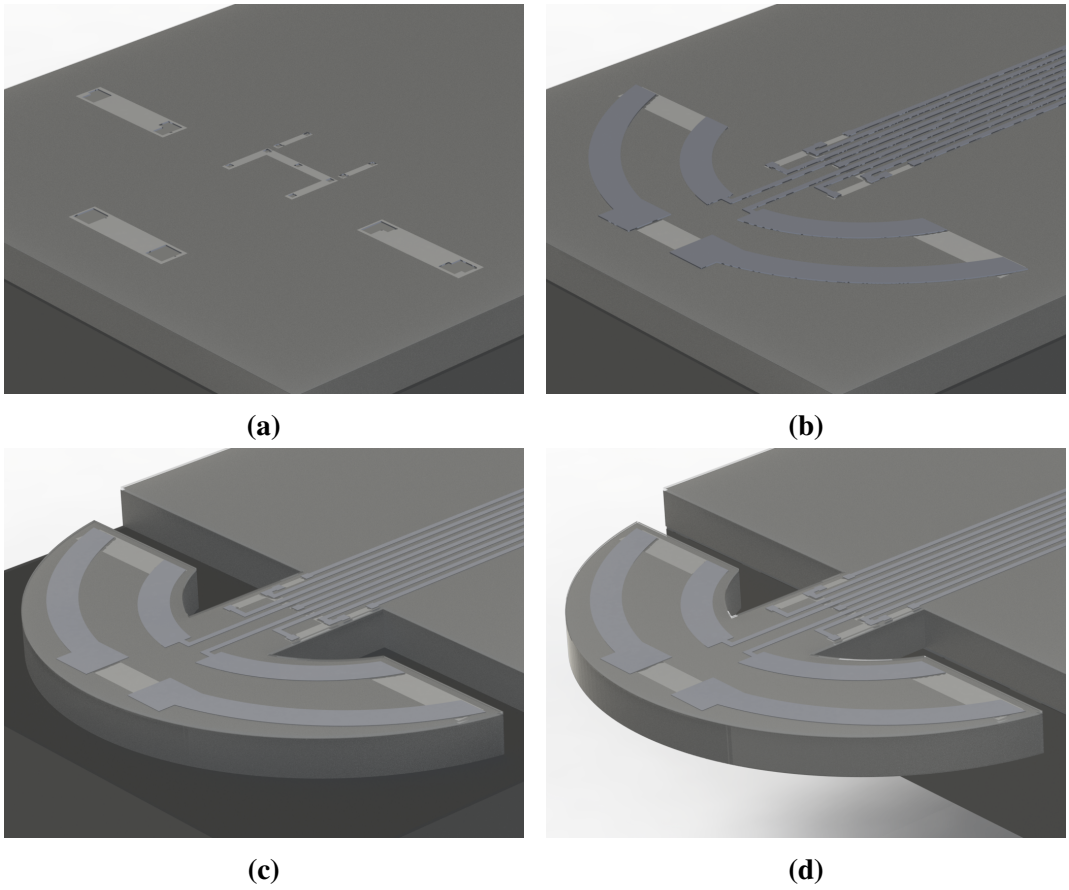

Figure 3.8: *CAD rendering of the fabrication process flow for a silicon resonant cantilever: (a) The doped resistors and vias are created and patterned on an SOI wafer. (b) The aluminum metal is deposited and makes contact with the resistors. (c) The passivation layer is deposited and the front-side of the device is patterned and etched to define the resonator lateral geometry. (d) The device is released via DRIE and a final ICP etch to remove the buried oxide from the back-side.*

lowed by a 30 min wet oxidation. The furnace is then ramped up to 1000 °C for 30 min dry oxidation. This boron diffusion sequence results in 250 Ω/□ sheet resistance in a 10 Ω cm n-type device layer, a junction depth of 1.23 µm, and 120 nm of silicon dioxide on the front-side of the wafer (oxide growth on the back-side is insignificant compared to the already grown 1 µm). An additional 1 µm plasma-enhanced chemical vapor deposition (PECVD) silicon dioxide is deposited and patterned with an inductively coupled plasma (ICP) etch to provide contact openings to the diffused resistors. After etching contact openings, a 750 nm aluminum-copper (99/1%) layer is sputtered onto the surface. After patterning,

the aluminum-copper film is etched with a BCl_3 ICP dry etching step. This etch is highly aggressive with low selectivity to photoresist and requires over-etching to assure complete removal of copper residue. Immediately following etching, the wafer is submerged in DI water to remove residual chlorine that could corrode the metal traces. This dry etching is a departure from previous work that utilized a wet etch in aluminum etchant type A. This new procedure allows for increased reliability of the devices as narrow metal traces are not compromised by an isotropic wet etch. This is followed by an annealing step in nitrogen at 450 °C for 2.5 h. A passivation layer comprised of 500 nm silicon dioxide and silicon nitride is deposited sequentially on the wafer front-side via PECVD. Next, a 2 µm thick silicon dioxide layer is deposited onto the wafer back-side via PECVD, bringing the total oxide thickness on the back-side to approximately 3 µm. The front-side passivation layer is patterned twice with ICP dry etching steps to open up the metal traces' bonding pads and expose the silicon for structural definition. The device layer of the wafer is etched via DRIE (i.e. the Bosch process) in the exposed silicon regions to the buried oxide (BOX) layer, which serves as the etch stop. Finally, the devices are released through back-side bulk micromachining. Initially, the back-side oxide passivation is patterned via ICP etch-

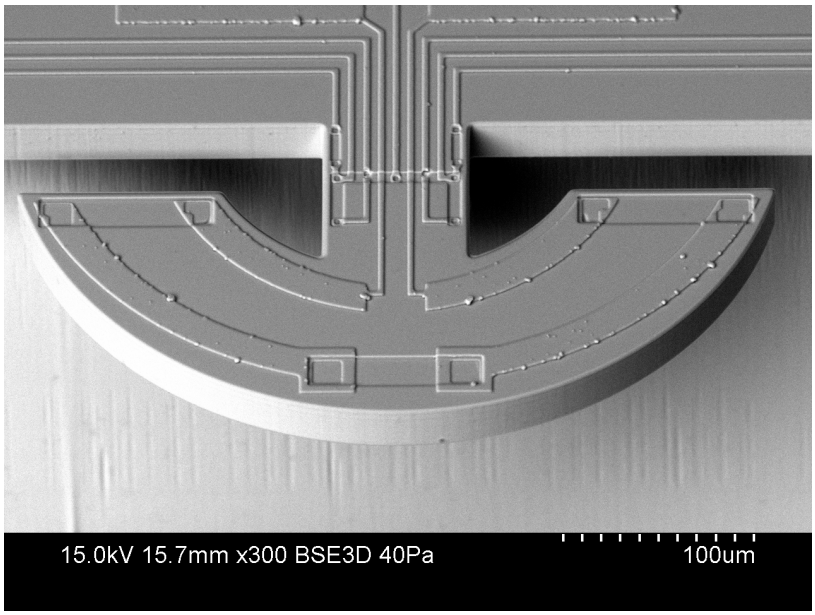

Figure 3.9: *SEM micrograph of the completed resonant cantilever.*

ing. Next the exposed handle layer is etched up to the BOX layer via the Bosch process. Finally, the devices are released as the BOX layer is removed from the back-side via an ICP etch. Figure 3.9 shows an SEM of the completed device.

3.3 Characterization

3.3.1 Mechanical Characterization

Once fabricated, the wafers were diced and individual die were packaged in standard 28-pin dual in-line packages (DIP), wire bonded, and characterized (electrically and mechanically) prior to functionalization (see Figure 3.10). After initial characterization, the devices were spray coated with an absorbing polymer. Suitable polymers are chosen based on the partition coefficient for analytes of interest [117], film quality, and melting point.

For the sample device tested here, PIB dissolved in a 0.1 wt% solution in toluene

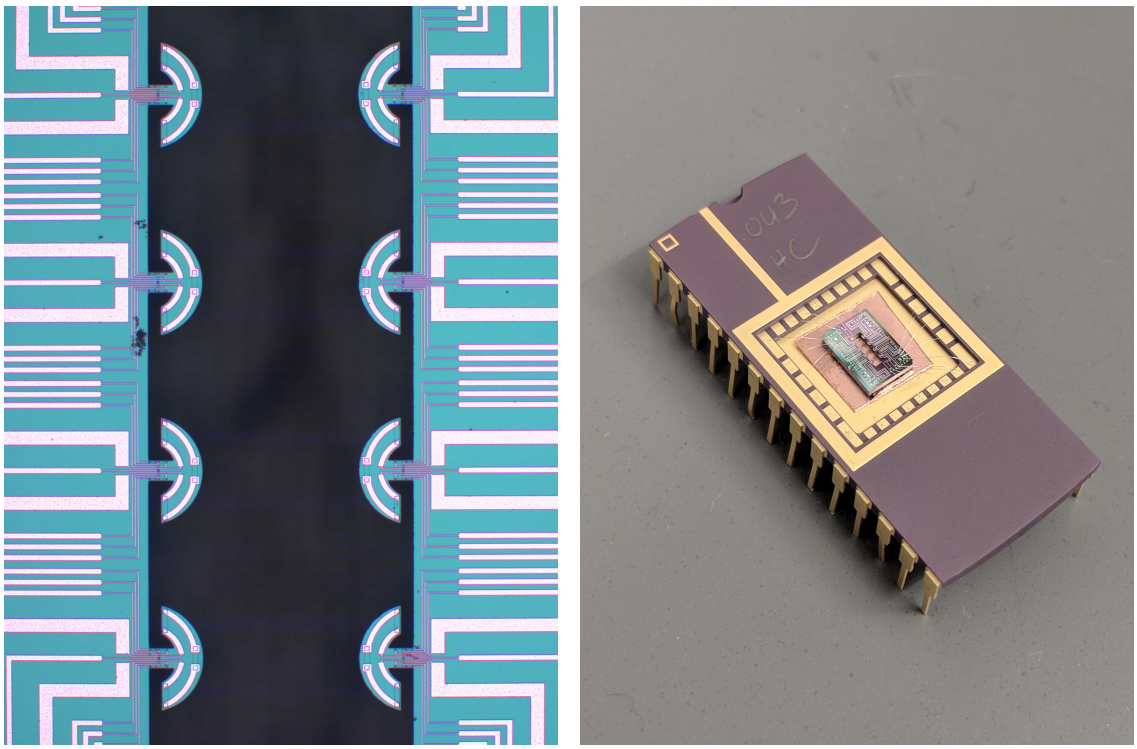

(a) **(b)**

Figure 3.10: *(a) Optical image of completed die showing all eight cantilevers. (b) The die, packaged and wire bonded, in a 28-pin dual in-line package.*

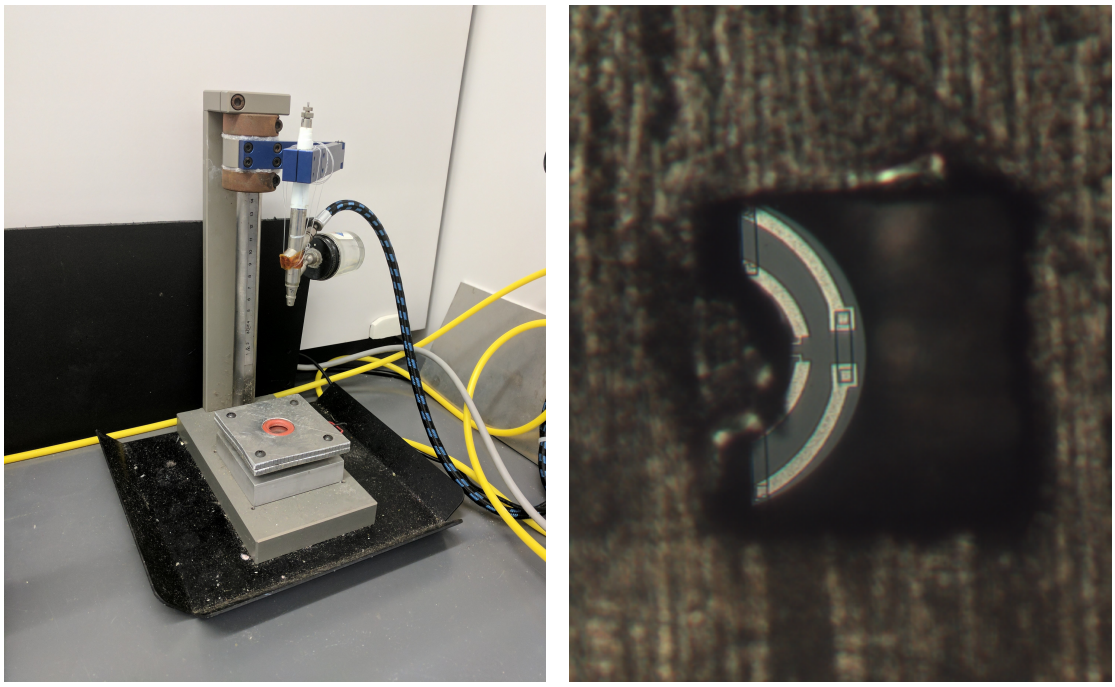

(a) **(b)**

Figure 3.11: *(a) A standard paint gun constitutes the spray coating apparatus for polymer deposition. Its reservoir is filled with a* 0.01 % *to* 0.1 % *by weight polymer in solvent solution. The holder, shown directly under the spray coater holds the laser cut shadow mask aligned to the device. (b) Alignment of the shadow mask to the hammerhead resonator's head region is performed under a standard laboratory stereoscope.*

was spray-coated (via the apparatus depicted in Figure 3.11a) onto the head region with a shadow mask. This laser-cut shadow mask (shown in Figure 3.11b) limits the polymer deposited outside the hammerhead region that would otherwise adversely affect the Q-factor and limit the polymer thickness due to a loss in minimum detectable frequency change [140]. The resulting thick polymer coatings increase the device sensitivity [127] and diffusivity time constant $(\tau = h^2/D(T))$ [101].

After spray coating, the resonance frequency shift is again measured via an open-loop transfer characteristic (see Appendix B). Comparison of the amplitude transfer characteristic before and after film coating can be used to extract amount of polymer deposited and the resulting Q-factor degradation, which affects the limit-of-detection [155]. For the example device in this section, Figure 3.12 shows the corresponding resonance frequency shift of the

device. Aided by a COMSOL simulation, the 31 kHz shift corresponds to approximately 6.1 µm of PIB deposited onto the active region of the hammerhead.

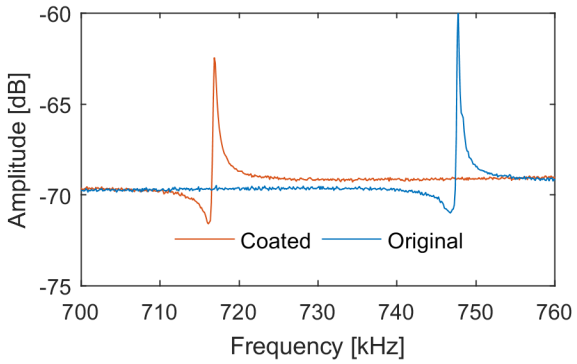

Figure 3.12: *Open-loop frequency transfer characteristics of the first in-plane mode before and after sorbing polymer film deposition. A thick PIB coating of* 6.10 µm *insures long transients and high analyte uptake, while only reducing the quality factor from 2900 to 1300.*

A spray-coated film lacks uniformity with random peaks and valleys as depicted in a confocal image of two polymer-coated devices in Figure 3.13. This profile increases the surface area available for sorption, and decreases observed diffusivity time constants. To increase the uniformity, polymer can be spin coated onto the surface, but this technique decreases the Q-factor as the beam would also be coated. Spin coating also limits the ability to coat arrays with different polymers, as the entire die would be uniformly coated with similar polymers.

3.3.2 Thermal Characterization

Thermal stability of the device is essential for reliable operation of the sensor. Environmental fluctuations and self-induced heating effects both influence the Young's modulus of the silicon, which changes the resonant frequency of the sensor. Operating the device (as described in Section 3.4) in known, stable conditions (such as in an environmental chamber) limits temperature fluctuations, but decreases the portability of the system. Thus, techniques for removing both external temperature fluctuations and self-heating effects must be

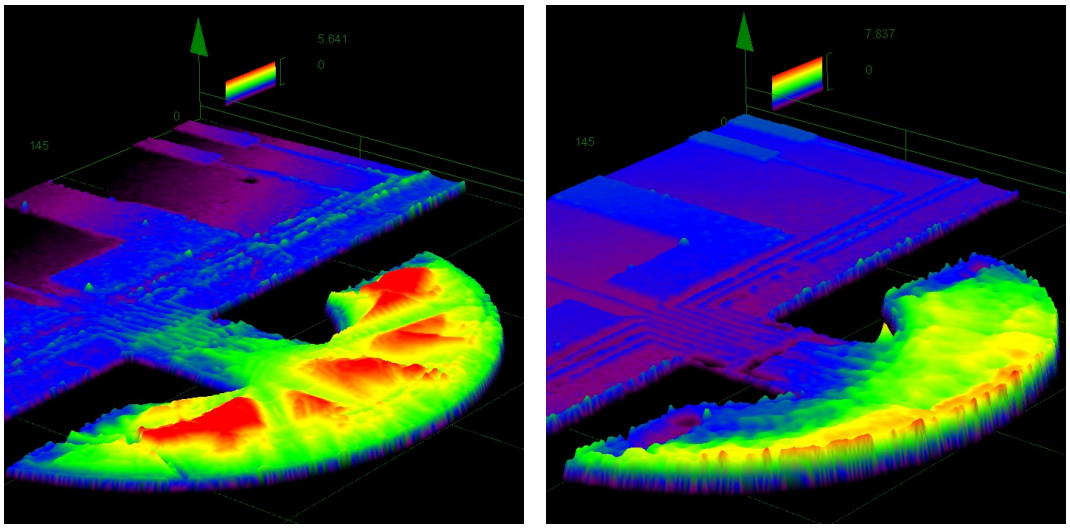

(a) **(b)**

Figure 3.13: *Confocal microscope 3D analysis of two coated devices. The false color corresponds to the polymer thickness. The spray coating with shadow masking film deposition technique produces uneven film surfaces with hills and valleys (a), which increase the effective diffusion rate. This technique also produces regions with limited polymer thickness (shown at the edges of the hammerhead in (b)). Polymer deposited on or near the anchor point as in (a) reduces the quality factor of the device. While shadow masking reduces the amount of polymer deposited in this region, it does not remove it completely.*

taken into consideration when processing the sensor output.

For removing the effect of environmental fluctuations from the sensor output, i.e. resonant frequency, three different reference sensors will be considered: a second uncoated reference cantilever, an on-chip diffused resistor, and a commercially available IC temperature sensor. As the coated cantilever's frequency response changes in response to ambient changes in temperature, an uncoated-neighboring resonant cantilever operated simultaneously can be utilized to provide a reference for a differential measurement. Device-to-device variations exist that do not result in identical responses to ambient temperature fluctuations. This work compares the sensors' responses assuming either a linear or quadratic dependence of the resonant frequency on temperature. In the linear case, the coated and reference cantilevers' measured frequency response to temperature changes in an environmental chamber generates a coupling factor that will be used to remove the effect of slight variations in ambient temperature. Equation 3.3 shows how a linear dependence on tem-

perature can be removed from unmatched devices during a chemical measurement,

$$\begin{gathered} f(t) = f_0 + \Delta f(t) + \alpha f_0 \Delta T(t) \\ f_{ref}(t) = f_{ref,0} + \Delta f_{ref}(t) + \alpha_{ref} f_{ref,0} \Delta T(t) \\ \Delta f_{ref}(t) \approx 0 \\ \Delta T(t) = \frac{f_{ref}(t) - f_{ref,0}}{\alpha_{ref} f_{ref,0}} \end{gathered} \tag{3.2}$$

$$\Delta f(t) = f(t) - f_0 + \frac{\alpha f_0}{\alpha_{ref} f_{ref}} \left[f_{ref}(t) - f_{ref,0} \right], \tag{3.3}$$

where $f(t)$ is the measured frequency of the device, $\Delta f(t)$ is the change in frequency of the device due to analyte (assumed to be 0 Hz for the reference cantilever), f_0 is the original resonance frequency of the device without analyte, $\Delta T(t)$ is the changing environmental temperature, and α is the linear frequency dependence on temperature.

Similarly, a quadratic relationship with temperature can also removed,

$$\begin{gathered} f(t) = f_0 + \Delta f(t) + \alpha \Delta T(t)^2 + \beta \Delta T(t) \\ f_{ref}(t) = f_{ref,0} + \Delta f_{ref}(t) + \alpha_{ref} \Delta T(t)^2 + \beta_{ref} \Delta T(t) \\ \Delta f_{ref}(t) \approx 0 \\ \Delta T(t) = \frac{-\beta_{ref} \pm \sqrt{\beta_{ref}^2 - 4 \cdot \alpha_{ref} f_{ref,0}}}{2 \cdot \alpha_{ref}} \end{gathered} \tag{3.4}$$

$$\Delta f(t) = f(t) - f_0 - \alpha \Delta T(t)^2 + \beta \Delta T(t) \tag{3.5}$$

where in this instance α is the quadratic temperature dependence and β is the linear component. Either analysis can be modified to instead utilize a secondary sensor for temperature detection, such as an integrated resistor that uses the temperature coefficient of resistance to detect temperature fluctuations or an external integrated circuit. A neighboring uncoated device has the fundamental advantage of having similar thermal properties as

the coated sensing cantilever, thus any changes in environmental conditions (temperature or flow rates) should be observed at similar timescales.

To compare these methods, an environmental chamber sets the temperature to nine temperatures, ranging from 10 °C to 50 °C, and steady-state measurements of the coated device, uncoated device, on-die resistor and external IC are recorded. These steady-state measurements are then used to estimate the temperature change ΔT in Equation 3.4 or Equation 3.2. These temperature estimates are then used in Equation 3.3 or Equation 3.5 to compensate for sensor response to the temperature shift. As there should be no change in mass, ideally, $\Delta f(t) = 0$.

Figure 3.14 shows a comparison of the discussed methods. Linear compensation with a second sensor removes the least amount of drift due to thermal interference, while a quadratic fit compensation method from the signal output from a resistor, external temperature sensor, or second cantilever perform similarly. As the quadratic fit using a secondary sensor performs similarly to the other methods and as the second sensor will behave similarly to the coated sensor for unknown interference sources (such as flow rate changes), it

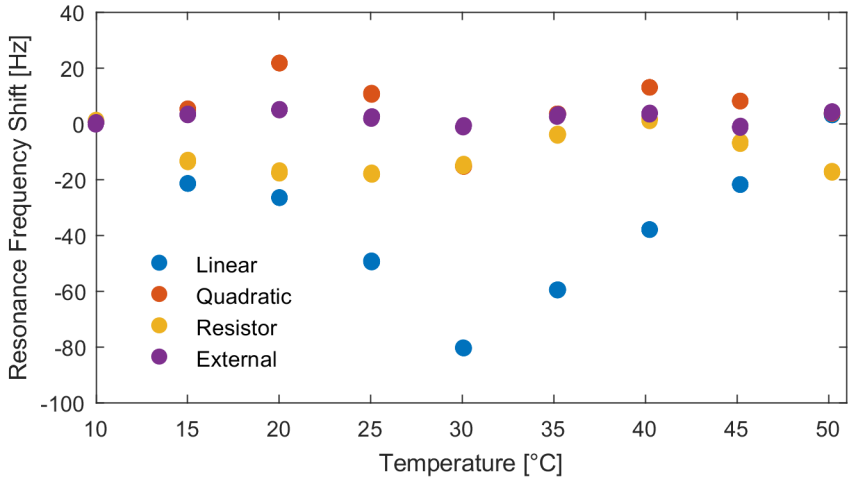

Figure 3.14: *Nominal resonance frequency shift of polymer-coated hammerhead resonator as a function of the environmental temperature after four different environmental compensation methods: an uncoated reference sensor with an assumed linear or quadratic temperature dependence, an on-die resistor and an external temperature sensor. The polymer-coated resonator has a room temperature resonant frequency of* 729.8 kHz *and a temperature coefficient of resonant frequency of* −26.9 Hz/°C *before compensation.*

will be the method of compensation utilized throughout this work.

For polymers with low melting points such as PIB, it was observed that the resonant frequency does not return to its original resonant frequency after heating the device to higher temperatures under resonant operation. Polymer softening resulting in redistribution on the sensor surface or even removal due to high angular acceleration forces likely cause this shift. This effect lessens with each succeeding temperature cycle as the easy-to-displace polymer has already been redistributed.

Figure 3.15 shows the resonant frequency shifts of PIB and OV-1-coated devices in an environmental chamber. The temperature is swept from 10 °C to 50 °C, with 30 min pauses every 5 °C. After only one cycle, the PIB-coated device in Figure 3.15a shows a 110 Hz shift after the initial temperature cycle. Over the full measurement cycle with

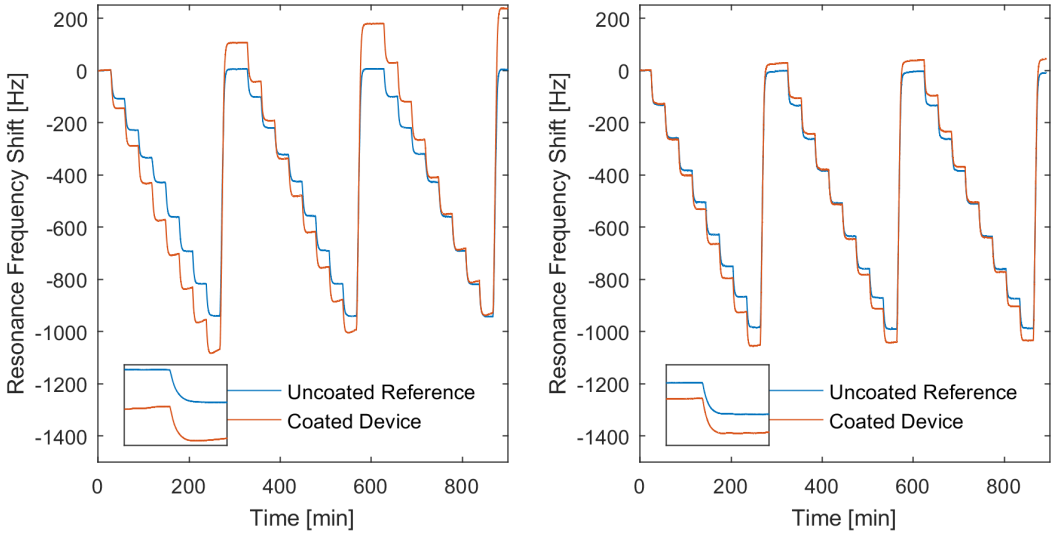

(a) *PIB* **(b)** *OV-1*

Figure 3.15: *Resonant frequency shift of (a) PIB-coated and (b) OV-1-coated sensors, each with an accompanying uncoated reference sensor, as a function of time while stepping the environmental temperature from* 10 °C *to* 50 °C *in* 5 °C *increments over three full temperature cycles. The PIB-coated device has a positive frequency shift during the measurement, especially evident at higher temperatures, and does not return to its original baseline between measurements; in contrast, the OV-1-coated device exhibits minimal frequency drift. This is indicative of the lower melting point of PIB, which is redistributed as it softens and is subject to high accelerations associated with continued oscillations at its resonant frequency.*

three temperature sweeps, the PIB device shifts approximately 240 Hz, while the OV-1-coated device in Figure 3.15b only shifts by 45 Hz. Additionally, the frequency shift due to polymer redistribution of the PIB-coated device varies with each successive temperature cycle: 110 Hz for the first, 70 Hz for the second and 60 Hz for the final temperature cycle. This presents a challenge for predictively compensating in high temperature scenarios, as an unknown amount of polymer is redistributed, and should be avoided by either limiting temperature excursions or using polymers with higher melting temperatures.

Applied heating to the film via integrated resistors manifests as an additional interference source in the resonance frequency shift. This work explores three methods to remove this interference: a pre-recorded measurement in nitrogen providing a baseline measurement; the recorded heating voltage (i.e. heating power) correlated to the expected frequency shift; and a secondary resonator located sufficiently close to the heated device so that it is thermally coupled via convection through the surrounding medium and conduction through the base. To investigate the self-heating effect, a test chip is stabilized in an environmental chamber at 20 °C and a function generator pulses the coated device's heaters with varying voltages for 5 min, allowing it to recover and return to a baseline for 10 min. Figure 3.16a shows measured resonance frequency shifts for a resonator coated with PIB and an uncoated neighboring reference resonator.

As expected, the increased temperature decreases the Young's modulus of silicon, which causes spring softening and a resonance frequency decrease. For small temperature increases, the sensors respond linearly to increased heating power, with observable deviations for the heated resonator above 20 mW. Figure 3.16b shows the linear fit for the two devices (data points above 20 mW were excluded from the fit as outliers for the heated device). The change in resonance frequency for the heated device is approximately 14.9 Hz/mW, or an estimated 20.1 Hz/°C from the simulated heating efficiency. The linear fit ratio between coated and uncoated device on this particular chip is 13.7 Hz/Hz which is used in Figure 3.17a to compensate for self-heating effects. While this fit does remove a significant

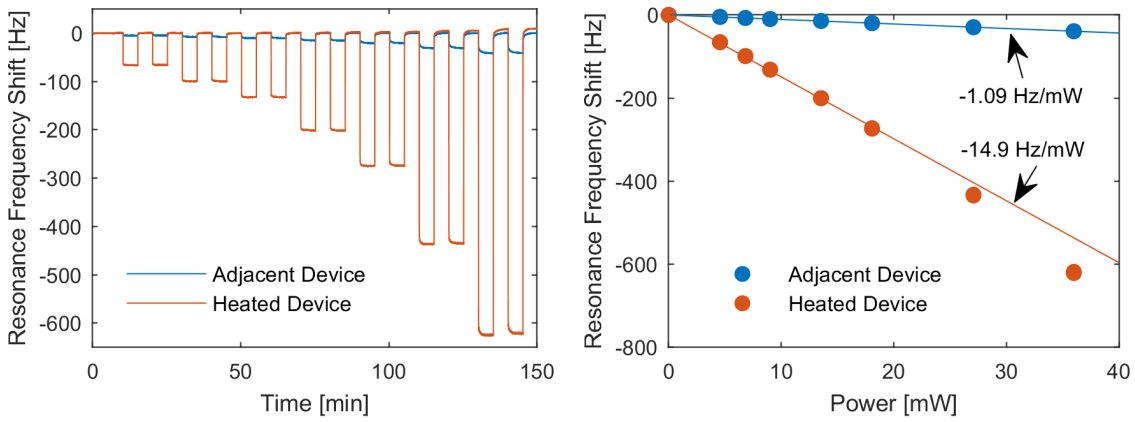

Figure 3.16: *Measured resonant frequency shift of a polymer-coated heated resonator and an uncoated and unheated adjacent resonator located on the same die to a heating pulse sequence applied to the polymer-coated resonator. Time series data (a) shows the resonant frequency shift of both devices due to spring softening from the temperature dependent Youngs modulus of silicon. Polymer redistribution on the heated devices surface causes the offset from zero at the heating sequence conclusion. The resulting resonant frequency shift as a function of applied heating power (b) is linear and corresponds to approximately* 20 Hz/°C *for the heated device.*

portion of the heating interference for lower heating powers, 10 Hz to 20 Hz of interference still remains in steady-state conditions. As an additional method, control system toolboxes (specifically in MATLAB), have unique features to create an estimated transfer function between an known input and measured output. Creating a transfer function, in this manner, between the measured applied power and resonant frequency shift in Figure 3.17b also yields an unsatisfactory shift in compensated resonant frequency at steady-state. The final method utilizes a recorded measurement, without the presence of any absorbing analyte, to subtract the frequency dependence of heating from the measured response. This technique is the least flexible as any new heating pattern or any change to the sensor requires a new reference measurement. However, as shown in Figure 3.17c it is the most effective of the techniques explored at removing self-heating effects.

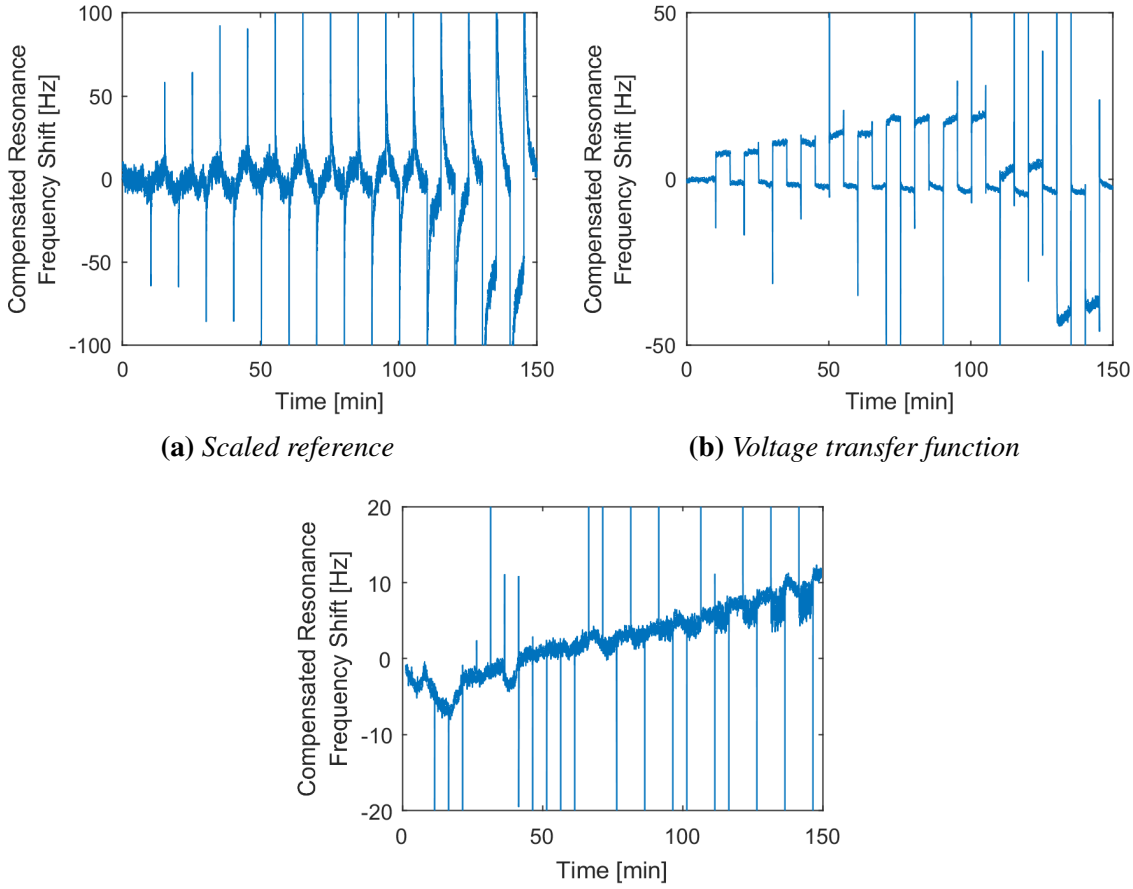

(a) *Scaled reference*

(b) *Voltage transfer function*

(c) *Pre-recorded reference*

Figure 3.17: *The coated sensor is exposed to inert gas at a constant flow rate and heating pulse pairs of* 5 mW, 7.5 mW, 10 mW, 15 mW, 20 mW, 30 mW *and* 40 mW *are applied to the heating resistors and methods to remove the effects of self-heating on the resonant frequency: (a) scaling any response of the uncoated and unheated adjacent device according to a pre-measured ratio (in this instance* 13.7 Hz/Hz *from Figure 3.16b); (b) modeling the applied heating power to frequency shift as a transfer function in MATLAB; (c) subtracting a pre-recorded measurement in inert gas from the measured resonant frequency (single sample spikes for these methods are caused by variable instrument timing).*

3.4 Chemical Measurement Procedure

For chemical and calibration measurements, the coated sensor and a neighboring uncoated device on the same die are operated in individual amplifying feedback loops with appropriate phase delays to ensure positive feedback at the resonance frequency. The U-shaped piezoresistive Wheatstone bridge (visible in Figure 3.1) design selectively rejects signals due to out-of-plane motion, while simultaneously enhancing signals from the in-plane

modes. The amplified signal from the Wheatstone bridge is fed into the excitation heating resistor located at a corner of the beam anchor point. The resulting thermal expansion due to Joule heating is used to excite the beam system and maintain resonance. A buffered signal is measured by a frequency counter with gate times ranging from 100 ms to 200 ms and recorded via a LabVIEW interface.

3.4.1 Gas Measurements

The experimental apparatus used (unless otherwise noted) in this thesis has previously been described in detail by Su [101]. It features multiple mass flow controllers, a four-way high speed pneumatic valve, glass bubblers with liquid analyte for a carrier gas (typically nitrogen N_2) to flow through, and supporting circuitry to control the gas flow and resonate the device (shown in Figure 3.18). The pneumatic four-way valve switches between an ultra-high purity nitrogen reference gas stream and an analyte-loaded gas stream from a liquid bubbler (set in a 20 °C temperature-controlled bath) that has been diluted from its Antoine equation partial pressure by nitrogen. Analyte gas concentrations dilution rates vary from 1:80 to 1:2 of analyte saturated carrier gas diluted with pure carrier gas. This enables analyte concentrations typically from hundreds to thousands of ppm.

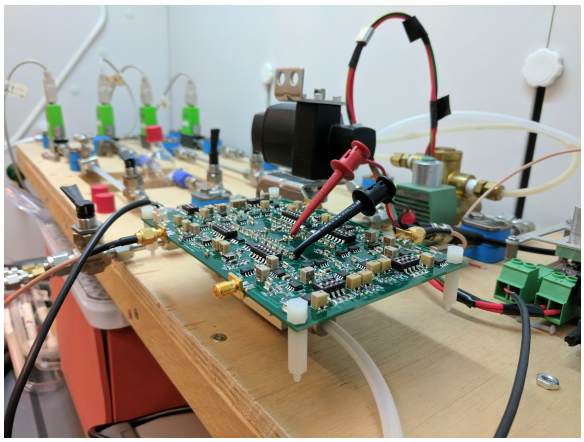

Figure 3.18: *Closed-loop resonant board connected to a resonant cantilever in the experimental setup. Mass flow controllers are visible towards the photo rear with the pneumatic high speed valve just above the circuit board.*

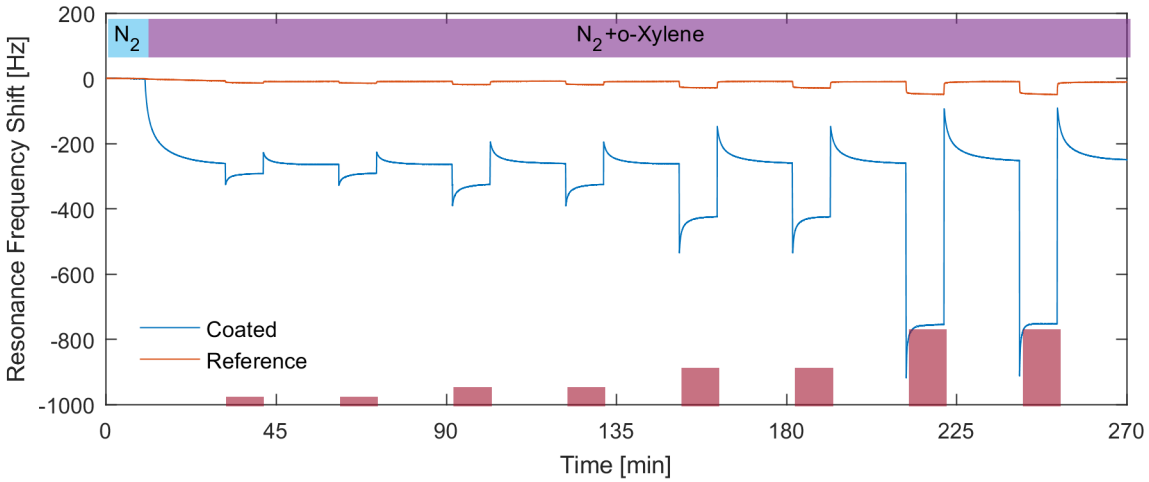

Figure 3.19: *A standard measurement sequence where nitrogen flows over the sensor (in this case a PIB-coated cantilever) until the measurement chamber is exposed to nitrogen with an analyte (*824 ppm *o-xylene). Applied heating pulses, represented by the red bars, begin after the system reaches equilibrium. For one heating pulse, the initial drop in frequency is caused by spring softening (due to silicon's temperature dependent Young's modulus).This is followed by desorption due to a decreased partition coefficient. At the conclusion of a heating pulse, the device rapidly cools to near room temperature causing the resonant frequency to increase and restoring the original partition coefficient, thus allowing analyte to re-absorb back into the sensing film.*

The hammerhead resonators are connected to the amplifying feedback loop and the resonance frequencies are measured with a frequency counter. Figure 3.19 shows the measured frequency shift for a typical chemical measurement. On experiment start, the system flows pure carrier gas over the resonator until equilibrium is reached. After equilibrium under the nitrogen carrier gas is reached, a chemical measurement begins as the 4-way valve switches from carrier gas to analyte loaded gas. The frequency drop, due to the absorbed mass or spring constant change, is recorded by a custom LabVIEW program sampling at 5-20 samples/second. The variable sampling rate is removed by re-sampling in MATLAB in post-processing. After the new equilibrium (with the analyte absorbed into the polymer film) is reached, heating pulses are delivered by a function generator or source-meter. These are identical to a previously recorded reference set of pulses with the sensor under pure nitrogen. Upon conclusion of the heating pulse chain, the valve system changes back to the pure carrier gas flow and the system is brought back to equilibrium as a reset prior to

subsequent measurements (not shown in Figure 3.19).

3.4.2 Interference Compensation

Figure 3.20 shows a graphical representation of the MATLAB procedure to remove interference and parse the measured data. The general technique used in this section will be utilized (but not necessarily shown) throughout this thesis.

Initially, the uncoated reference device compensates for environmental effects in the coated device via techniques discussed in Subsection 3.3.2. This compensation is displayed in Figure 3.20a and Figure 3.20b, for the case of N_2 exposure only and N_2 plus analyte, respectively, where drift due to environmental temperature fluctuations has been removed. Self-heating causes shifts in the reference device, which leads to some shifts due to environmental compensation. While this shift is undesirable, it is uniform across the chemical and reference measurements; therefore, it will be able to be removed during heating pulse compensation.

This compensation decreases the noise, especially at longer integration times, thus in-

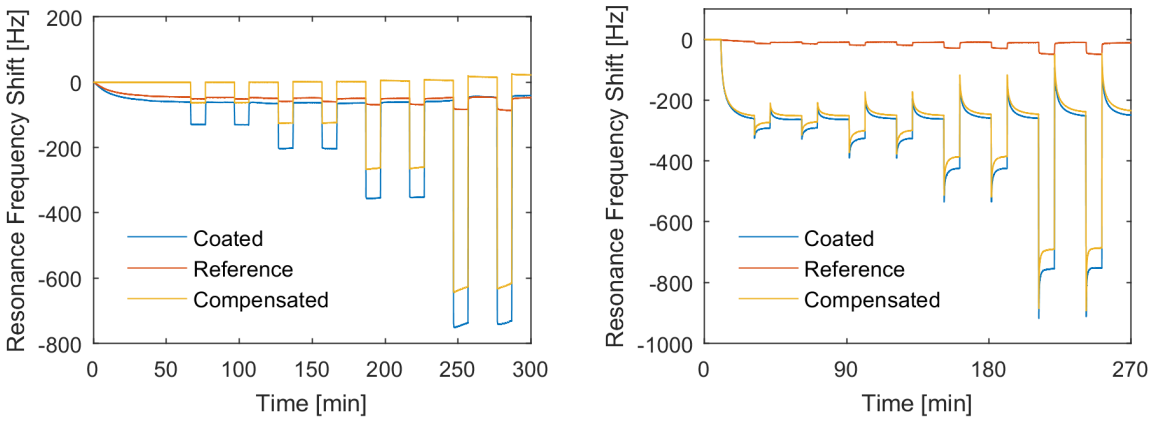

(a) N_2 *only* **(b)** $N_2 \rightarrow N_2$ + *Analyte*

Figure 3.20: *The resonant frequency shift of a PIB-coated sensor and its neighboring uncoated, reference sensor due to a heating pulse applied to the PIB-coated device's heaters when exposed to different environments: (a) pure nitrogen, (b) nitrogen plus analyte. The uncoated cantilever provides temperature compensation from environmental fluctuations during both measurements. Thus shifts not from sorption (e.g. a small frequency change in the first* 25 min *of (b)) do not influence the chemical measurement.*

creasing sensitivity by lowering the minimal detectable frequency change Δf_{min} [45]:

$$\text{LOD} = 3\frac{\Delta f_{min}}{S}, \tag{3.6}$$

where the minimum detectable frequency shift is related to the Allan Deviation, $\sigma(\tau)$, by

$$\Delta f_{min} = \sigma(\tau) \cdot f. \tag{3.7}$$

The Allan deviation is a frequency instability measurement that compares a device's neighboring frequency measurements over an integration time (τ). Short integration times highlight frequency instabilities due to random walk, while longer integration times show frequency drift [156]. The second resonator decreases the frequency drift due to environmental changes and thus allow for longer integration times, increasing frequency stability. Figure 3.21 shows the effect of a temperature/drift compensation on the Allan Deviation and, thus, sensor sensitivity. Without compensation, the minimum detectable frequency shift for the 713 kHz resonator is 9.5 mHz at an integration time of 0.79 s, while the compensation decreases this minimum detectable frequency shift by 26 % to 7.0 mHz with a

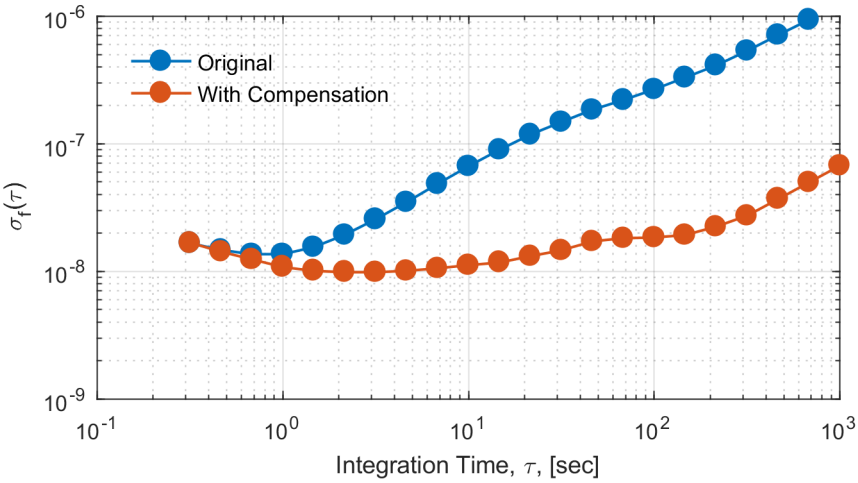

Figure 3.21: *Allan deviation as a function of gate integration time with and without temperature compensation from a neighboring (uncoated) device. The addition of temperature compensation extends the regime where averaging increases the device stability.*

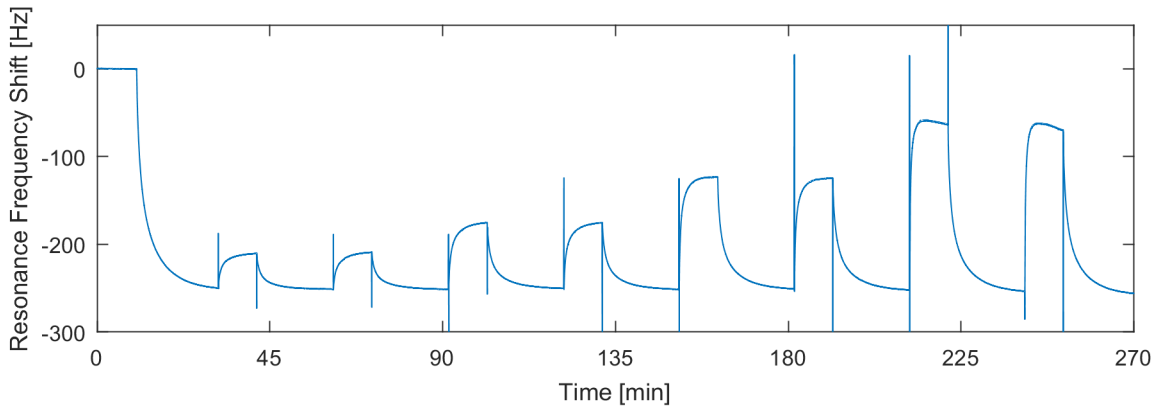

Figure 3.22: *A chemical measurement with environmental temperature effects removed with a reference cantilever and self-heating temperature effects removed with a reference measurement. Frequency shifts during and following heating pulses clearly show the analyte sorption due to the partition coefficient changes.*

2.9 s integration time.

Subtracting the frequency change of the heating pulses recorded in pure nitrogen (Figure 3.20a) from that during the chemical measurement (Figure 3.20b) results in the frequency change solely from mass desorption or absorption processes (Figure 3.22). Aligning the measurements is accomplished by finding the maximum correlation index between the recorded voltage signals. The voltage signals were chosen over the frequency measurements as there are minimal transients of the recorded signal and no sorption effects that could skew the alignment. Time mismatches due to variable sampling produce the positive and negative spikes at the beginning and end of each heating pulse. As these spikes are due to post-processing alignment inaccuracies, they are not considered for the remainder of this work. The data is then parsed to determine partition coefficient (Figure 3.23a) and diffusivity coefficient changes (Figure 3.23b).

The differing steady-state frequency shifts in Figure 3.23a correspond to a change in partition coefficient at constant analyte concentration. The normalized response in Figure 3.23b removes the effects of concentration, analyte mass and partition coefficient and highlights the change in diffusivity as the desorption time constants decrease with increasing heating power. The similar re-absorption rates suggest steady-state at the conclusion of

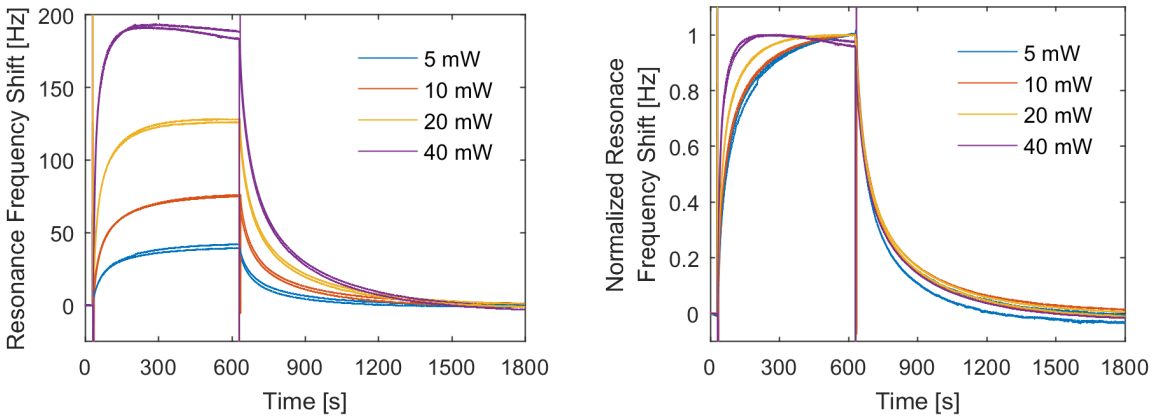

(a) **(b)**

Figure 3.23: *(a) Absolute and (b) normalized resonant frequency shift due to heating induced analyte desorption and subsequent re-absorption for heating pulses with* 10 min *lengths and varying heating powers.*

the heating pulse and a consistent re-absorption temperature irrespective of heating power.

Evident from this example is again the effect of higher heating pulses on polymer redistribution. The negative slope of the 40 mW pulse between 200 s and 600 s would seem to indicate a mass gain; however, the compensation process must be taken into consideration. In the heating reference case (Figure 3.20a), which is subtracted from the dataset, the positive frequency shift of a 40 mW pulse is approximately 15 Hz, while the negative shift in Figure 3.23a is approximately 7 Hz. The 8 Hz discrepancy is likely from the sensor losing or redistributing less polymer later in its life-cycle.

CHAPTER 4

STEADY-STATE RESPONSE AND EQUILIBRIUM ANALYSIS

Measuring the steady-state response as a function of temperature can improve the selectivity of a sensor by providing characteristic analyte properties that can help discriminate between analytes. From Section 2.2 the enthalpy of vaporization for a given analyte for small temperature changes (ΔT) from a base temperature (T_0) is

$$\Delta H_{Vap} = 2.303 \cdot R \left(\frac{T_0 \cdot (T_0 + \Delta T)}{\Delta T} \right) \cdot \log \frac{K(T_0)}{K(T_0 + \Delta T)} \tag{4.1}$$

As highlighted in Section 2.2, Equation 4.1 assumes that (1) the enthalpy of vaporization dominates the analyte sorption into the sensing film (e.g. the mixing enthalpy can be neglected) and (2) a temperature-independent ΔH_{Vap}. Approximating the temperature dependence of ΔH_{Vap} with a linear function over the small temperature range ΔT from the base temperature T_0, Equation 4.1 becomes (see Equation 2.24)

$$\Delta H_{Vap} = 2.303 \cdot R \left(\frac{T_0 \cdot (T_0 + \Delta T)}{\Delta T \cdot (1 + T_0 \cdot \frac{a}{T_c})} \right) \cdot \log \frac{K(T_0)}{K(T_0 + \Delta T)}, \tag{4.2}$$

which accounts for an estimated enthalpy change as a function of temperature (see Figure 2.4). As the mass-sensitive sensor response, i.e. the measured frequency change is $\Delta f \propto m_a C_A K(T)$, where m_a is the analyte mass, C_A is the concentration and $K(T)$ is the partition coefficient, the ratio of frequency shifts at equilibrium for two temperatures is the partition coefficient ratio $K(T_0)/K(T_0 + \Delta T)$. It should be noted that the frequency shift at a given temperature is measured with respect to the frequency without analyte. This chapter will investigate the steady-state response to analyte absorbed in the sensing film as a function of temperature and developing a method to distinguish between analytes based on this analysis.

4.1 Device Partition Coefficient Simulations

The effect of the analyte's enthalpy of vaporization on the sorption behavior of the sensing film at room temperature as well as elevated temperatures during heating can be simulated using COMSOL. Simulations estimating the partition coefficient change according to Equation 4.1 show the added mass as a function of heating power and enthalpy of vaporization, aiding the implementation of methods that accurately extract enthalpy constants from the measured sensor output.

To this end, Figure 4.1 shows the normalized simulated added mass in the sensing film for four different heating powers and four distinct vaporization enthalpies ranging from 20 kJ/mol to 50 kJ/mol. At $t = 0\,\mathrm{s}$, the analyte concentration in the sensing film and thus the (normalized) absorbed mass are zero. Between $t = 0s$ to $500s$, the analyte diffuses into the sensing film at room temperature ($T = 20\,^{\circ}\mathrm{C}$), assuming a film thickness of 5 µm and an analyte/polymer-specific diffusivity of 1×10^{-9} cm^2/s. At $t = 500\,\mathrm{s}$, the heating pulse with varying heating power starts. As the applied power heats the resonator structure and film, at a thermal time constant significantly faster than the diffusion time constant (see Subsection 3.1.1), the partition coefficient decreases as is calculated from Equation 4.1 according to the given vaporization enthalpy and simulated temperature increase, causing the previously absorbed species to desorb out of the sensing film. The time-dependent COMSOL simulation models the change in partition coefficient resulting from the increasing film temperature at the film-gas interface by adjusting the analyte concentration boundary condition at the film-gas interface according to the reduced partition coefficient. It should be noted that the analyte diffusivity is modeled as not being temperature-dependent in this particular simulation.

Figure 4.1 demonstrates how the varying heating power and vaporization enthalpy affects a typical measurement. As expected, an increasing heating power and, thus, increasing sensor temperature causes more analyte to desorb from the sensing film. More im-

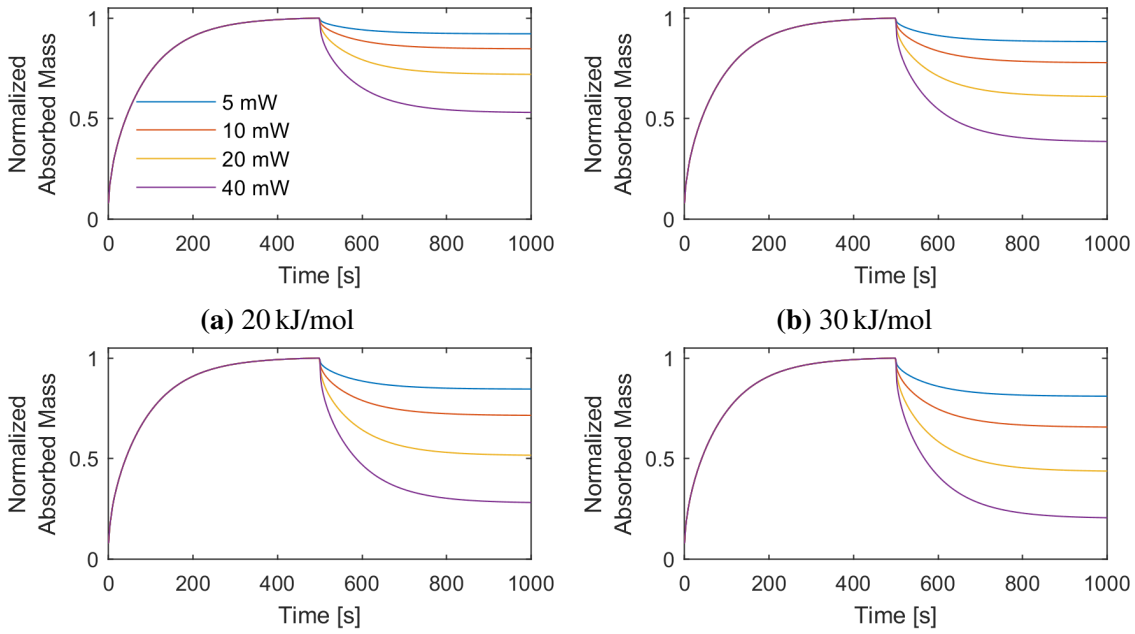

(a) 20 kJ/mol **(b)** 30 kJ/mol

(c) 40 kJ/mol **(d)** 50 kJ/mol

Figure 4.1: *Simulated normalized absorbed mass in the sensing film during initial analyte absorption followed by heating-induced analyte desorption for analytes with different vaporization enthalpies and four heating powers. Initially, the polymer is at room temperature (*20 °C*) and devoid of the simulated analyte species. The analyte concentration boundary conditions at the film-gas interface as a function of temperature governs diffusion into the sensing film. At* $t = 500\,\mathrm{s}$ *the heating pulse changes the film temperature, thus reducing the analyte concentration at the film surface, causing the analyte to desorb.*

portantly, an increase vaporization enthalpy results in more analyte desorbing from the sensing film at a given heating power, because of the increase partition coefficient ratio $K(T_0)/K(T_0 + \Delta T)$ (see also Equation 4.1).

4.2 Film Temperature

Essential to enthalpy estimation and subsequent analyte identification using Equation 4.1 is an accurate film temperature measurement. The film-gas/analyte interface temperature modifies the partition coefficient K, and thus the boundary conditions from Equation 2.2. The bulk film temperature also modifies the diffusivity coefficient which will be the subject of Chapter 5. While initial thermal simulations of the hammerhead resonator show an approximate average heating efficiency of 0.75 °C/mW and 0.60 °C/mW for 20 µm and 25 µm

thick devices built on SOI wafers, respectively, uncertainty in the final device dimensions (especially thickness) require appropriate measurement of the film temperature. In this thesis, a direct and indirect way to assess the film temperature were investigated besides above modeling approach:

1. Direct measurements of the film temperature via measuring the temperature-dependent resistance of the heating resistor.

2. Indirect measurement of the film temperature via fitting the experimental results using analytes with known vaporization enthalpies to Equation 4.1.

The temperature of the sensing film can be estimated by measuring the resistance in the doped silicon heating resistors. Figure 4.2a shows the measured resistance of the heating resistors in an environmental chamber as a function of temperature. A Keithley 2400 source meter applies 100 µA of current (≈8 µW) to limit self heating, while measuring the four-wire resistance of the doped resistors. Measurements recorded in 5 °C increments from 20 °C to 50 °C are represented as symbols in Figure 4.2a, while the solid line represents a second order fit through the measured points, where

$$R(T) = a \cdot T^2 + b \cdot T + c. \tag{4.3}$$

By measuring the heating resistance during self-heating, while an environmental chamber maintains a constant temperature (10 °C, 20 °C or 30 °C), the above temperature calibration can now be used to convert the measured resistance into a temperature increase or to estimate the heating-power efficiency coefficient according to Equation 4.8.

$$T = P \cdot \eta + T_0 \tag{4.4}$$

$$T_0 + \Delta T = I^2 R(T) \cdot \eta + T_0 \tag{4.5}$$

$$\Delta T = I^2 R(T) \cdot \eta \tag{4.6}$$

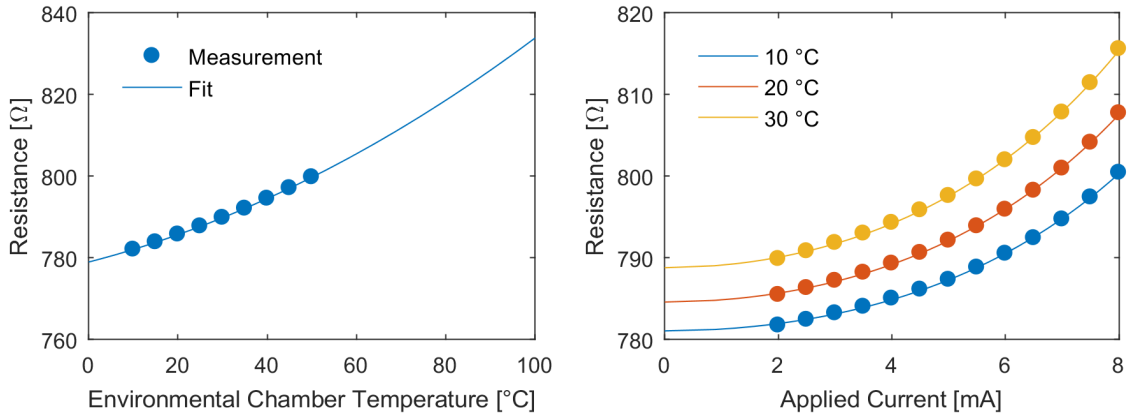

Figure 4.2: *(a) Four-wire resistance of the three heating resistors as a function of the environmental chamber temperature. The resistance was measured using a Keithley 2400 source-meter, applying a probing current of* 100 µA. *(b) Four-wire resistance of the three heating resistors as a function of the current applied by the Keithley 2400 source-meter for three different environmental temperatures.*

$$\Delta T = I^2 \left[aT^2 + bT + c\right] \cdot \eta \tag{4.7}$$

$$\Delta T = I^2 \left[a\left(T_0 + \Delta T\right)^2 + b\left(T_0 + \Delta T\right) + c\right] \cdot \eta \tag{4.8}$$

Similar to the previous experiment, a Keithley 2400 source-meter measures the four-wire resistance, while sourcing increasing current, while the packaged chip resides in an environmental chamber. The resistance as a function of applied current is shown in Figure 4.2b for the three different environmental chamber temperatures.

Figure 4.3 shows the extracted estimated temperature rise as a function of the applied heating current and heating power, using the calibration measurement from Figure 4.2 and Equation 4.8. Best fits result in heating efficiencies between 0.83 °C/mW and 0.89 °C/mW, which is a significant deviation from the simulated values. It is believed that this deviation is due to the dual nature of the resistors for heating and temperature sensing and the fact that the resistors are doped resistors. The higher voltages applied during heating (compared to the temperature calibration) modify the depletion region of the pn-junction between p-type heater and n-type device layer and, thus, affect the measured resistance besides the

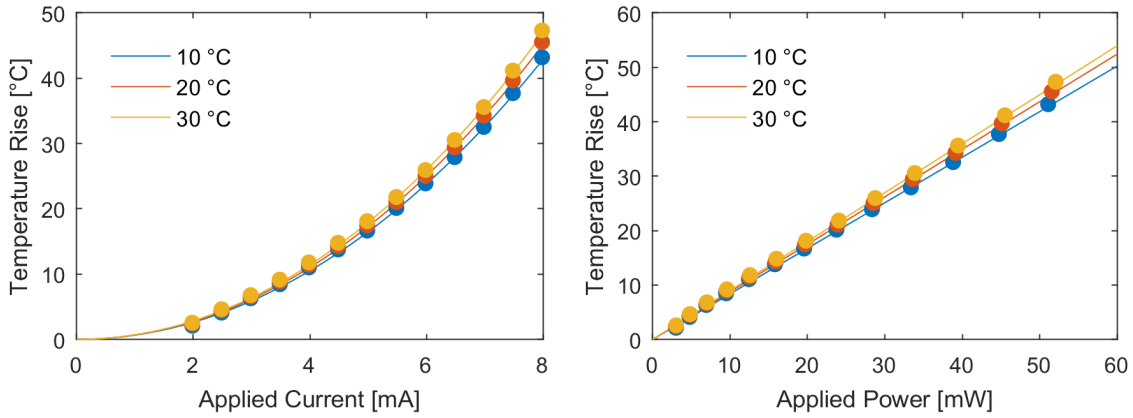

Figure 4.3: *Estimated temperature rise as a function of the applied heating current (a) and heating power (b). As expected, the temperature increase is linear with applied power and a heating power efficiency ranging from* 0.83 °C/mW *to* 0.89 °C/mW.

temperature. An increasing voltage would widen the depletion region and thus increase the resistance, similar to the effect of temperature. Future designs should thus include additional resistive elements on the hammerhead structure specifically for temperature sensing that are excluded from the heating circuit, thus separating the heaters and temperature sensor. For the present work, the heating efficiency was instead estimated by a fitting approach described in the following.

Reference measurements with analytes of known vaporization enthalpies, such as in the simulated cases of Figure 4.1, can provide a calibration measurement that allows extraction of the heating power efficiency. Assuming that the temperature increase of the sensing film is directly proportional to the applied heating power, $\Delta T = \eta P$, with η being the heating efficiency, Equation 4.1 can be rewritten as:

$$\log \frac{K(T_0)}{K(T_0 + \Delta T)} = \frac{\Delta H_{Vap}}{2.303 \cdot R} \cdot \frac{\eta \cdot P}{(\eta \cdot P + T_0) \cdot T_0}, \tag{4.9}$$

where the enthalpy of vaporization (ΔH_{Vap}) and the heating power (P) are variable inputs and the initial temperature is represented as T_0. If one now measures the partition coefficient ratio $K(T_0)/K(T_0 + \Delta T)$ for a given device and sensing film for an analyte

with known ΔH_{Vap} as a function of the heating power P, a best fit against Equation 4.9 can be used to extract the heating efficient η and thus the temperature increase indirectly. While in reality, ΔH_{Vap} is not the only temperature dependent term from Equation 2.6, but only contains the dominant temperature effects. Thus, fitting to this equation can result in an approximated film temperature only. Accounting for the mixing vaporization enthalpy Equation 4.9 becomes:

$$\log \frac{K(T_0)}{K(T_0 + \Delta T)} = \frac{\Delta H_{Vap} - \Delta H_{Mix}}{2.303 \cdot R} \cdot \frac{\eta \cdot P}{(\eta \cdot P + T_0) \cdot T_0}. \tag{4.10}$$

and solved for the heating power efficiency as:

$$\eta = -\log \frac{K(T_0)}{K(T_0 + \Delta T)} \cdot \frac{2.303 \cdot R \cdot T_0^2}{P \cdot \left(2.303 \cdot R \cdot T_0 \cdot \log \frac{K(T_0)}{K(T_0 + \Delta T)} - (\Delta H_{Vap} - \Delta H_{Mix})\right)}. \tag{4.11}$$

Thus, as $2.303 \cdot R \cdot T_0 \cdot \log \frac{K(T_0)}{K(T_0+\Delta T)} < \Delta H_{Vap}$ in cases where the $\Delta H_{Vap} \not\gg \Delta H_{Mix}$, the fitted effective heating power η will increase. In this instance, the ΔH_{Mix}, which is the energy required or released upon mixing, can change the effective heating power efficiency as it can reduce or increase the amount of energy required for the vaporization phase change.

To demonstrate this approach, Figure 4.4 shows the partition coefficient ratios extracted from the simulations in Figure 4.1 as a function of the known ΔH_{Vap} and a fitted temperature increase (that must be proportional to P) so that the data points are best described by Equation 4.9 in case of a 25 µm thick device. For this analysis, the extracted heating power efficiency (η) from the fit is 0.612 °C/mW, very close to the expected efficiency of 0.61 °C/mW for the device based on the average simulated film temperature. This close match to the simulated value also shows that the mixing enthalpy for PIB and the fitted analytes is much less than the vaporization enthalpy.

Figure 4.5 further demonstrates this method with measured partition coefficient ratios

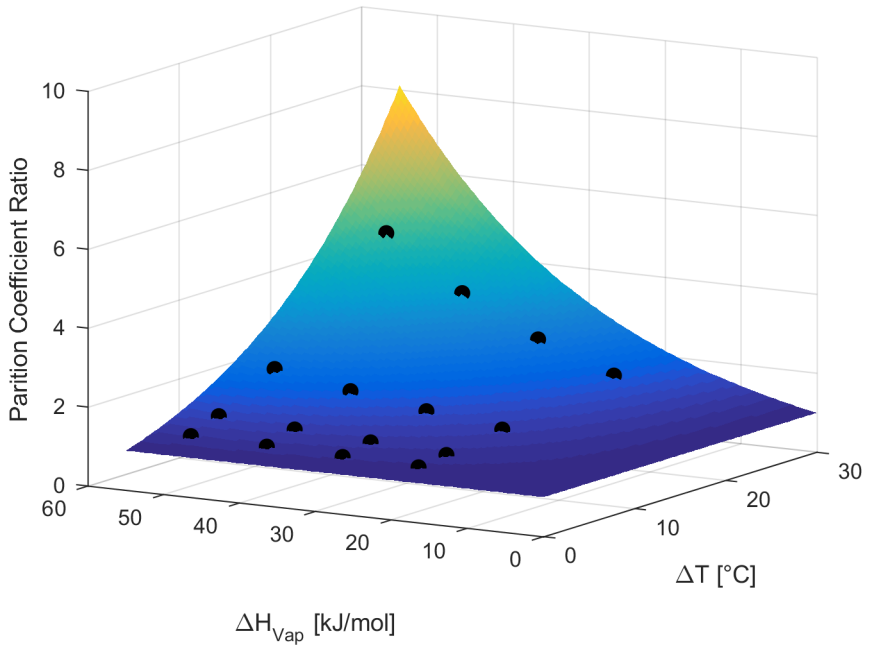

Figure 4.4: *Partition coefficient ratio $K(T_0)/K(T_0 + \Delta T)$ from the simulation in Figure 4.1 as a function of the vaporization enthalpy ΔH_{Vap} and the extracted film temperature $\Delta T = nP$ so that the data is best described by Equation 4.9.*

from a 25 µm thick, PIB-coated sensor to four heating pulses in atmospheres with varying levels of o-xylene, toluene, pentane and chloroform. Similar to the previous analysis, the known powers were fitted to a temperature increase with a best fit to Equation 4.9. For this analysis with four analytes as references, the extracted heating power efficiency is 0.5906 °C/mW, also very close to the simulated 0.61 °C/mW.

Finally, the resonance frequency itself could be used to estimate the sensing film temperature. While the resonant frequency changes as a function of temperature in Subsection 3.3.2 have already been shown to be an effective measure a cantilever's temperature, the hammerhead shape and resistive heater locations limit the effectiveness of this technique. As the beam region closest to the anchor point, which contains the regions of highest stress and strain, has the largest impact on device resonant frequency, the small temperature rise in this region by design limits coupling from heating on the distal end to a measured response. Calibration would require a known temperature and the same heating profile, through the high stress and strain regions, as achieved with the heaters; this is unlikely to

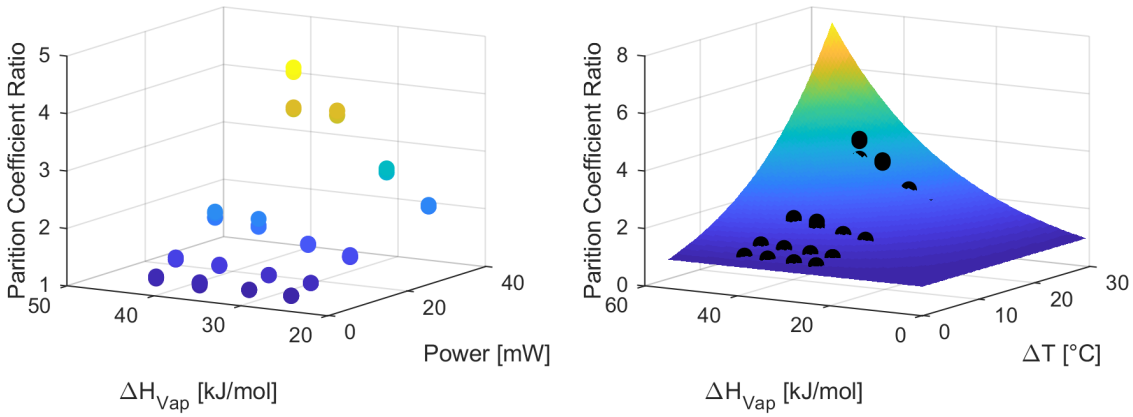

Figure 4.5: *(a) Measured partition coefficient ratio from multiple analytes subject to four heating powers. (b) The measured partition coefficient ratios are fitted to Equation 4.9. This determines the effective heating power efficiency. The fit (*0.5906 °C/mW*) agrees well with simulation.*

be achieved as most methods utilize a temperature controlled oven with uniform temperature for calibration measurements. Additionally, during chemical measurements, sorption of the chemical species will interfere with temperature measurements from observed resonant frequency shifts, preventing a real-time calculation.

4.3 Measured Sensor Response

Chemical measurements were performed with multiple analytes and absorbing films according to the measurement procedure highlighted in Section 3.4. Thereby, the custom gas mixing setup depicted in Figure 3.18 generated analyte-carrier gas mixtures, with analyte concentrations ranging from 2-15% of the Antoine coefficient defined saturation concentrations at a bath temperature of 20 °C. Typical analyte concentrations tested ranged from hundreds to tens of thousands of ppm. Table 4.1 shows a sample of the gas concentrations used in this thesis. A dilution of 2:80 refers to 2 sccm flow rates through the temperature-controlled analyte bubbler mixed with a reference gas (N_2) for a total flow rate of 80 sccm. While the tested analyte concentrations vary over multiple orders of magnitude depending on the analyte used, the analysis remains unchanged so long as the concentration does not

Table 4.1: *Vaporization enthalpies and typical concentrations for analytes used in this thesis. A dilution of 2:80 refers to* 2 sccm *flow rates through the temperature-controlled analyte bubbler mixed with a reference gas (N_2) for a total flow rate of* 80 sccm*. The analyte bubblers were kept at a constant temperature of* 20 °C*.*

Analyte	ΔH_{Vap} [kJ/mol]	Dilution 2:80 [ppm]	Dilution 10:80 [ppm]
Benzene	33.9 ± 0.1	$2,500$	$12,500$
Chloroform	31.32 ± 0.08	$5,300$	$26,500$
Ethyl Benzene	41.0 ± 4	240	$1,200$
o-Xylene	42.0 ± 5	170	850
Pentane	26.5 ± 0.6	$14,000$	$70,000$
Toluene	37.0 ± 3	740	$3,700$

affect the polymer absorption characteristics.

Figure 4.6, Figure 4.7, and Figure 4.8 show the measured frequency changes of hammerhead resonators coated with OV-1, PEUT and PIB, respectively, to the analytes listed in Table 4.1 for different applied heating powers. Thereby, an Agilent 33220A function generator supplies the embedded heating resistor with 180 s long heating pulses of 5 mW to 40 mW. Environmental and heating effects were removed according to Section 3.4. Thus, the displayed frequency change is solely due to analyte desorption from the sensing film during heating and analyte re-absorption after the completion of the heating pulse. The secondary y-axis shows the frequency change normalized by the ambient temperature equilibrium response, i.e. the room-temperature frequency response while switching from reference gas to analyte-loaded gas stream. Doing this removes the steady-state responses' dependency on analyte concentration and mass. As heating power efficiencies vary device-to-device due to process variations from fabrication, film properties, and film deposition quality, the tendency to equate the normalized device-to-device measurements should be avoided (i.e. comparisons between normalized frequency responses should only be made for equivalent temperatures). Spikes occurring at the beginning or end of a heating pulse cycle are alignment artifacts stemming from variable sampling rates between the gas and reference measurements (as discussed in Subsection 3.4.2).

Fitting known vaporization enthalpies (similar to what was described in Section 4.2)

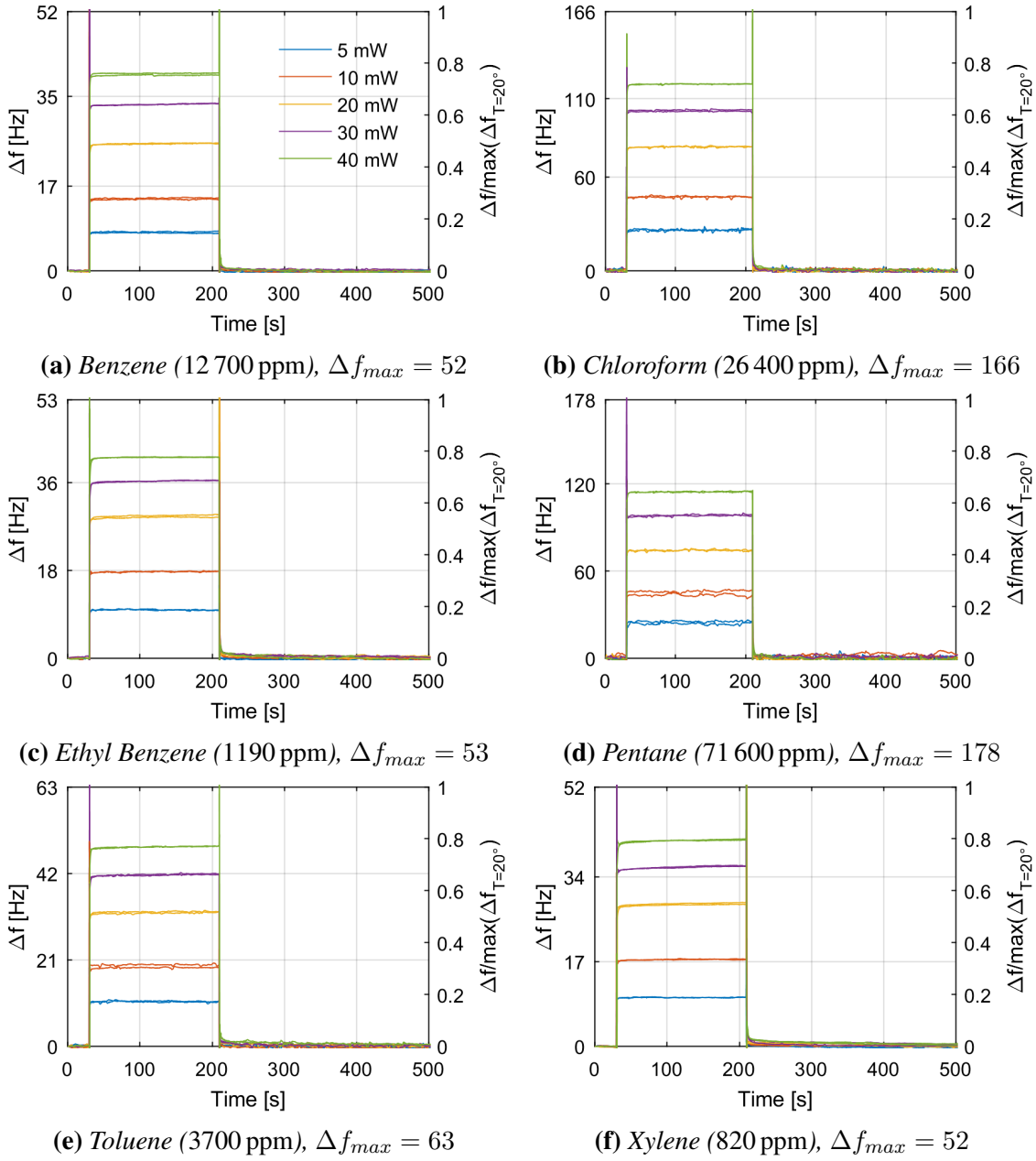

(a) *Benzene (*12 700 ppm*),* $\Delta f_{max} = 52$ **(b)** *Chloroform (*26 400 ppm*),* $\Delta f_{max} = 166$

(c) *Ethyl Benzene (*1190 ppm*),* $\Delta f_{max} = 53$ **(d)** *Pentane (*71 600 ppm*),* $\Delta f_{max} = 178$

(e) *Toluene (*3700 ppm*),* $\Delta f_{max} = 63$ **(f)** *Xylene (*820 ppm*),* $\Delta f_{max} = 52$

Figure 4.6: *Measured absolute resonant frequency shift of a hammerhead resonator coated with* 29 ng *(see Figure B.2) of OV-1 as a function of time while heating the resonator for* 180 s *at different heating powers during exposure to six analytes at constant concentration. The secondary y-axis normalized the measured frequency shift by the frequency shift* f_{max} *measured at room temperature while switching from analyte-loaded gas to reference gas (valve-generated transient). The short sorption time constants observed are consistent with a thin polymer coating* ≈790 nm*. The base resonance frequency of the OV-1 coated hammerhead is* 744 kHz*.*

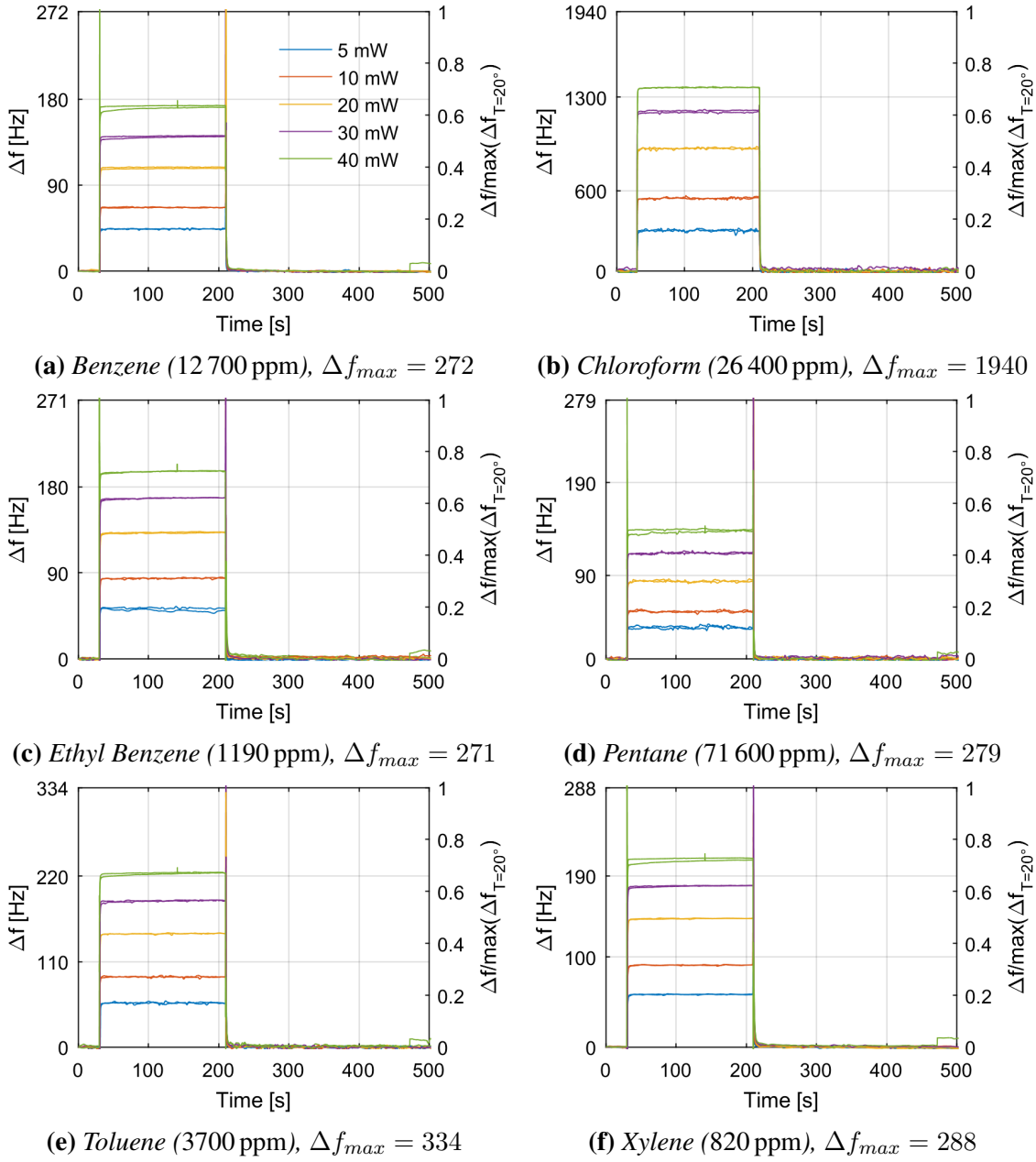

(a) *Benzene (*12 700 ppm*),* $\Delta f_{max} = 272$ **(b)** *Chloroform (*26 400 ppm*),* $\Delta f_{max} = 1940$

(c) *Ethyl Benzene (*1190 ppm*),* $\Delta f_{max} = 271$ **(d)** *Pentane (*71 600 ppm*),* $\Delta f_{max} = 279$

(e) *Toluene (*3700 ppm*),* $\Delta f_{max} = 334$ **(f)** *Xylene (*820 ppm*),* $\Delta f_{max} = 288$

Figure 4.7: *Measured absolute resonant frequency shift of a hammerhead resonator coated with* 149 ng *(see Figure B.3) of PEUT as a function of time while heating the resonator for* 180 s *at different heating powers during exposure to six analytes at constant concentration. The secondary y-axis normalized the measured frequency shift by the frequency shift* f_{max} *measured at room temperature while switching from analyte-loaded gas to reference gas (valve-generated transient). Despite the thick* 4.06 µm *coating, this sensors shows shows short sorption time constants. The base resonance frequency of the PEUT coated hammerhead is* 727 kHz*.*

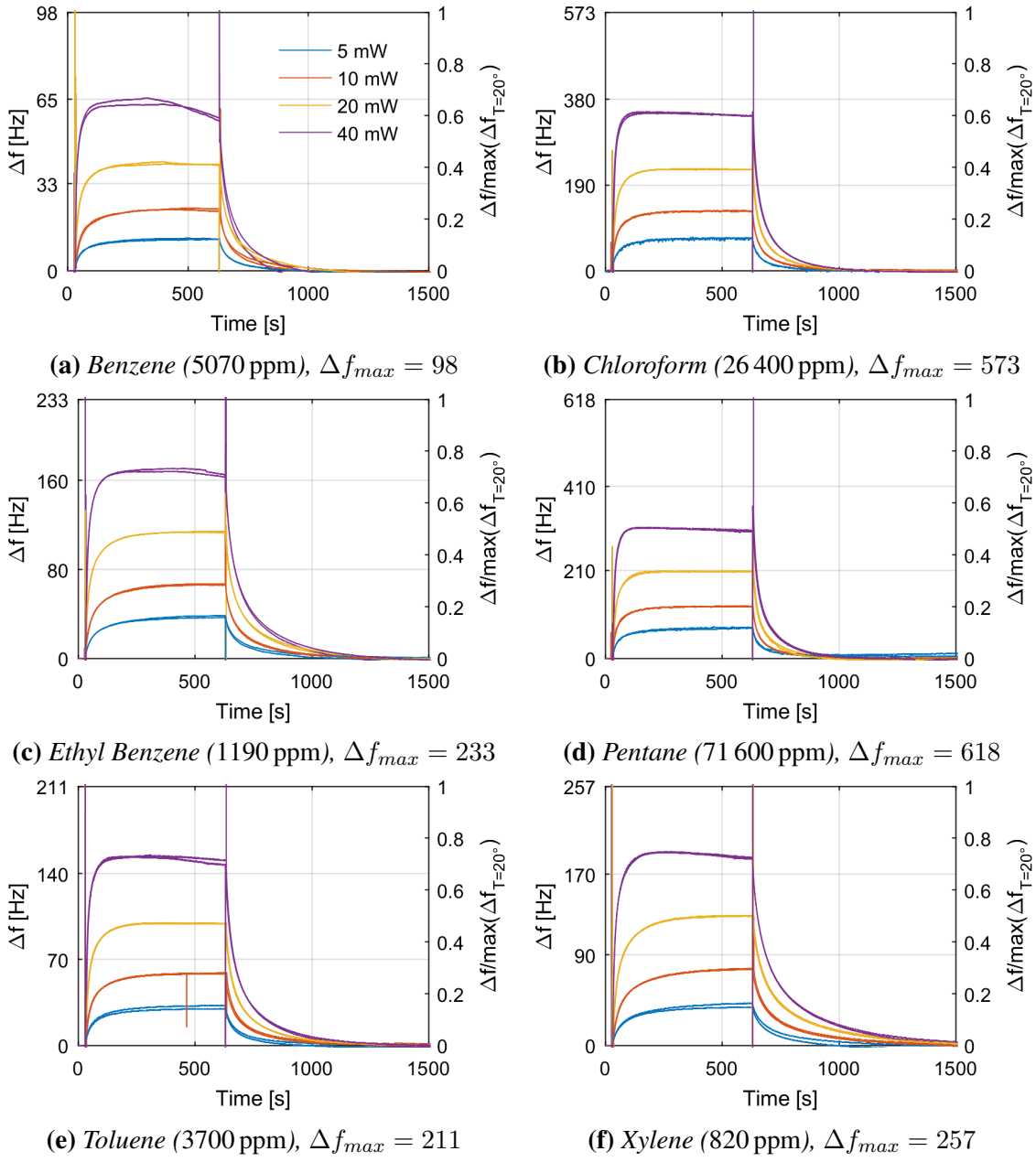

(a) *Benzene (*5070 ppm*),* $\Delta f_{max} = 98$

(b) *Chloroform (*26 400 ppm*),* $\Delta f_{max} = 573$

(c) *Ethyl Benzene (*1190 ppm*),* $\Delta f_{max} = 233$

(d) *Pentane (*71 600 ppm*),* $\Delta f_{max} = 618$

(e) *Toluene (*3700 ppm*),* $\Delta f_{max} = 211$

(f) *Xylene (*820 ppm*),* $\Delta f_{max} = 257$

Figure 4.8: *Measured absolute resonant frequency shift of a hammerhead resonator coated with* 215 ng *(see Figure B.5) of PIB as a function of time while heating the resonator for* 180 s *at different heating powers during exposure to six analytes at constant concentration. The secondary y-axis normalized the measured frequency shift by the frequency shift* f_{max} *measured at room temperature while switching from analyte-loaded gas to reference gas (valve-generated transient). The slow time constant is indicative of a thick polymer coating (*≈6.1 µm*). The base resonance frequency of the PIB coated hammerhead is* 713 kHz.

estimates the heating power efficiencies for the used devices to be 0.78 °C/mW, 0.651 °C/mW, 0.617 °C/mW for the OV-1, PEUT and PIB-coated sensors, respectively. Using one or two reference analytes is sufficient for accurate estimations (e.g fitting to only a single analyte estimates the PIB-coated device's heating power efficiency as 0.629 °C/mW). As the PEUT and OV-1 film coatings are on heated cantilevers contained on the same die, and with minimal process variations across the die, their true heating power efficiencies are likely matched and closer to the simulated value. Therefore, mixing enthalpies for the PEUT and OV-1 films likely contribute to the estimated increase in heating power efficiency from simulation (see Equation 4.10). Thus, for these films, the estimated ΔH_{Vap} using Equation 4.1 is less useful in directly measuring the enthalpy of vaporization, but will still provide ΔH_{Vap} correlated data for analyte discrimination.

As expected, the analytes with lower vaporization enthalpies (e.g. pentane) result in smaller normalized responses to the heating pulses compared to analytes with higher enthalpies (e.g. o-xylene). The time needed to reach steady-state for both OV-1 and PEUT is only a few tens of seconds, because of the thinner films. This allows for shorter pulses, reducing the overall power consumption of the device. Differing time constants will be discussed in Chapter 5. The overlapping plots depicted in Figure 4.6, Figure 4.7, and Figure 4.8 show the repeatability of this measurement technique.

Device and film stability, especially at higher heating powers, limit the measurement accuracy. Figure 4.8a and Figure 4.8c show a distinct decrease in the resonant frequency shift for the 40 mW heating pulse, while the measurements for the remaining analytes with the PIB sensor show more subtle frequency decreases for the same power of 40 mW. Changes in polymer distribution on the sensing region of the cantilever cause this interference, as any redistribution or loss of material affects the resonant frequency and sorption characteristics. As these shifts can occur during a reference measurement, a chemical measurement or the sensor idling between measurements, compensating for these shifts remains a challenge. Thus, measurements for lower melting point polymers, such as PIB, operated at high heat-

ing powers should be avoided. This mode of interference would be less distinct in sensors where the sensing mode does not rely on mechanical resonance, such as chemicapacitors or chemiresistors.

Figure 4.9 shows a point-by-point vaporization enthalpy extraction based on Equation 4.1 and the fitted heating power efficiency. The partition coefficient ratio needed for Equation 4.1 is calculated by dividing the steady-state frequency shift obtained through valve switching (f_{max}) at room temperature by the shift between analyte exposure at elevated temperature and no analyte exposure at room temperature ($f_{max} - f_{heat}$). Section 6.2 explores methods to remove the dependence on room temperature, valve-generated transients.

The general trends in acquired data match previously known values. The OV-1-coated device performed best for the analytes tested, accurately matching known enthalpy values, with an error less than 5% on average. Figure 4.10 shows a visual comparison of this method, focusing on benzene, toluene and xylene (BTX) measurements detected by the OV-1-coated sensor. This group of chemicals differ chemically only by the number of methyl groups added to the benzene ring (one for toluene and two for xylene). Figure 4.10a shows the normalized frequency shifts for the analytes. The tight grouping of data points (four data points per grouping are visible with high magnification) highlights the repeatability and discrimination ability of this method. While the measurements in Figure 4.10b are not exact values of ΔH_{Vap} (due to the influence of ΔH_{Mix}), clearly visible are three distinct vaporization enthalpy values.

Fitting multiple measurements taken at different temperatures to Equation 4.1 can remove some noise associated with individual measurements. Figure 4.11 fits the acquired points using a non-linear least squares fit in MATLAB, first grouped by sensing film then using all acquired data points and the appropriate estimated temperatures. Table 4.2 shows the extracted enthalpy of vaporization values for these fits. While deviations from literature exist, the trends correlate well with established values and are useful inputs to a

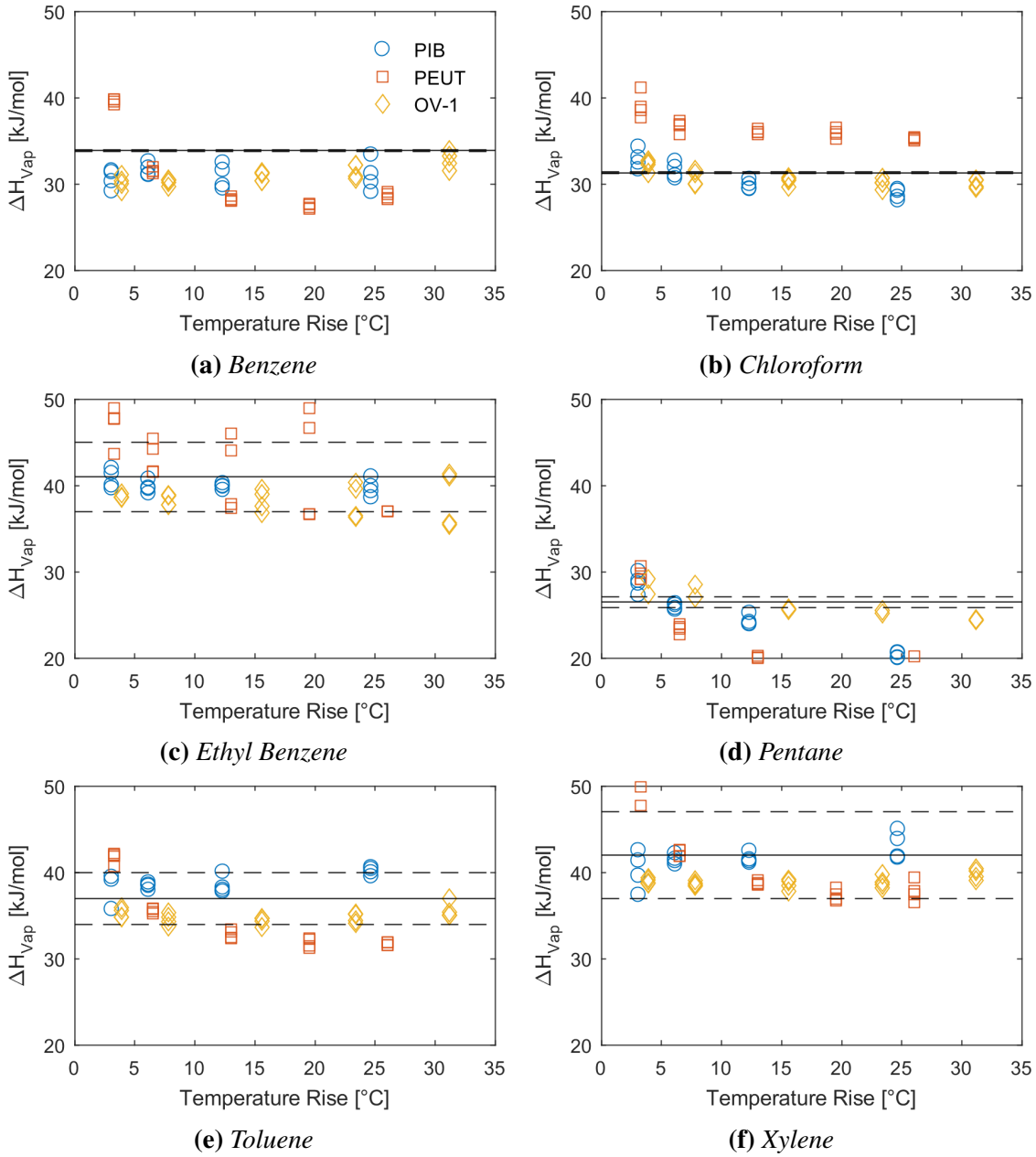

(a) *Benzene* **(b)** *Chloroform*

(c) *Ethyl Benzene* **(d)** *Pentane*

(e) *Toluene* **(f)** *Xylene*

Figure 4.9: *Vaporization enthalpies calculated from measurement data displayed in Figure 4.6, 4.7 and 4.8 based on Equation 4.1 and the fitting method described in Section 4.2 as a function of the temperature increase by heating for the three tested polymers and six analytes. The average literature values are represented by the solid black line with accepted ranges indicated between the dashed lines. Four data points for each measurement, typically overlapping, display high reliability for this technique. OV-1 results (yellow symbols) consistently more closely match literature values compared to the other two polymers and have less temperature variation.*

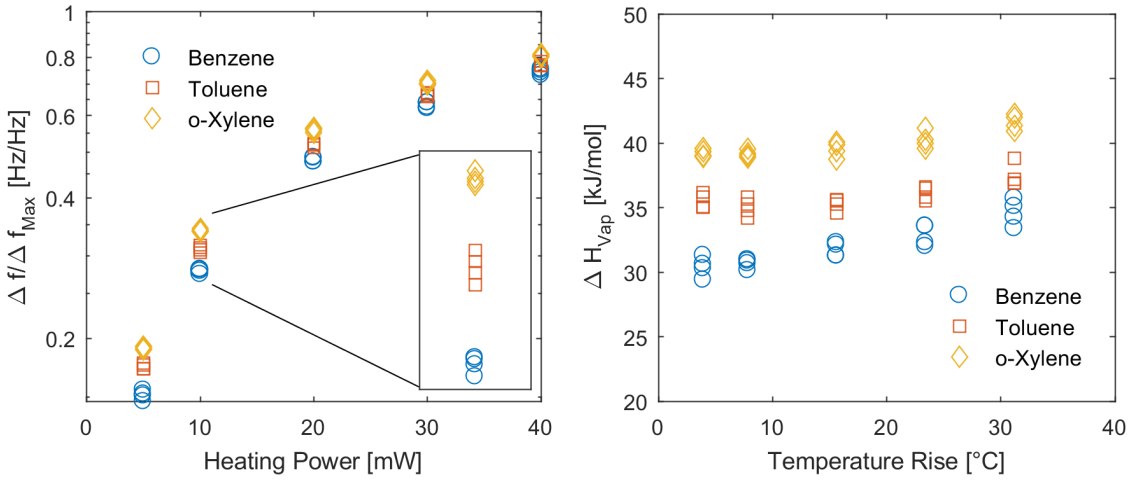

Figure 4.10: *A comparison of normalized change in frequency as a function of applied power (a) and extracted vaporization enthalpies as a function of estimated temperature (b) from data displayed in Figure 4.6 for benzene, toluene and o-xylene. Each analyte-power/temperature cluster is a tight group of four data points with no overlapping regions with the other analytes.*

multi-parameter approach discriminate between analytes (see Chapter 7). The OV-1 coated sensor is typically the most accurate in estimating the vaporization enthalpy and has an average error of 1.01%.

Table 4.2: *Extracted enthalpies of vaporization for the six analytes and the polymer coatings compared to known literature values and ranges. Measurement confidence intervals typically overlap with the known reference values.*

	Enthalpy of Vaporization [kJ/mol]				
Analyte	Reference	PIB	PEUT	OV-1	Combined
Benzene	33.9 ± 0.1	32.36 ± 0.88	29.74 ± 0.44	34.04 ± 0.61	32.61 ± 0.60
Chloroform	31.32 ± 0.08	30.31 ± 0.32	36.85 ± 0.15	31.75 ± 0.24	33.01 ± 0.70
Ethyl Benzene	41.0 ± 4.0	41.09 ± 0.47	47.30 ± 4.02	40.14 ± 1.25	42.30 ± 1.68
o-Xylene	42.0 ± 5.0	44.37 ± 0.82	39.20 ± 0.54	41.23 ± 0.41	41.25 ± 0.54
Pentane	26.5 ± 0.6	22.30 ± 0.74	20.94 ± 0.38	26.44 ± 0.24	23.33 ± 0.79
Toluene	37.0 ± 3.0	41.34 ± 0.53	33.26 ± 0.27	37.04 ± 0.49	36.85 ± 0.76

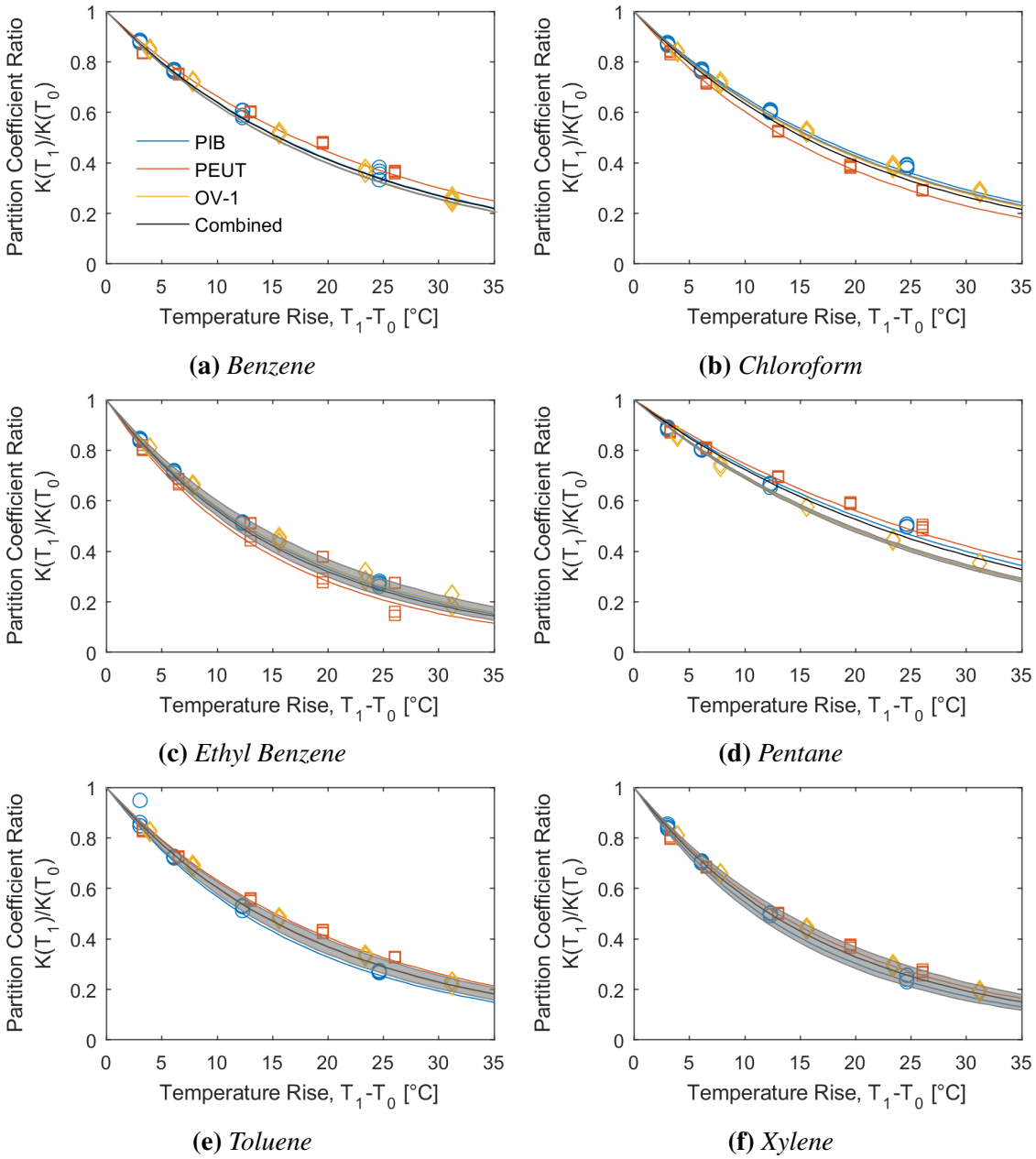

(a) *Benzene* **(b)** *Chloroform*

(c) *Ethyl Benzene* **(d)** *Pentane*

(e) *Toluene* **(f)** *Xylene*

Figure 4.11: *Partition coefficient ratio as a function of temperature rise from* 20 °C *for the three polymers. The solid colored lines represent non-linear least squares fits through all the points of a particular polymer (using Equation 4.1). The solid black lines show the fitted relationship using the combined dataset. The gray region indicates the expected behavior based on vaporization enthaplies and their uncertainties from literature known values.*

4.4 Effects of Concentration

Importantly, the effects of analyte concentration must not significantly affect the steady-state measurement analysis of Section 4.3. While the steady-state frequency change with respect to the frequency without analyte depends on analyte concentration, both in the heated and unheated case, the normalization by f_{max} should ideally remove this concentration dependence. To verify this Figure 4.12 and Figure 4.13 show the response of a PEUT-coated resonator at varying heating powers to different concentrations of o-xylene. Unlike the measurement procedure described in Section 3.4, the sensor heaters were con-

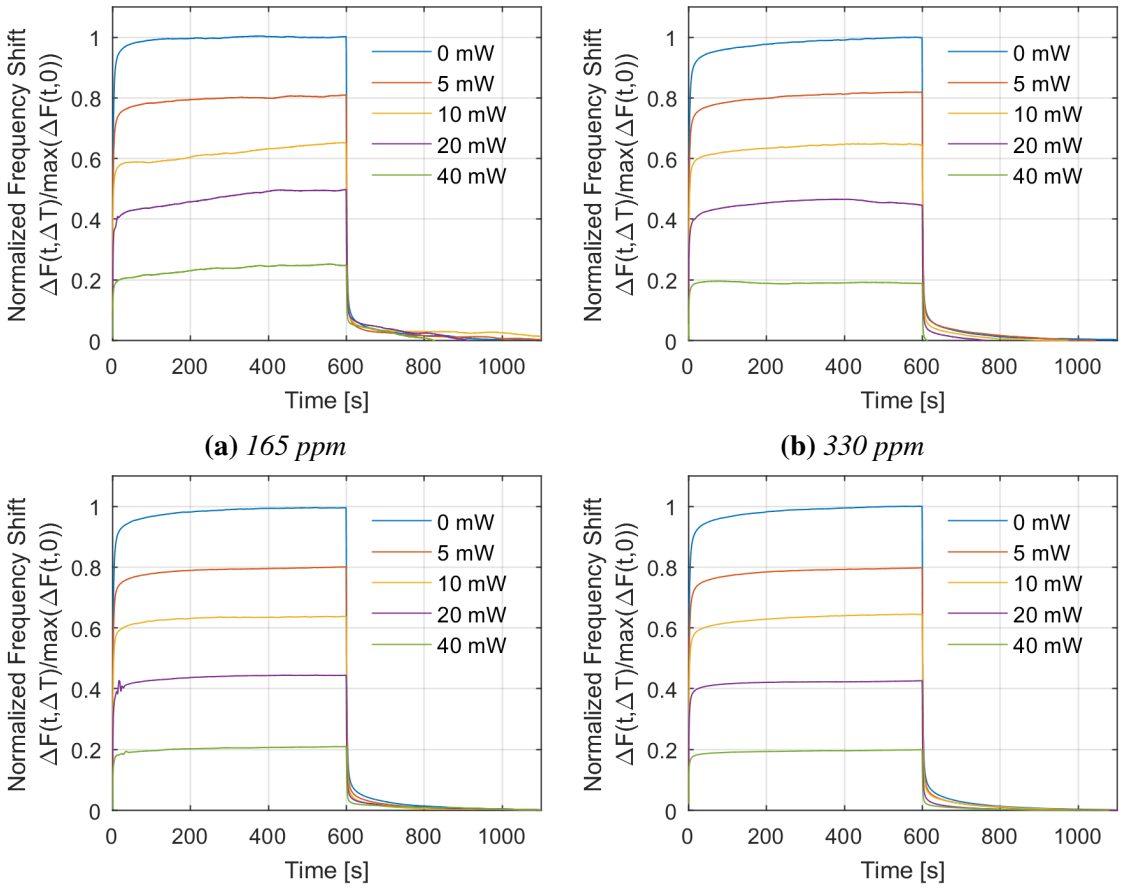

(a) *165 ppm* **(b)** *330 ppm*

(c) *660 ppm* **(d)** *1320 ppm*

Figure 4.12: *Normalized frequency shift, i.e. ratio of frequency shift at a heating power P to the frequency shift at zero heating power, as a function of time while switching from reference gas to analyte-loaded gas ($t = 0\,\mathrm{s}$) and back ($t = 600\,\mathrm{s}$) for four different o-xylene concentrations and four distinct heating powers.*

tinuously powered at a constant heating power, set prior to the measurement start, and the gas mixing system was used to switch between a known analyte concentration and reference gas. Obviously, this alternate method of sensing only works in applications where switching between the reference gas and analyte-loaded gas is feasible. After reaching equilibrium in a reference gas flow at 80 sccm, a high-speed valve switched the gas flow to an analyte-loaded gas flow also at 80 sccm. Thereby, the mixing ratios of an analyte-saturated gas flow with a diluting flow determined the concentrations of this analyte-loaded gas flow. For this test, dilution factors of 1:40, 1:20, 1:10 and 1:5 generated gas flows of 165, 330, 660 and 1320 ppm o-xylene in N_2 respectively. The responses, i.e. the measured frequency changes, were normalized by the frequency shift obtained without applied heating power ($P = 0\,\mathrm{mW}$).

Figure 4.13 overlays all four graphs from Figure 4.12 in a single graph to show the repeatability of this measurement. Clearly, the normalized sensor responses are largely concentration independent in the tested concentration range, with variations largely happening at higher heating powers (resulting in smaller partition coefficients) and small analyte concentrations due to measurement noise. Calculated point-by-point vaporization enthalpies vary by 1 kJ/mol to 2 kJ/mol only, while the fitted vaporization enthalpies for concentra-

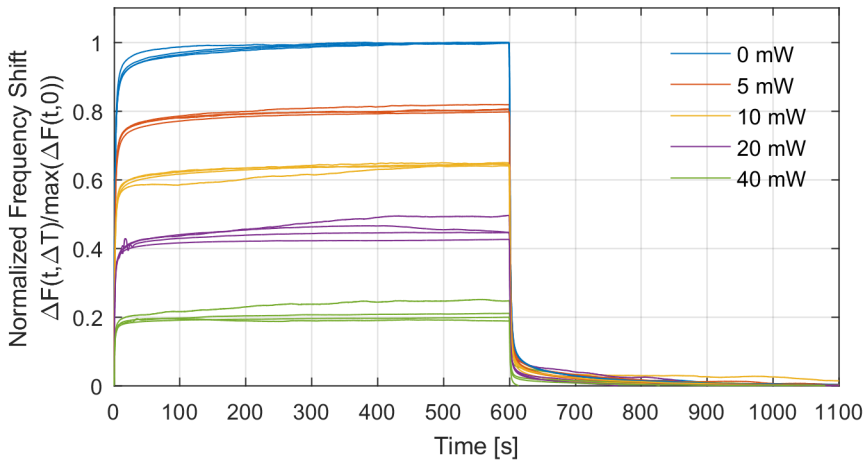

Figure 4.13: *Overlay plot combining all measurements from Figure 4.12 obtained at different concentrations in a single graph. The most significant deviations are evident at higher heating powers* 20 mW *to* 40 mW *and low concentrations.*

tions of 330, 660 and 1320 ppm ranges from 44.6 kJ/mol to 46.5 kJ/mol. These values agree well with previous tests from Table 4.2, where the estimated enthalpy of vaporization for o-xylene in case of the PEUT film was 45.90 kJ/mol. Data collected for 165 ppm appears noisy as the experimental setup has stability issues for lower concentration measurements. Despite this noise, the estimated enthalpy at the lower concentration is 39.4 kJ/mol, still within literature accepted ranges. Challenges of low concentration measurements remain, especially in an uncontrolled environment where interference sources can dominate low concentration measurements.

CHAPTER 5

THERMALLY ENABLED DIFFUSIVITY AND TRANSIENT SIGNAL ANALYSIS

Various methods have been previously explored to increase the selectivity of a chemisorbing sensor via analyzing the transient data. Kummer et al. and Su et al. showed the effectiveness of using a valve generated signal transient to discriminate between similar analytes in chemicapacitor [134] and resonant cantilever (shown in Figure 5.1a) [101], respectively, and Carron et al. replaced the valve with heaters to purge the sensing film of analyte [61]. While the latter method of purging the sensing film utilized heating, the measurement analyzed room-temperature re-absorption, thus mimicking the effects of a valve. While both works explored signal transients, the addition of temperature as an independent variable for chemical sensing on an integrated MEMS platform has not yet been explored. This chapter explores the effectiveness of thermally generated sensor transients towards analyte

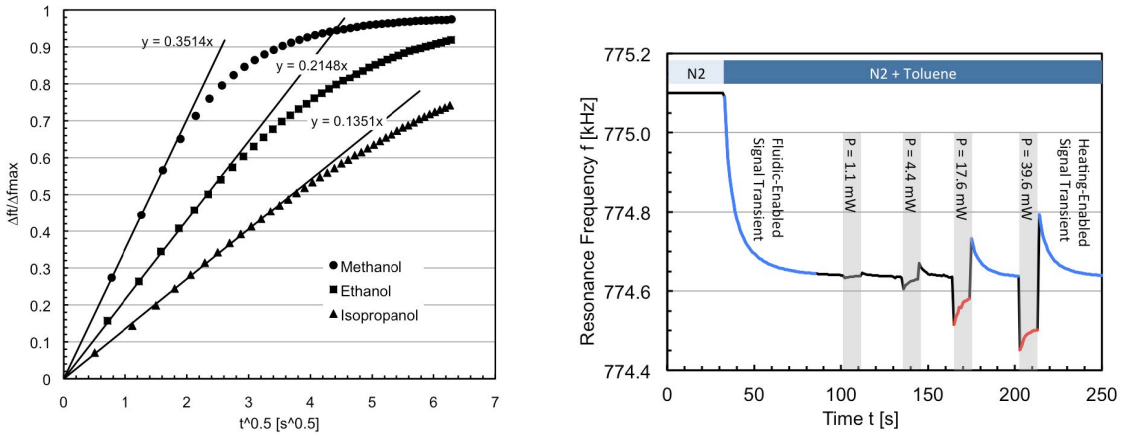

(a) **(b)**

Figure 5.1: *(a) Relative frequency change of a cantilever coated with an absorbing film as a function of the square root of time while switching from reference gas to an analyte-loaded gas stream using a valve-based gas mixing setup. Measured data points are shown as individual markers, while a linear fit through the first 50% of the relative frequency response is plotted as a solid line [101]. (b) Transient signal generation via thermally purging the sensor with a heating pulse. Measured re-absorption transients show this technique is effective at reproducing valve-like transients [61].*

discrimination. Specifically, this chapter investigates differentiating between analytes via Arrhenius diffusivity coefficients. These values are extracted from measured desorption transients at various temperatures.

5.1 Diffusivity Temperature Dependence

From Chapter 2, the diffusivity temperature dependence of an analyte into a polymer sensing film can be approximated as

$$D(T) \approx D_0 \exp\left(\frac{-E}{RT}\right), \tag{5.1}$$

where D(T) is the approximate diffusivity at temperature T in Kelvin, D_0 is the Arrhenius pre-exponential factor relating to the diffusivity as temperature approaches infinity, E is the activation energy for diffusion of analyte molecules into the sensing film and R is the gas constant (8.314 J/(mol K)).

The absorption and desorption diffusivity coefficients can be extracted by a fit to the normalized sensor mass change during analyte absorption and desorption (which is directly proportional to the normalized frequency shift of the resonator),

$$\frac{M(t)}{M_\infty} = \frac{2}{h}\sqrt{\frac{D(T)\cdot t}{\pi}}, \tag{5.2}$$

for $M(t)/M_\infty \leq 0.5$ (as shown in Figure 5.1a) [101]. This fit can be easily accomplished via a MATLAB polynomial fit ($y = mx$) where the $x = \sqrt{t}$ and $D = \left(\frac{m\cdot h}{2}\right)^2 \cdot \pi$.

While these coefficients have been shown to be distinct for a few analytes [101], characterizing the polymer-analyte interaction over temperature to extract both D_0 and E may yield greater discriminatory ability. Fitting the desorption diffusivity values to the Arrhenius curve via a first order polynomial fit ($y = mx + b$) to the equivalent linearized form of

the Arrhenius equation accomplishes this task. In this case, the fit becomes

$$\ln D(T) = \ln D_0 - \frac{E}{R}\left(\frac{1}{T}\right), \tag{5.3}$$

where x is the reciprocal absolute temperature ($x = 1/T$), y is the natural logarithm of the measured diffusivity at temperature T ($y = \ln D(T)$), and the fitting parameters m and b are $m = -\frac{E}{R}$, $b = \ln D_0$.

Transient thermal simulations of the heated hammerhead structure using COMSOL (see Figure 5.2) verify that the sorption film on the hammerhead structure has a 90% thermal rise time of 2.9 ms. As this is significantly faster than observed characteristic diffusion time constants of analytes into the films, which are on the order of seconds to minutes especially for thicker films, the device's thermal transient is not considered in the sorption characteristics. In contrast, it is assumed the analyte sorption happens at a constant temperature T.

To verify that the thermal transients indeed do not impact the observed analyte diffusion, the re-absorption of analytes into the sensing film after the end of the heating pulse

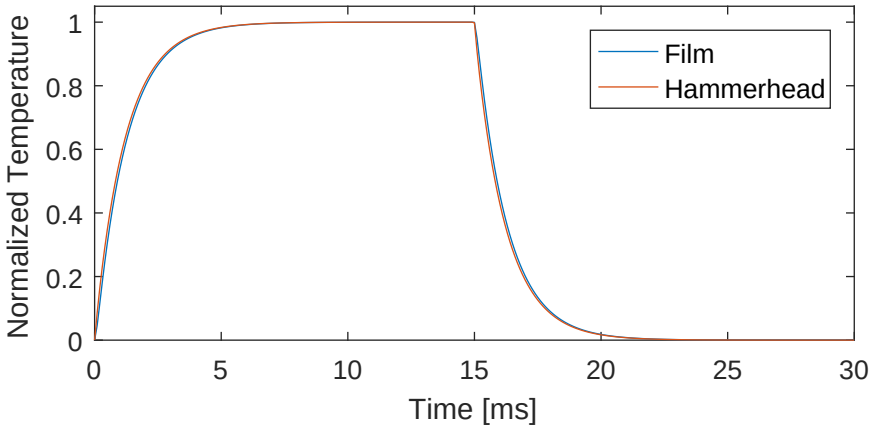

Figure 5.2: *Time-dependent COMSOL simulation of normalized average temperature within the sensing film (blue line) and underlying hammerhead resonator (red line) versus time while applying a* 15 ms *long heating pulse to the resonator. The thermal rise and fall times of the structure with a silicon thickness of* 20 µm *are orders of magnitude faster than diffusivity time constants for a* 6 µm *thick sensing film.*

should follow the same normalized transient behavior independent of the actual heating temperature. Should this not be the case, any effects from the previous heating pulse would increase the measured diffusivity. Figure 5.3 shows diffusion coefficients extracted from re-absorption transients for different analytes into a PIB sensing film as a function of the heating power applied before recording the re-absorption transients. As expected, the extracted diffusivity coefficients are independent of the applied heating power and thus temperature, verifying that re-absorption happens at a constant temperature due to the short thermal time constant of the heated microstructures.

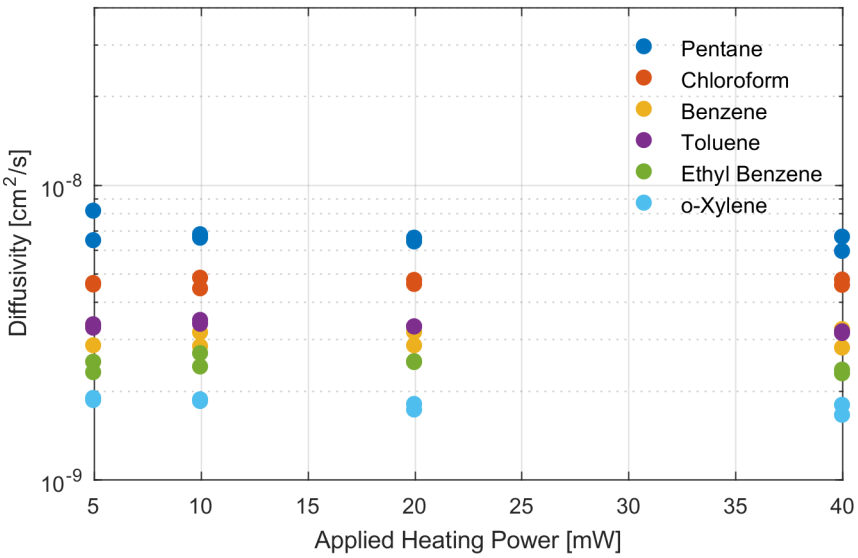

Figure 5.3: *Re-absorption diffusivity coefficients extracted from transients after a heating pulse as a function of the applied heating power for different analytes into a PIB sensing film.*

Data acquired from the chemical measurements described in Section 4.3 for Figure 4.8 using the 6.1 µm thick PIB-coated device was used for the temperature dependent transient analysis. The thick PIB film assures sufficiently long diffusion transients. In the case of the PEUT and OV-1-coated devices tested in Section 4.3, the observed diffusion time constants are on the same time scale as the frequency sampling rates. Thus, extracted diffusion coefficients have large error bars and discriminating between different analytes with these coatings is less feasible. With diffusivity time constants being proportional to the sensing

film thickness squared and sampling rates of the sensor's resonant frequency being fixed at a maximum of 5 Hz to 10 Hz, sensors coated with thin films (approximately 1 µm to 4 µm) are sampled only a few times during transients. Increasing the film thickness or selecting polymers with lower diffusivity coefficients can yield a system that is more suitable for transient measurements. In practical applications, diffusion time constants, τ, should be approximately one order of magnitude longer than the (inverse) sampling frequency for accurate diffusivity analysis. This provides sufficient measurement data points during the transient for curve fitting, reducing the uncertainty in extracted similar diffusivity values. To measure analytes with diffusivity values ranging from 1×10^{-10} cm^2/s to 1×10^{-7} cm^2/s at 5 samples/s and fulfill this practical limitation, requires a film thickness of at least ≈4.5 µm. Increasing the accuracy of the extracted diffusion parameters can be achieved via an increased sampling rate and precision in both timing and measured frequency. However, increasing the sampling rate has a negative effect on the Allan deviation (as the gate time decreases), reducing the precision of recorded measurements and limiting the accuracy of the acquired data.

Figure 5.4a shows the extracted diffusivity coefficients for six analytes as a function of the estimated film temperature. It is important to note that, in this case, desorption transients have been analyzed, i.e. the transients occurring at the beginning of the heating pulse. The measurement points are fitted to an Arrhenius relationship (shown as the solid line in both graphs). The logarithmic form (Figure 5.4b) shows the "linear" relationship highlighted in Equation 5.3 and clearly highlights differences in D_0 (proportional to the y-intercept) and E (proportional to the slope) for the different analytes. It also shows that analytes with similar D_0 may be distinguished by their activation energy E. Acquired data sets are not without fault, some measurements provide obviously erroneous measurements and fits (such as ethyl benzene measured at 45 °C) and further processing with machine learning is required to differentiate these points (Chapter 6) or they need to be excluded as outliers.

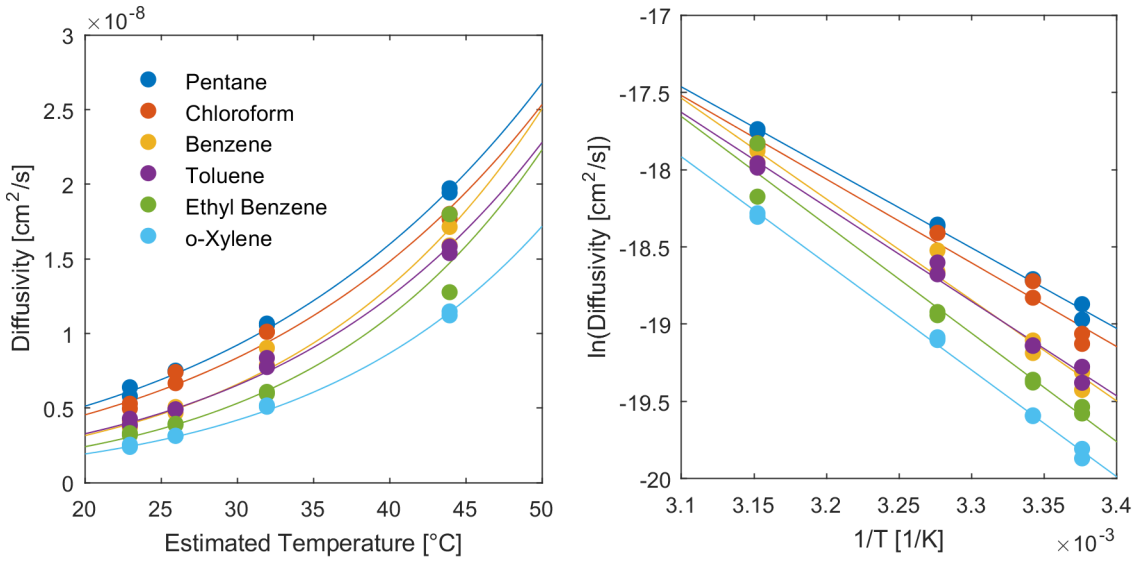

Figure 5.4: *(a) Diffusivity coefficients extracted from analyte desorption transients as a function of the estimated desorption temperature for six analytes for a hammerhead resonator coated with 6.1m of PIB. The solid lines are fits to an Arrhenius relationship; (b) Logarithm of extracted diffusion coefficient as a function of the inverse temperature with "linear" Arrhenius relationship to obtain D_0 and E coefficients from a first order polynomial.*

Table 5.1 displays the extracted pre-exponential factor and activation energy coefficients. Graphically, similar analyte pairs such as benzene and toluene appear to be distinguishable from one another by comparing both coefficients in Table 5.1 as shown in Figure 5.5.

The distinct nature of each analyte's response may allow for identification and separation of closely related compounds even in the case of measurement noise. Optimization of

Table 5.1: *Extracted Arrhenius equation coefficients from data shown in Figure 5.4.*

Analyte	D_0 [cm^2/s]	E [kJ/mol]
Benzene	15.2	54.33
Chloroform	0.484	45.04
Ethyl Benzene	59.9	58.33
Pentane	0.272	43.34
Toluene	3.79	50.86
o-Xylene	32.6	57.39

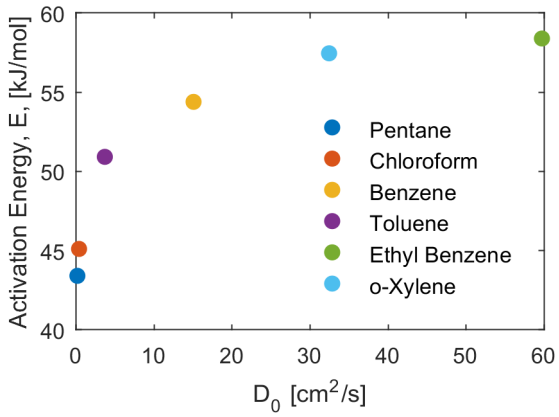

Figure 5.5: *Fitted pre-exponential diffusivity coefficient as a function of the fitted activation energy coefficients for each analyte. The visual separation indicates the possibility to discriminate between different analytes.*

polymer thickness and type can further target specific analytes and lead to an improved selectivity based solely on a diffusion time constant from the transient analysis. This method is complimentary to the partition coefficient investigation from Chapter 4 and a further analysis combining these two methods will be conducted in Chapter 6.

Similar to the steady-state analysis, reliable analysis of transient requires that the diffusivity dependence on temperature must also be concentration independent. To verify

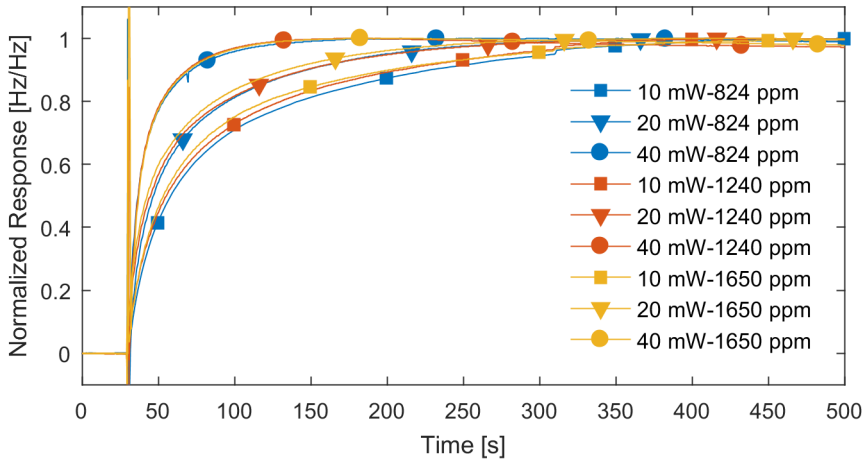

Figure 5.6: *Normalized desorption transients of a heated PIB-coated sensor exposed to (*820 ppm*,* 1240 ppm *and* 1650 ppm*) o-xylene as a function of time for three heating powers (*10 mW*,* 20 mW *and* 40 mW*). Transients depend on temperature (heating power) but not on analyte concentration.*

Table 5.2: *Desorption extracted diffusivity values for three different concentrations of o-xylene and the coefficients from their fit to an Arrhenius relationship.*

	Diffusivity [cm^2/s]		
	10 mW	20 mW	40 mW
820 ppm	3.17×10^{-9}	4.91×10^{-9}	11.1×10^{-9}
1240 ppm	3.23×10^{-9}	3.99×10^{-9}	9.50×10^{-9}
1650 ppm	3.77×10^{-9}	5.19×10^{-9}	12.4×10^{-9}

this, a PIB-coated device was exposed to three concentrations (820 ppm, 1240 ppm and 1650 ppm) of o-xylene and pulsed with three heating pulses (10 mW, 20 mW and 40 mW). Figure 5.6 and Table 5.2 show the result of this test.

With some deviations at the lower heating powers, the sensor transients at different analyte concentrations but the same heating powers follow the same diffusivity curves and trends. Fitting the extracted diffusivity values in Table 5.2 to the Arrhenius relationship yields similar values for E and D_0 as Table 5.1.

5.2 Signal Processing Inspired Analysis

As an analysis technique, heating pulses of varying duration present a unique opportunity to investigate sorption in a sensing film. The transient signal can also be analyzed using Laplace and Fourier transform inspired heating pulses. The Laplace transform of the (normalized) analyte mass diffused into the sensing film in response to a step change in analyte concentration at the film boundary can be calculated from Equation 1.5 as

$$\begin{aligned} \mathcal{L}\left(\frac{M(t)}{M_\infty}\right) &= \mathcal{L}\left(1 - 8\sum_{n=0}^{\infty} \frac{1}{[(2n+1)\pi]^2} e^{-(t/4\tau)[(2n+1)\pi]^2}\right) \\ \frac{M(s)}{M_\infty} &= \frac{1}{s} - 8\sum_{n=0}^{\infty}\left(\frac{1}{[(2n+1)\pi]^2}\right)\left(\frac{1}{s + [(2n+1)\pi]^2/4\tau}\right). \end{aligned} \tag{5.4}$$

Thereby, the change in analyte concentration is the result of either a valve switching or a reduction in the partition coefficient from an increased temperature due to film heating.

Considering the dominant, first term of the Riemann sum only, Equation 5.4 simplifies to

$$\begin{aligned} &\approx \frac{1}{s} - \frac{8}{\pi^2}\left(\frac{1}{s+\pi^2/4\tau}\right) \\ &\approx \frac{(1-8/\pi^2)}{s}\left(\frac{s+\frac{\pi^2}{4\tau(1-8/\pi^2)}}{s+\pi^2/4\tau}\right). \end{aligned} \tag{5.5}$$

This yields an approximate transfer function for the analyte sorption in the form of a single-pole, single-zero system.

$$H(s) = (1-8/\pi^2)\left(\frac{s+\frac{\pi^2}{4\tau(1-8/\pi^2)}}{s+\pi^2/4\tau}\right). \tag{5.6}$$

As expected, the pole and zero locations are real numbers dependent on the characteristic sorption time constant $\tau = h^2/D(T)$, with the pole being located at a frequency 5.28 times greater than the zero. Using this generalized transfer function, the system response to arbitrary changes in the film boundary concentration, either simulated or measured data, can be analyzed using MATLAB (or other software platforms) to determine the pole and zero locations. This analysis also aids in developing effective heating functions that can potentially remove the effects of a specific analyte or aid in discrimination by determining how the analyte will absorb with varying heating frequencies.

The bode plot in Figure 5.7 shows the Fourier analysis (the Laplace transform evaluated at $s = j\omega$) of the normalized added mass in case of o-xylene, toluene and chloroform sorption into a 6.1 μm thick PIB sensing film based on Equation 5.6 and diffusivity coefficients taken from room-temperature measurements in Figure 5.3. This visualization lends itself towards identifying specific frequencies at which the analyte-polymer sorption is unable to occur. Intuitively, for long heating pulses, the system responds with its typical transient behavior with the characteristic diffusion time τ; however, for heating pulses with periods significantly faster than the diffusion time constant, the analyte is unable to fully diffuse back into the film when not heated (i.e. the film temperature is low) or desorb out of the film

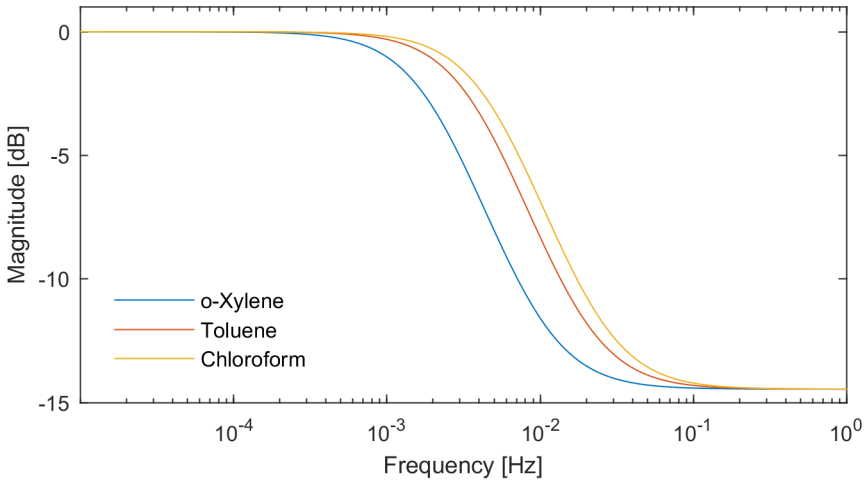

Figure 5.7: *Simulated normalized mass absorption as a function of square-wave heating pulse frequency for o-xylene, toluene and chloroform at room temperature using measured diffusivity values in a* 6.1 µm *thick PIB film.*

during a heating pulse (i.e. the film temperature is high). A −3 dB point characterizes the frequency where half the final mass is unable to diffuse into the film and thus characterizes specific analyte diffusivity within the film.

The simulated −3 dB points are summarized in Table 5.3 show the distinctions between analytes within a 6.1 µm film. As the cutoff frequency is on the order of 1 mHz to 10 mHz (or 100 s to 1000 s), drift due to changing environmental conditions needs to be mitigated via the methods described in Subsection 3.4.2. The cutoff frequencies for a given analyte strongly depend on the sensing film thickness and can be increased significantly by using thinner films.

For analytes with diffusivity values separated by a factor of 5.28 (the pole to zero ratio)

Table 5.3: *Simulated* −3 dB *frequencies of three VOCs in a* 1.00 µm *and* 6.1 µm *PIB film at room temperature.*

Analyte	Diffusivity $[cm^2/sec]$	−3 dB Frequency [mHz] 6.1 µm PIB film	−3 dB Frequency [mHz] 1.00 µm PIB film
Chloroform	4.39×10^{-9}	4.8	178
Toluene	3.43×10^{-9}	3.7	139
o-Xylene	1.80×10^{-9}	2.0	73.2

or greater, a frequency or band of frequencies for heating pulses exists where the analyte with a lower frequency zero will not sufficiently diffuse during that heating pulse, while the analyte with a higher frequency zero will be able to reach equilibrium. Thus, knowing the diffusivity coefficients of analytes in the sensing film can potentially result in generating heating pulse frequencies for specific analyte identification. However, the diffusivity coefficients for analytes studied in this thesis are not separated sufficiently for complete separation based on this method. Nevertheless, the remainder of this chapter will explore how such measurements can provide some information pertaining to the diffusivity.

MATLAB simulations in Figure 5.8 show the normalized mass absorption subject to square heating pulses of varying periods for two diffusivity coefficients based on the approximated transfer function from Equation 5.6. Distinct differences between the envelopes are observed as the pulse frequency increases. Again, these simulated pulses could either come from a valve or be generated by sensing film heating. For a heat generated pulse train to imitate the response of a valve, the heating power would need to be sufficiently high so that the partition coefficients $K_{heating} \ll K_{initial}$. This assures that similar to a valve-based system, the effective concentration outside the film is approaching zero while the film is heated.

Figure 5.9 shows the result of such a measurement for three analytes: chloroform, toluene and o-xylene. While analyzing the data, the chemical and reference measurements

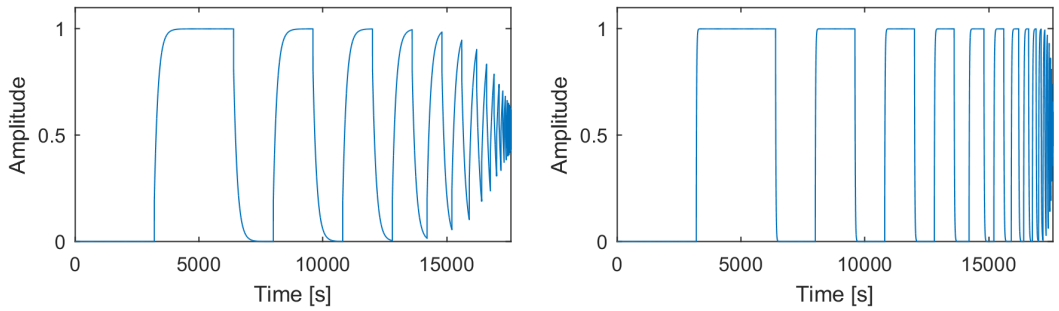

(a) $D = 1 \times 10^{-9}\,\mathrm{cm}^2/\mathrm{s}$ **(b)** $D = 1 \times 10^{-8}\,\mathrm{cm}^2/\mathrm{s}$

Figure 5.8: *Simulated normalized mass change in a* 6.1 µm *PIB film subject to a chain of step excitations with increasing frequency based on transfer function of Equation 5.6.*

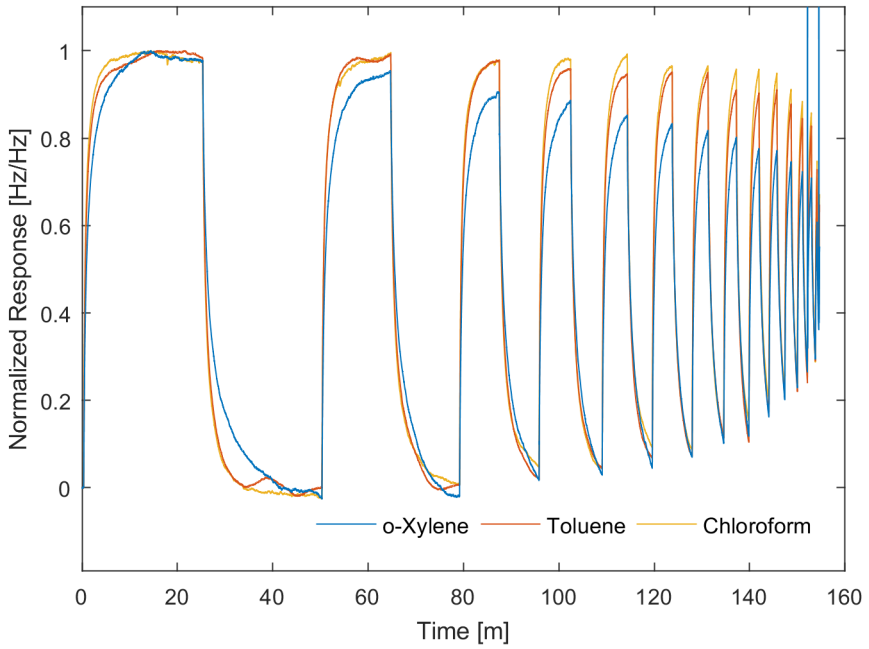

Figure 5.9: *Measured normalized resonant frequency change of a hammerhead resonator coated with a* 6.1 µm *PIB film exposed to three analytes at constant analyte concentration while applying* 10 mW *heating pulses with decreasing pulse length. The measured frequency changes are normalized with respect to the minimum and maximum shifts during the first heating pulse. Heating pulse periods range from* 20 s *to* 3000 s. *Spikes towards the end are from misalignments in the reference and measured data sets during the short heating pulses*

were aligned by cross-correlating the recorded voltage sequence; the index where this value is maximum serves as the reference shift between the two measurements. This alignment method is similar to previous alignments in this thesis, but variations in measurement timing for the shortening pulses can cause sudden spikes in processed data. Whereas in Chapter 4 and Chapter 5, these spikes were ignored, in this instance they along with potential timing variations can cause valuable phase information to be lost. Moreover, heating pulse durations approaching 10 s can become unreliable as LabVIEW timing can fluctuate on the order of 0.5 s to 1 s when communicating with attached function generators and source meters.

Nevertheless, the data shows the absorption-desorption cycle of xylene, subject to the heating pulse sequence, to be distinctly different from toluene or chloroform. This is es-

pecially apparent as the heating pulse period decreases. Figure 5.10 shows the normalized response in decibels as a function of the inverse pulse-duration. The normalizing value is the frequency shift measured for desorption at the longest pulse duration (1500 s). Desorption frequency shifts for the remaining pulses were measured as the frequency differential from the value just prior to the heating pulse to the final value coinciding with the applied voltage termination and peak temperature.

The analyte absorption/desorption as a function of frequency follows the same trend as predicted by Equation 5.6 and Figure 5.8. Differences between the toluene and chloroform responses would likely be noticeable at shorter pulse durations. However, the sampling rate of the measurement equipment limits the length of the shortest pulses that can be accurately aligned and compensated for using existing methods to a few seconds, making these and other closely related analytes not distinguishable from one another using this method. While initial results correlate with simulated values in Table 5.3, additional investigation is necessary to fully develop this technique for increased chemical discriminatory ability.

Heating also allows for partition coefficient changes with a continuous first-derivative, where $K_{heating} \ll K_{initial}$. In this case, the polymer and carrier gas boundary condition,

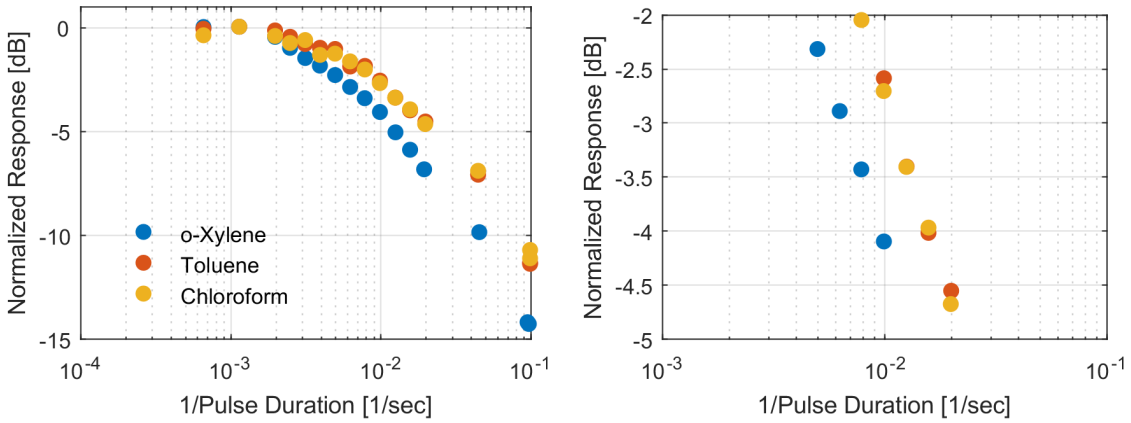

Figure 5.10: *Measured normalized peak-to-peak frequency change as a function of inverse pulse duration using data from Figure 5.9. The* −3 dB *cutoff frequency identifies o-xylene as having the lowest diffusivity coefficient, while toluene and chloroform are essentially indistinguishable using this method.*

$C(r,t,T)|_{r\in\text{film-analyte interface}} = K(r,t,T)\cdot C_A$, from Equation 2.2 is a dynamic system. Modulating the film temperature with a voltage ramp (as opposed to a step function) boundary conditions for Fick's law beyond what a traditional valve-based system is able to accomplish. After conversion to power dissipated in the heating resistor, a voltage ramp becomes a second order polynomial temperature change and changes the input Fourier transform. Figure 5.11 shows the corresponding voltage and power for a simulated heating resistor with 800 Ω resistance.

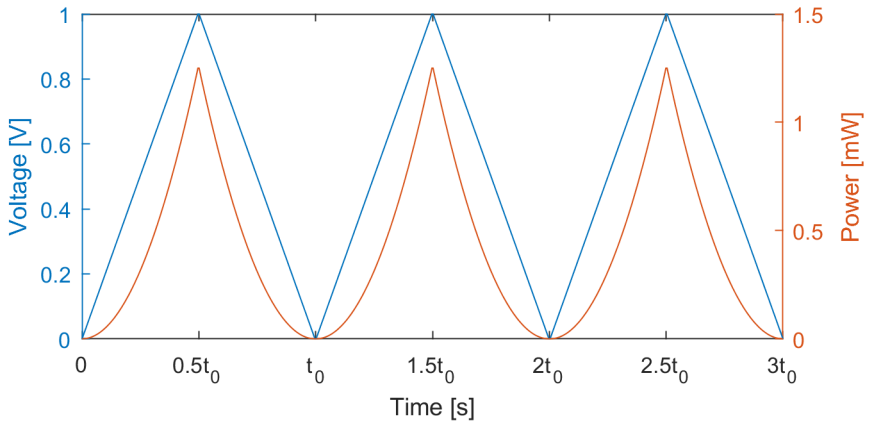

Figure 5.11: *A periodic voltage ramp and corresponding power through an* 800 Ω *resistor.*

Modeling the voltage waveform as the convolution of two periodic rectangular functions (approximated for simplicity to be infinite in length) simplifies a Fourier analysis of the mass-absorption system to this new input.

$$V(t) = \text{rect}(2\cdot t/t_0) * \text{rect}(2\cdot t/t_0) * \sum_{n=-\infty}^{\infty} \delta(t - nt_0). \tag{5.7}$$

This representation simplifies the Fourier transform using the convolution property and known transform pairs. Thus, the voltage Fourier transform becomes

$$V(f) = \frac{t_0}{4}\,\text{sinc}^2\left(\frac{\pi t_0 f}{2}\right)\cdot \sum_{n=-\infty}^{\infty} (f - n/t_0). \tag{5.8}$$

and the power transform follows suit as

$$P(f) = V(f) * V(f)/R \tag{5.9}$$

$$P(f) = \frac{t_0^2}{16}\,\mathrm{sinc}^2\left(\frac{\pi t_0 f}{2}\right) * \mathrm{sinc}^2\left(\frac{\pi t_0 f}{2}\right) \cdot \sum_{n=-\infty}^{\infty} \delta(f - n/t_0). \tag{5.10}$$

Figure 5.12 shows a graphical version for $P(f)$. The two primary frequency components are at DC and the fundamental triangular waveform period. Higher order terms fall off sharply after the triangular waveform period and have negligible effects on the output, thus allowing for interrogating the diffusivity.

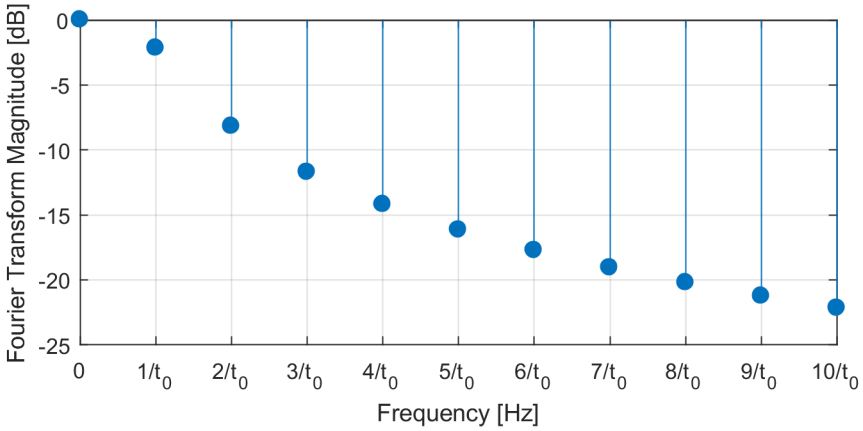

Figure 5.12: *Analytical Fourier transform magnitude for the power applied to the heating resistors with a periodic voltage ramp. As the function is real, it is symmetric about the y-axis and only frequency positive values are shown. As the voltage function is periodic, the Fourier transform is only defined at integer increments of the fundamental frequency,* t_0.

While this input can be used with the previously described transfer function, this analytical model does not incorporate the coupling of temperature to diffusivity. Finite element modeling with physics coupling between the thermodynamic and diffusion models in COMSOL can integrate both the diffusivity and partition coefficient dependence on temperature. Figure 5.13 shows simulated normalized mass absorption into the sensing film incorporating these dependencies, for o-xylene, toluene, and chloroform when a 20 mW

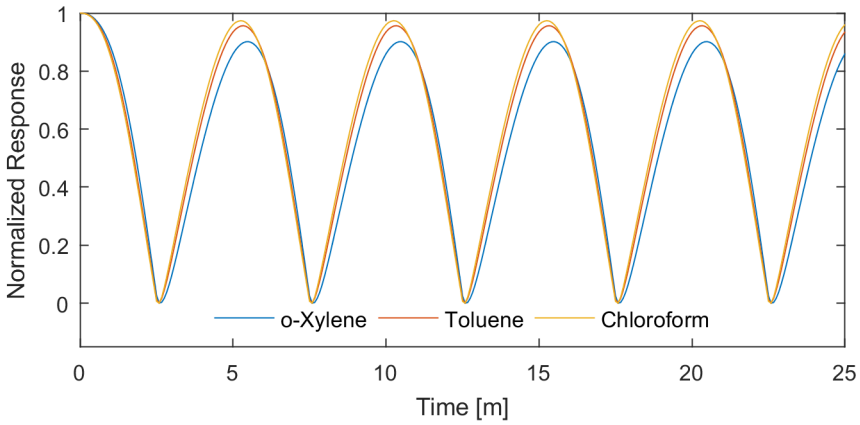

Figure 5.13: *Normalized absorbed analyte mass for o-xylene, toluene and chloroform in a simulated PIB sensing film when a* 20 mW *peak-to-peak heating power is applied from a ramp voltage source. The max value represents the absorbed mass at room temperature, while zero is set to the minimum mass, which occurs near when the partition coefficient is lowest (the maximum temperature).*

peak-to-peak heating power is applied to the simulated resistors from a voltage ramp with a 300 s period. The time-dependent model runs for multiple periods to remove any initial condition bias in the modeling parameters and the inherent step function nature of a time-dependent simulation.

From this simulation, two subtle differences between the three analytes exist. First, the peak-to-peak normalized amplitude decreases for o-xylene compared to toluene and chloroform. Secondly, a subtle phase delay from minimum film temperature is visible in Figure 5.13. Following the diffusivity trends measured and recorded in Table 5.3, for the 300 s pulse period, this delay is approximately 15 s for chloroform, 20 s for toluene, and 30 s in the case of o-xylene.

Intuitively, during the first heating pulse, the increased desorption rate removes more analyte from the sensing film than can reabsorb during the subsequent cool down, causing a peak-to-peak value that is shifted from steady-state values. While the response is normalized, the different peak-to-peak amplitudes between simulated analytes are a result of the differing desorption and re-absorption rates coupled with partition coefficient physics. As chloroform has the lowest enthalpy of vaporization and temperature-diffusivity depen-

dency (E), the peak-to-peak value is expected to be the largest; whereas the peak-to-peak value for o-xylene is the smallest, which corresponds to the highest vaporization enthalpy and largest temperature dependence of diffusivity for the three analytes.

Measurements with three analytes, o-xylene, toluene and chloroform, investigated the feasibility of this heating pulse scheme to identify analytes (Figure 5.14). The sensor was initially exposed to the carrier gas until a stable frequency baseline was reached. A high-speed valve then changed the gas flow to an analyte loaded gas stream. Similar dilution ratios from a gas mixing system generated 300 ppm, 1050 ppm and 8300 ppm of o-xylene, toluene and chloroform, respectively. The steady-state frequency shift from the reference gas to analyte loaded gas sets the frequency shift for normalization, removing any effects of concentration or mass difference between the analyte tests. A voltage ramp sourced by an Agilent 33120A function generator with a period of 300 s and 50% symmetry, provides the heating power to the hammerhead resistors. Ten periods at three different peak voltage levels (corresponding to 10 mW, 20 mW and 40 mW of heating power) provide the thermal changes to the 6.1 µm PIB sensing film. Similar to other measurements in this work, a reference measurement from an identical voltage sequence, recorded while the sensor is in

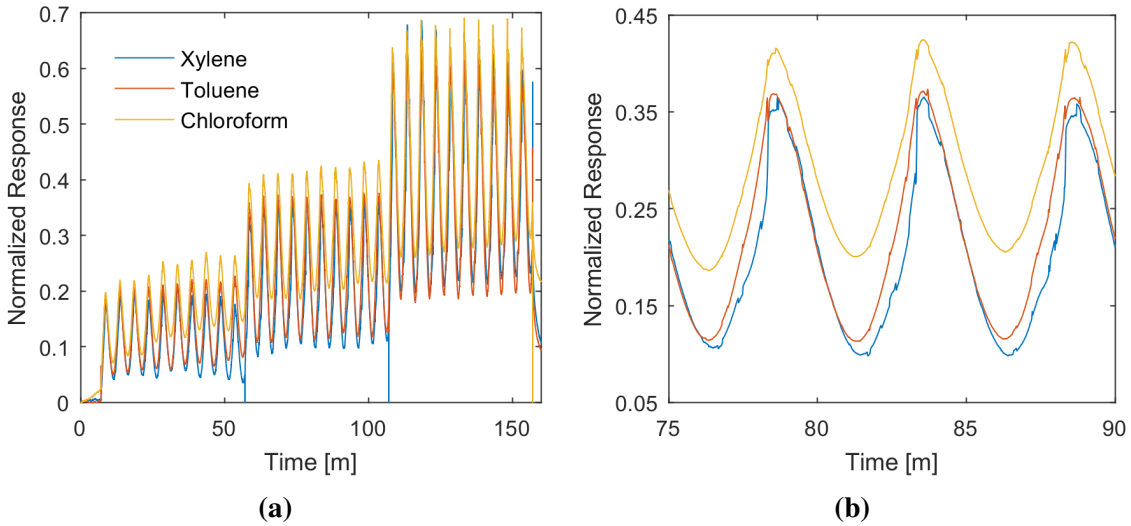

Figure 5.14: *Normalized frequency shift of a PIB-coated sensor to three periodic ramp functions with a peak-to-peak power of* 10 mW, 20 mW *and* 40 mW. *Peak-to-peak frequency shifts and response lag shows the differences between the three analytes.*

a nitrogen environment with the same flow rate as the chemical measurement, provides a compensation frequency shift for the device to remove frequency modulations caused by the temperature dependence of the Young's modulus of silicon.

The measurements show varying peak-to-peak values and DC shifts for the different analytes and heating pulses. The peak-to-peak amplitude variations between the three analytes in Figure 5.14a is most essential to understand how the analyte responds to a periodic signal. However, the peak-to-peak amplitude extracted from the minimum and maximum values in a sliding window do not show significant distinction between the three analytes. True maximum values for each peak is likely obfuscated by sampling rates being insufficient at the inflection point corresponding to the maximum applied power (see Figure 5.11). These values are less distinct than the simulated effects and follow more closely the enthalpy of vaporization, rather than the diffusivity trends from simulation. This is mostly evident in the 20 mW and 40 mW peak heating sequences, where the xylene and toluene data points are very similar, while the chloroform line is distinct, as is the case in vaporization enthalpy measurements. Due to difficulty in reference pulse alignment and a low signal-to-interference-plus-noise ratio (SINR), the 10 mW heating pulse sequence does not provide significant discrimination ability as a peak-to-peak measurement.

Phase information, similar to that observed in the simulations, is more difficult to record as subtle differences in the transient timing are masked by variations between the reference and chemical measurements. While the true peak-to-peak value is difficult to extract due to sampling limitations, the timing of inflection points can be easily identified. Figure 5.14b shows a magnified view of three heating cycles from Figure 5.14a. As expected, the o-xylene leads both the toluene and chloroform measurements during desorption by an average of 11.0 s for toluene and 12 s for chloroform. These data points coincide with earlier measurements in this chapter (Figure 5.9) and simulated data (Figure 5.13) where the respective delays are 10 s and 15 s.

CHAPTER 6
ENVIRONMENTAL ANALYSIS

As highlighted in Chapter 1, a complete environmental analysis is typically done by sampling in the field and using laboratory-based analytical instrumentation, such as gas chromatography in combination with mass spectrometry (GC/MS), for analysis. Chemical sensors, on the other hand, typically detect a particular analyte or a small number of analytes in the field. Dealing with field samples still presents complex challenges to any chemical sensor. Often, compounds of interest are present at low ppm or even ppb levels with many interferents that may be present at higher concentrations. This tests a sensor's limits of detection, selectivity and analytical capabilities. This chapter applies the sensors and methods used throughout this thesis in more complex environments, analyzing multiple parameters hereunto measured to discriminate between analytes.

6.1 Low Concentration Measurements

Low analyte concentrations, approaching the sensor's limit of detection, restrict the methods described in this thesis. The measured frequency shifts, when analyzing both equilibrium and transient signals stemming from the heated sensors, are generally only fractions of the steady-state frequency shifts observed at room temperature, because the partition coefficient decreases with increasing temperature. Moreover, differences between the sensor's response to certain analytes at the heated equilibrium vary by only a few percentile (see Section 4.3). Thus, a more reasonable limit for the smallest analyte concentration needed for proper discrimination needs to be established, as opposed to the theoretical limit of detection for that analyte. As an example, in case of trying to identify toluene based on the heated equilibrium measurement with the PIB-coated sensor, a 1% accuracy threshold would require a 2.11 Hz differentiation (see Figure 4.8e), which is 300 times greater

Table 6.1: *Estimated limit of detection and smallest analyte concentration needed for analyte discrimination for hammerhead resonators coated with different polymers.*

Analyte	6.1 µm PIB		4.1 µm PEUT		0.8 µm OV-1	
	LOD [ppb]	Heated LOD [ppm]	LOD [ppb]	Heated LOD [ppm]	LOD [ppb]	Heated LOD [ppm]
Benzene	1071	107	665.8	66.6	3497	350
Chloroform	952.0	95.2	194.0	19.4	2276	228
Ethyl Benzene	105.8	10.6	62.75	6.3	322.2	32.2
Pentane	2399	240	3666	367	5770	577
Toluene	363.5	36.4	158.4	15.8	843.4	84.3
o-Xylene	66.35	6.6	40.84	4.1	227.2	22.7

than the frequency resolution measured by the Allan deviation. This raises the effective minimum distinguishable limit of detection to approximately 36 ppm. This trend would be similar for the other analytes investigated in this thesis. Table 6.1 shows the extrapolated limits of detection and the estimated minimum analyte concentrations needed for analyte discrimination using the heated analysis. While the analytes are still detectable below this threshold, chemical signatures become less distinct.

For low concentration measurements, a Kin-Tek FlexStream unit provides calibrated ppm levels of analyte to the measurement chamber at a constant flow velocity. A permeation tube filled with an analyte of interest sits inside of the FlexStream unit's oven. Known permeation rates at different temperatures provide controlled analyte concentrations as the mass flow controllers adjust the quantity of mixing gas through the FlexStream system and an internal valve allows for switching between a reference and the analyte-loaded gas.

Figure 6.1 shows the frequency shift of the 6.1 µm PIB-coated hammerhead resonator to toluene at 30 ppm. The observed 1.5 Hz shift yields a sensitivity of 20 ppm/Hz, which matches the ≈18 ppm/Hz extracted from Figure 4.8e (which was obtained using a different measurement setup). Assuming the minimum detectable frequency shift is 7 mHz from Subsection 3.4.2, the extrapolated LOD for toluene detected by this sensor is 420 ppb. However, as measuring the desorption rates or relative equilibrium shifts caused by the heating pulses described in this thesis would require measuring and analyzing fractions of the 1.5 Hz shift, heating pulses that completely (or almost completely) purge the sensing film of analyte and then monitor the transient (similar to [61, 107]) are most likely to

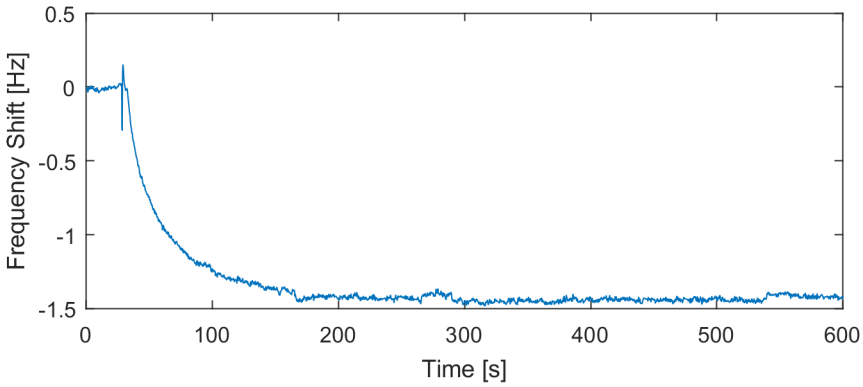

Figure 6.1: *Frequency change of hammerhead resonator coated with* 6.1 µm *of PIB to* 30 ppm *toluene provided by a Kin-Tek FlexStream at* 250 sccm.

be beneficial, since they would yield the largest frequency shifts. The safety limits set by OSHA in Table 1.1, on the order of 10-100 ppm for most VOCs, reflect targets of sensitivity for this system. The detection limits of this device and estimated selectivity limits in Table 6.1 would be sufficient to monitor these safety limits.

6.2 Static Environment

This work investigates two types of static measurement environments: (1) an enclosed chamber with no flow and (2) the analysis of the heated response when the room-temperature frequency shift based on valve switching is unknown.

Figure 6.2 shows the design and build of a measurement chamber designed to simulate no flow conditions. An inlet valve (viewed as the image rightmost port) allows the box atmosphere to be purged through a one-way valve (leftmost port) and a measurement to be reset to known conditions. The middle port contains a septum designed similar to a GC inlet, allowing a microliter syringe inject a liquid or gas sample while keeping the environment sealed. A PTFE gasket seals the sensor chip packaged in a 28-pin DIL package to the chamber's top surface and an acrylic clamp holds the packaged device in place.

After flushing the box with compressed-dry air, the inlet valve closes and, with the one-way valve and septum, seals the chamber. Prior to experiment start, the device reaches a

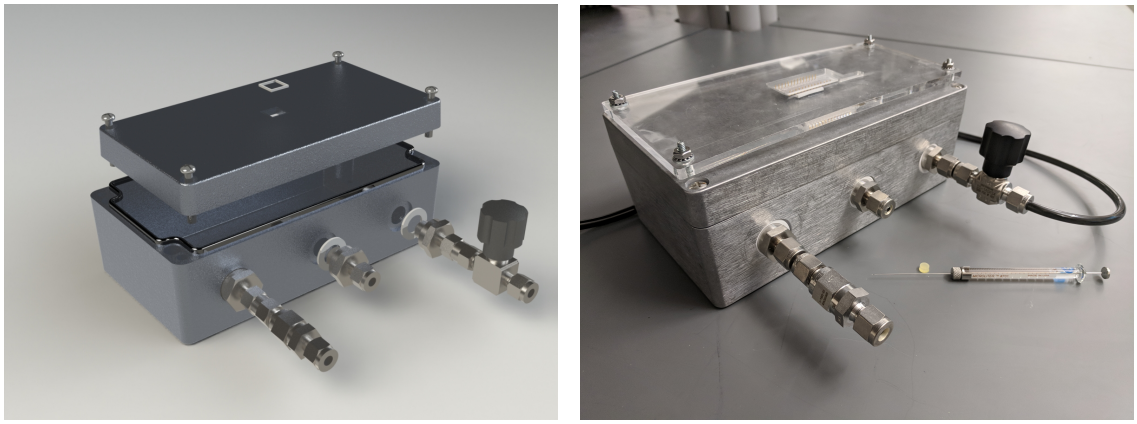

(a) **(b)**

Figure 6.2: *Design (a) and build (b) of a static measurement chamber. The design has an interior volume of* 1.55 L *which allows for* 100 ppm *to* 200 ppm *of analyte concentration per* µL *of injected analyte. The microliter syringe, visible in (b) has a range of* 1 µL *to* 10 µL.

new thermodynamic equilibrium, resulting from the lack of airflow over the sensor. After equilibrium is reached, the microliter syringe injects a 5 µL or 5.75 µL sample of o-xylene or toluene, respectively, through the septa into the measurement chamber. Analyte vaporization and diffusion occurs over the next few minutes (see Figure 6.3). Diluted with the box's environment, these volumes result in chemical concentrations of 730 ppm o-xylene or 740 ppm toluene. Figure 6.3 shows approximately 35 Hz of frequency shift in case of 740 ppm of toluene exposed to the hammerhead resonator coated with 6.1 µm of PIB. The

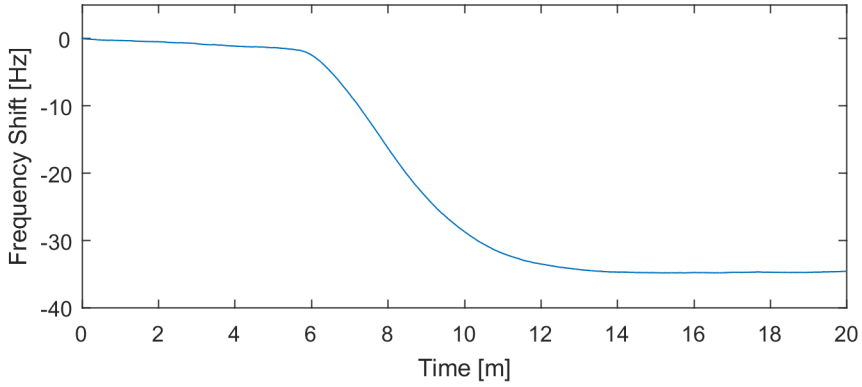

Figure 6.3: *Sensor response to* 5.75 µL *of toluene injected into the* 1.55 L *static chamber at* $t = 0$. *Vaporization and molecular diffusion cause the* ≈6 min *delay in sensor response. The hammerhead resonator tested is coated with a* 6.1 µm *PIB film.*

resulting sensitivity of 21 ppm/Hz is again close to previous results obtained using both the Kin-Tek FlexStream system and the custom gas mixing setup, giving confidence in the different measurement setups.

After stabilization, a Keithley 2400 source-meter applies a heating pulse sequence to the heating resistors. Unlike previous measurements with a continuous source of analyte flowing that maintains a constant concentration in the measurement chamber, diffusion out of the box slowly decreases the analyte concentration in the chamber over time and limits measurement time. Figure 6.4 shows the normalized chemical response to a heating pulse sequence of 5 mW, 10 mW and 20 mW, after environmental and mechanical heating pulse effects were removed in post processing. The responses have been normalized to the maximum frequency shift at 20 mW. Similar to the analysis in Chapter 4 and Chapter 5, the device's response varies with temperature and the transients as well as equilibrium frequency shift can be analyzed similar to Chapter 4 and Chapter 5.

While the transient analysis highlighted in Chapter 5 is based on the knowledge of the heating-induced signal transients, the equilibrium analysis from Chapter 4 requires the

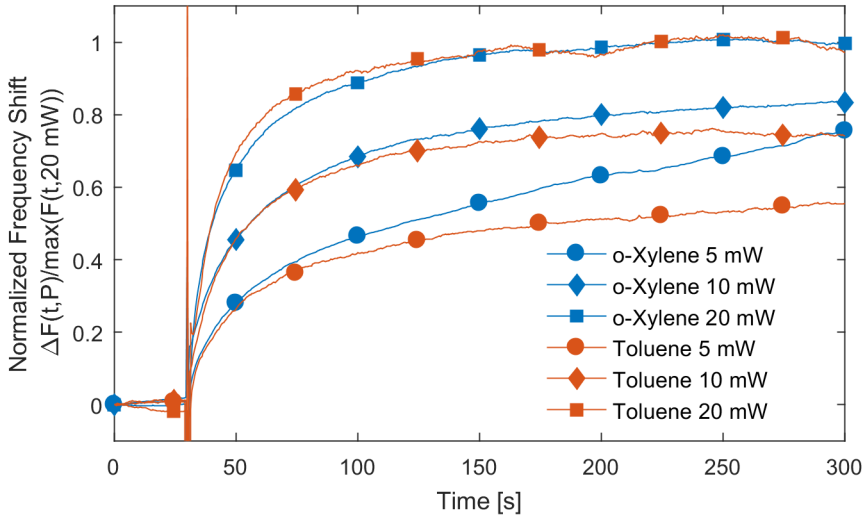

Figure 6.4: *Normalized frequency shift resulting from analyte desorption due to* 5 mW, 10 mW *and* 20 mW *heating pulses for the enclosed chamber in a* 730 ppm *o-xylene or* 740 ppm *toluene environment. The hammerhead sensor used was coated with a* 6.1 µm *PIB film and the measured frequency shifts were normalized by the maximum frequency shift for the* 20 mW *heating pulse.*

knowledge of the resonant frequency without analyte as a reference value for the calculation performed in Equation 4.1. In a laboratory environment, this reference frequency can be easily found by (valve) switching between analyte and reference gas cylinders to extract analyte information. While the reference frequency could be initially measured in the lab and programmed into the system, the unavoidable long-term drift of the resonant sensors would require frequency re-calibration, which again may be difficult to achieve with remote sensors. This poses the question whether one could extract analyte specific information without requiring the knowledge of the reference frequency without analyte? The answer is yes, at least in theory, as will be highlighted in the following.

The mass change in the sensing film is proportional to the analyte mass m_a, the analyte concentration in the environment C_A and the partition coefficient K at temperature T_0

$$\Delta M_0 = m_a C K(T_0), \tag{6.1}$$

with the mass change being proportional to the measured frequency change $\Delta f \propto \Delta M$. When changing the sensing film from $T_0 \rightarrow T_1$ and $T_0 \rightarrow T_2$, the resulting mass change simply becomes

$$\Delta M(T_1) = mC\left(K(T_0) - K(T_1)\right) \text{ and } \Delta M(T_2) = mC\left(K(T_0) - K(T_2)\right). \tag{6.2}$$

If one divides both equations, takes the logarithm on both sides, Equation 6.3 can be derived, which relates the ratio of the mass changes $\Delta M(T_1)/\Delta M(T_2)$ at temperatures T_1 and T_2 to the vaporization enthalpy ΔH_{Vap}:

$$\begin{aligned}
\frac{\Delta M(T_1)}{\Delta M(T_2)} &= \frac{mC\left(K(T_0) - K(T_1)\right)}{mC\left(K(T_0) - K(T_2)\right)} = \frac{K(T_0) - K(T_1)}{K(T_0) - K(T_2)} \\
\log\frac{\Delta M(T_1)}{\Delta M(T_2)} &= \log\left(K(T_0) - K(T_1)\right) - \log\left(K(T_0) - K(T_2)\right) \\
\log\frac{\Delta M(T_1)}{\Delta M(T_2)} &= \log\left(10^{\frac{\Delta H_{Vap}}{2.303\cdot RT_0}} - 10^{\frac{\Delta H_{Vap}}{2.303\cdot RT_1}}\right) - \log\left(10^{\frac{\Delta H_{Vap}}{2.303\cdot RT_0}} - 10^{\frac{\Delta H_{Vap}}{2.303\cdot RT_2}}\right).
\end{aligned} \tag{6.3}$$

Since the mass changes $\Delta M(T_1)$ and $\Delta M(T_2)$ are proportional to the respective frequency changes $\Delta f(T_1)$ and $\Delta f(T_2)$ when heating the sensing film from $T_0 \rightarrow T_1$ and $T_0 \rightarrow T_2$, the vaporization enthalpy can be extracted using Equation 6.3, from the ratio of the measured frequency changes for two heating pulses with different heating powers (at constant analyte concentration), without the need to know the reference frequency without analyte.

Using this analysis procedure the data presented in Chapter 4 was reanalyzed. The 20 mW heating pulse temperature sets T_2 and $\Delta f(T_2)$, while the remaining heating pulse values for 5 mW, 10 mW, 30 mW and 40 mW set T_1 and $\Delta f(T_1)$. In general, because of measurement noise, the larger frequency changes obtained for higher heating powers generate more reliable data points. The results comparing the 20 mW T_2 and 40 mW heating pulse to extract ΔH_{Vap} are summarized in Table 6.2.

As can be seen from Table 6.2, larger discrepancies exist between literature established and measured values using this method. Of the three coated sensors, the OV-1-coated one performs the best with an average error of 12%. The PIB and PEUT-coated devices exhibit a 19% and 16% average error respectively. As vaporization enthalpies for various analytes in this thesis typically varies by less than ten percent, these errors seem to preclude accurate analyte discrimination with this method in its current state. However, more measurements are needed to explore whether the extracted ΔH_{Vap} are repeatable enough so that they could be used for analyte discrimination with the help of a calibration measurement.

6.3 Mixture

In a mixture environment with n analytes, the added mass at equilibrium in the polymer beam can be assumed as the sum of the added masses stemming from the individual analyte:

$$\Delta M(T) = \sum_{i=1}^{n} m_i C_i K_i(T), \tag{6.4}$$

where m_i is the mass, C_i the concentration and $K_i(T)$ is the partition coefficient at a given temperature of the i^{th} analyte. Using Equation 2.7, Equation 6.4 can be rewritten as

$$\Delta m(T) = \sum_{i=1}^{n} m_i C_i 10^{\left(\alpha_i + \frac{\Delta H_i}{2.303 \cdot RT}\right)}. \tag{6.5}$$

Thus, in an environment with multiple unknown analytes and concentrations, the measured stead-state frequency (changes), even when recorded as a function of temperature, is a result of multiple thermodynamic coefficients and there is no straight-forward method to extract analyte relevant information. Likewise, in the presence of multiple analytes, the transient response from Equation 1.5 becomes

$$M(t,T) = \sum_{i=0}^{n} m_i C_i K_i \cdot \left(1 - 8 \sum_{l=0}^{\infty} \frac{1}{[(2l+1)\pi]^2} e^{-(t/4\tau(T))[(2l+1)\pi]^2}\right). \tag{6.6}$$

i.e. the transient response is a linear combination of the analyte-specific transient responses. Figure 6.5 shows the responses of the PIB-coated sensor heated with 5 mW, 10 mW and 20 mW pulses to a single analyte environment of 435 ppm o-xylene (Figure 6.5a) and 2100 ppm of toluene (Figure 6.5b).

Figure 6.6 shows the system response to a mixture of the two gases and the calculated response based on a linear combination of the individual analytes responses. With only

Table 6.2: *Enthalpy of vaporization extracted with an unknown reference frequency without analyte. The ratio of the measured frequency shifts induced by the heating pulses at* 20 mW *and* 40 mW *is used to extract* ΔH_{Vap} *from Equation 6.3. Measured data are taken from Chapter 4, Figures 4.6, 4.7 and 4.8.*

Chemical	Literature [kJ/mol]	PIB[kJ/mol]	PEUT [kJ/mol]	OV-1[kJ/mol]
Benzene	33.9	29.58	25.65	26.00
Chloroform	31.32	33.10	37.10	29.68
Ethyl Benzene	41	39.35	34.08	38.65
Pentane	26.5	45.1	20.43	28.45
Toluene	37	33.35	35.70	31.20
o-Xylene	42	39.6	40.63	37.08

small deviations, the additive response of the individual components equals the frequency shift measured for the mixture. This demonstrates that the responses to individual analytes can be compiled and used as the input for machine learning techniques to extract individual gas components from a heating-induced transient analysis of more complex mixtures.

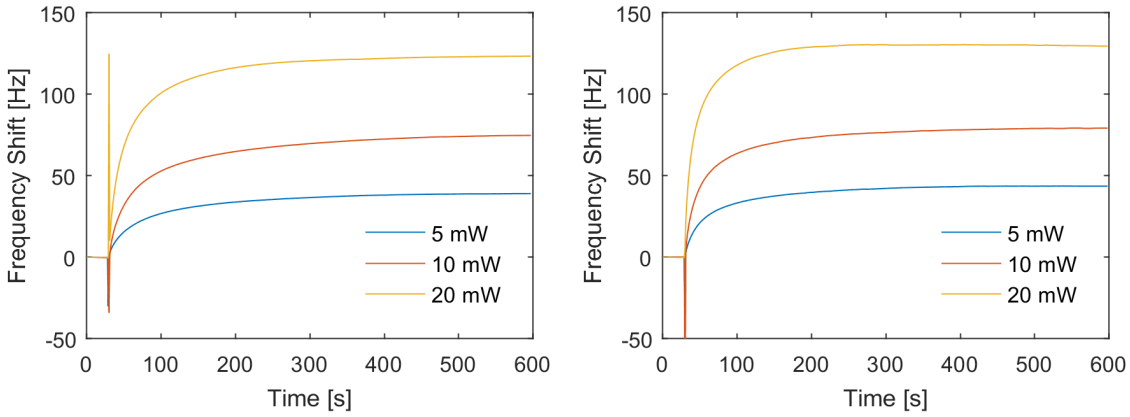

(a) *o-Xylene (*435 ppm*)* **(b)** *Toluene (*2100 ppm*)*

Figure 6.5: *Frequency shift of hammerhead resonator coated with* 6.1 µm *PIB film exposed to constant o-xylene (*435 ppm*) and toluene (*2100 ppm*) concentrations in response to a sequence of heating pulses at* 5 mW, 10 mW *and* 20 mW.

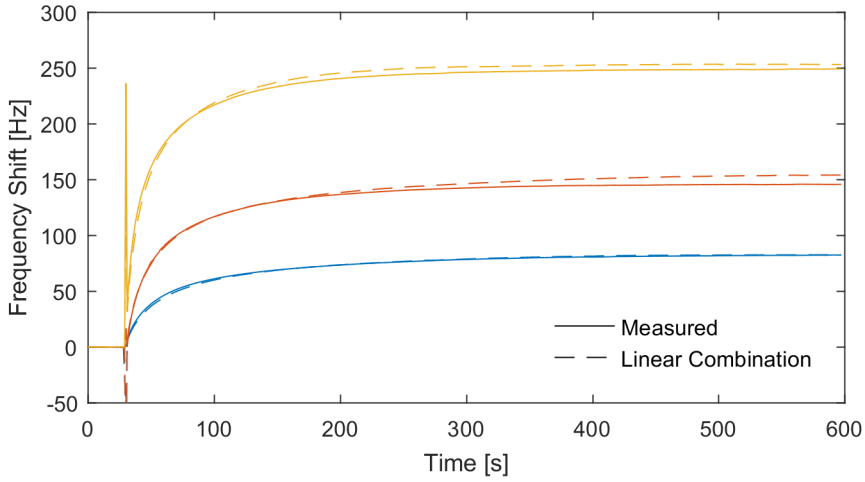

Figure 6.6: *Frequency shift of hammerhead resonator coated with* 6.1 µm *PIB film exposed to a mixture of o-xylene (*435 ppm*) and toluene (*2100 ppm*) concentrations in response to a sequence of heating pulses at* 5 mW, 10 mW *and* 20 mW. *The measured frequency shifts (solid lines) are compared to estimated responses (dashed lines) calculated by a linear combination of the individual analyte responses (see Figure 6.5).*

6.4 Machine Learning

Machine learning is an effective technique to train models for classifying data. The MATLAB classification learner enables supervised learning algorithms to train classifiers and generate predictions (see Figure 6.7) [157].

To demonstrate classification capabilities, enthalpy of vaporization and diffusivity coefficients at each temperature (extracted in Chapter 4 and Chapter 5) are assigned as predictors, while the chemical species is the output. Following the previous chapters' analysis, the input variables are normalized so that there are no effects of concentration; thus, the training effectiveness is not limited to specific concentration ranges.

While not captured simultaneously due to equipment limitations (but acquired under identical conditions), Figure 6.8 shows the equilibrium extracted vaporization enthalpies and estimated classification regions for three polymers and six analytes. While providing

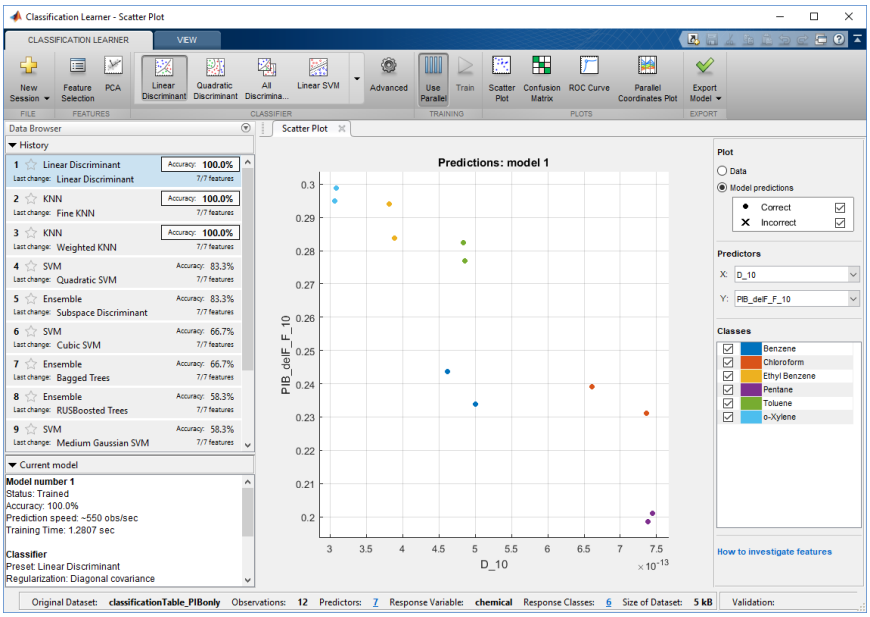

Figure 6.7: *Screenshot from MATLAB's classification learner application. The parameters extracted from measurements in Chapter 4 and Chapter 5 are used as inputs to generate machine learning algorithms to classify the system response to various analytes. Different training models are listed in the leftmost column, with the success of any two predictors (selectable via drop-down options) shown in the middle scatter plot, and the classes listed in the rightmost column.*

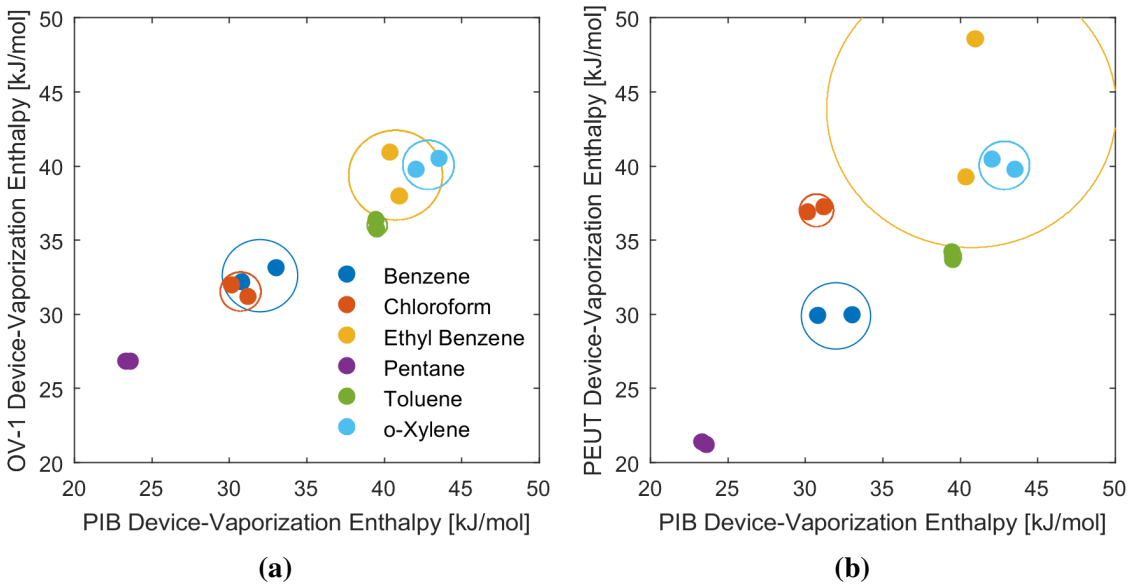

(a) **(b)**

Figure 6.8: *Multi-measurement classification of vaporization enthalpies using PIB, OV-1 and PEUT-coated resonators. The overlapping regions display uncertainty and possible confusion for analyte identification. While the measurements were taken at separate times (due to equipment restrictions), they were recorded with identical input parameters.*

analyte specific classification data, solely relying on the steady-state responses of arrayed devices does not provide full discrimination ability (seen in the overlapping regions in the figures). At best, the supervised learning algorithms only model 83% of the data accurately.

However, using a combination of steady-state and diffusivity measurements for the PIB-coated device, multiple machine learning techniques can classify the six analytes with 100% accuracy. Methods with a perfect success rate for this dataset include linear discriminant, fine K-nearest neighbor, and weighted K-nearest neighbor. Other techniques such as support vector machines and trees show limited success. Additional testing with more datasets would validate this modeling.

Figure 6.9 shows basic partitioning of diffusivity and enthalpy of vaporization measurements for the PIB-coated device. Distinct regions for each analyte are visible in one or more of the plots. As previously discussed, the 40 mW heating pulses strongly reduce the partition coefficient and contribute toward the diffusivity variations between measurements (y-axis). Visually, chloroform and benzene seem to present challenges for discrimination

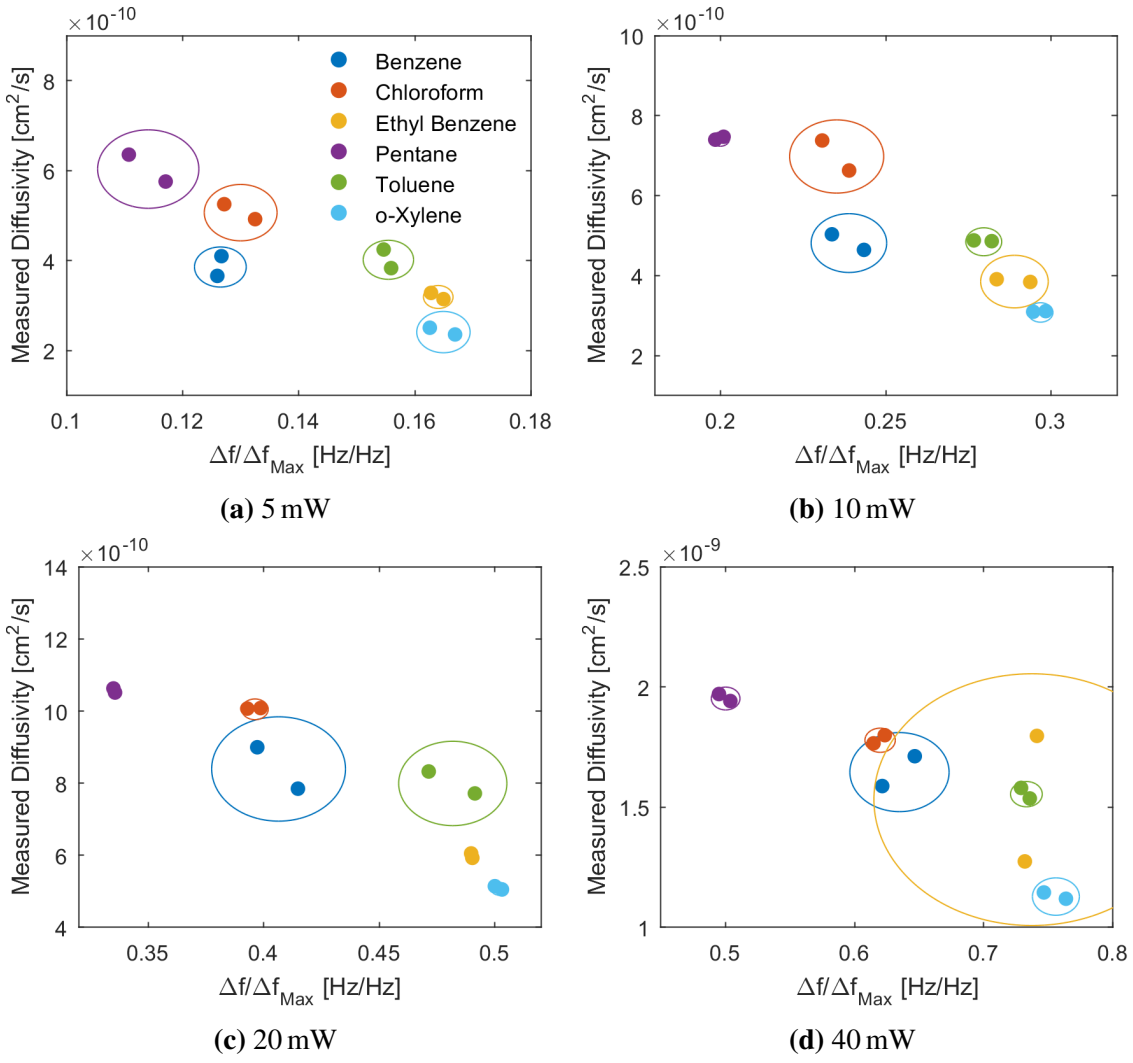

(a) 5 mW **(b)** 10 mW

(c) 20 mW **(d)** 40 mW

Figure 6.9: *Multi-measurement classification of normalized frequency shift and diffusivity values due to different heating powers using a PIB-coated resonator. The overlapping regions of some measurements, do not necessarily repeat on all measurements. This allows machine learning techniques to accurately classify the patterns and discriminate between analytes.*

as their regions partially overlap; however, the supervised learning algorithm is able to separate their distinct signatures (likely due to differences in diffusivity values at 10 mW and 20 mW).

Increased selectivity can be achieved using additional devices coated with different polymers arrayed on-chip. These new measurements would increase the number of classifiers leading to any prediction, enhancing the reliability of any chemical identification.

The coatings on these devices should be substantially thick so that diffusivity coefficient are easily distinguishable at the sampling rate of the frequency counter.

CHAPTER 7
CONCLUSION AND FUTURE WORK

7.1 Summary

The objective of this thesis has been to develop a novel resonant-cantilever-based chemical sensing system to discriminate between similar VOCs. Chapter 2 introduced temperature as an independent variable for sorption into a polymeric sensing film in both steady-state and transient measurements. Pursuant to this investigation, Chapter 3 introduced the design, fabrication and characterization of a heated resonant cantilever designed to modulate the temperature of such polymeric sensing films. Chapter 4 investigated the steady-state sensor response at different temperatures to measure analyte-specific properties. As a complimentary approach, Chapter 5 analyzed the transient response of sorption in the sensing film as a function of temperature. Finally, Chapter 6 introduced the sensor into more complex environments and combined results from the preceding chapters with machine learning techniques to successfully differentiate between analytes.

Pursuant to the above objective, improvements to the mass-sensitive sensing system were presented. A circuit board was designed and built to allow for multiple cantilevers to be operated and resonated simultaneously. LabVIEW code was written to increase the sampling rate of the frequency measurement allowing for more accurate diffusivity measurements, to add additional measurement instruments, and control the heating pulse generation. These improvements allowed implementation of new compensation techniques to reduce the impact of environmental temperature effects on the sensor output, ultimately improving the minimum detectable frequency shift by 26%. Additionally, these improvements enabled the mitigation of undesired resonant frequency shifts from self-heating through reference measurements, thus allowing accurate steady-state and diffusivity measurements.

This novel, systematic approach to discriminating between analytes represents a distinct improvement to prior state-of-the art. It was shown that the enthalpy of vaporization ΔH_{Vap} of an analyte can be estimated through an analysis of steady-state frequency shifts. The thermally generated transients have provided -never before acquired- temperature dependent diffusion rates on a MEMS device. It was also shown that this sensing system and these methods can be used without a reference gas or valve system. The obtained data were assessed with machine learning techniques, providing a novel method for analyte discrimination and improved selectivity through the thermal modulation of a microfabricated cantilever-based chemical sensor.

7.2 Future Work

This work has demonstrated various advantages of a temperature-modulated MEMS-based chemical sensor or sensing system to discriminate between analytes. That being said, there remains a number of topics for future research:

1. **Integrate Temperature Sensors:** An additional resistive element on the hammerhead region, independent of the heating elements, would provide accurate temperature sensing capabilities and remove the need for estimates made in this work.

2. **Mixture Analysis:** One of the most significant drawbacks of MEMS chemical sensors (in the absence of upstream separation techniques), such as chromatography, is specificity in the presence of mixtures. While the techniques discussed in this thesis extract analyte specific values, the analysis and extraction of these constants is complicated in the presence of multiple analytes. While simple mixtures have been initially investigated in Chapter 6, much more work on analyzing mixtures should be done in the future. Besides looking into how signals stemming from mixtures are linear combinations of the individual analyte responses, future work could explore a μGC attached to the heated cantilever system. This would allow for analyte sep-

aration and a mixture analysis. This system could utilize multiple cantilevers in an array with the same thin-polymer, but heated to different temperatures. Thus, allowing for measurements at multiple temperatures (required by the methods presented in this thesis), but allow for the short analyte dwell times in the sensing chamber that is characteristic of chromatography.

3. **Arrayed Devices:** Current recording systems in the iSenSys lab limit the number of cantilevers that can be simultaneously recorded. Future work could expand the measurement system to simultaneously record the resonant frequency of four or more cantilevers. Measurements in this work have already shown successful, simultaneous operation of multiple cantilevers with resonant frequencies separated by only 5 kHz (see Appendix B). However, as adding additional devices would decrease the spacing between resonant frequencies, these measurements would have to account for mechanical and electrical cross-talk between the devices. Additionally, as the vaporization enthalpy measurement is, to a first-order approximation, polymer-independent, an arrayed measurement (while increasing the reliability or redundancy of a vaporization enthalpy measurement) would only provide additional transient information based on analyte-polymer specific properties, such as diffusion rates. These polymer-dependent properties would aid in analyte discrimination and further increase the selectivity of the sensing system.

4. **Expanded Training Sets:** While this work explored in detail three polymers and six analytes, future work could generate a large training dataset as the input for machine learning and analyte discrimination. The addition of multiple resonators coated with different polymers would significantly increase the classification state-space. This would compound the number of analytes that the sensor system could accurately identify and, thus, increase the reliability of any measurement. This system could potentially be used to identify the components in a multi-analyte sample with or

without additional transduction mechanisms or system components.

5. **NEMS cantilevers:** Transitioning from MEMS to NEMS could improve the device performance. Nanometer-scale polymer thickness would allow for shorter absorption time constants and a NEMS device would also require significantly less power to achieve a target temperature. The shorter sorption time constants would also require a shorter heating pulse, further reducing the energy used by the system. However, the resonant frequency still must be sampled at rates sufficient to extract diffusivity coefficients necessary for analyte discrimination, this would require a system to sample the resonant frequency over 1000 samples per second assuming a 600 nm thick PIB film.

6. **Multi-Transducer Integration:** As the techniques described hereunto also apply to other transduction mechanisms, creating a system with the heated resonant mass sensors and other heated sensors (e.g. chemicapacitors) could increase the system's discrimination ability by measuring additional physical properties other than the mass (e.g. dielectric constant) of the analyte.

7. **System Miniaturization:** While, this work presents a compact system that does not require a reference gas or valve system, it is currently limited in size by the surrounding circuitry and printed circuit board. These components could be replaced with an application-specific integrated circuit (ASIC). Further miniaturization in future work would integrate the heated cantilever design onto an IC with post-CMOS processing to form the released cantilever. This would significantly reduce the system volume and power requirements leading to a portable gas sensor.

Appendices

APPENDIX A

FABRICATION PROCEDURE

Below is the fabrication procedure for the heated cantilever devices fabricated in Georgia Institute of Technology's Institute for Electronics and Nanotechnology (IEN) cleanrooms. This process has been developed through multiple graduate students within the iSenSys lab, the most recent significant changes were developed by Christopher Carron. The process flow is included here for completeness.

1. Clean wafer

   - **Tool:** CMOS Cleaning Station and Spin Rinse Dryer
   - **Recipe:**
     (a) Set pirahna bath to 120 °C
     (b) Pour 80 mL into pirahna bath
     (c) Transfer wafers to CMOS boat
     (d) Place boat and wafers into piraha bath for 10 min
     (e) Place waferes in dump rinser for five cycles
     (f) Place wafer in BOE for 30 s with mild agitation
     (g) Place waferes in dump rinser for five cycles
     (h) Dry wafer in CMOS spin rinse dryer
   - **Notes:** The piranha bath should be fresh, this can be tested using a glass dipping rod and a texwipe. A drop from the dipping rod should burn a hole through the texwipe within a couple seconds.

2. Thermal oxidation growth

    - **Tool:** Tystar Nitride Tube 3
    - **Recipe:** wetox.003
        (a) Ensure tool at idle temperature
        (b) Load wetox.003
        (c) *Temperature:* 1050 °C
        (d) *Time:* 3.5 h
    - **Verification:** Nanospec Reflectometer
    - **Notes:** Verify uniformity across wafer, ≈10 800 Å

3. Lithography for diffused resistors

    - **Tool:** Karl Suss MA-6, Spinner, Optical Microscope
    - **Recipe:** Standard lithography steps with Shipley 1827
    - **Mask:** DIFFUSION
    - **Verification:** Optical microscope
    - **Notes:** Alignment to the wafer flat is essential for the piezoresistors. Centering the wafer is desired for maximum device throughput.

4. Thermal oxide etch

    - **Tool:** Plasma Therm ICP
    - **Recipe:** c4f8_lab.bch
    - **Verification:** Nanospec Reflectometer
    - **Notes:** With cleanroom swab and acetone, remove PR from edge of wafer corresponding to clamped area (check tool cleaning wafer). Etch rate ≈1500 Å/min. Over etch for 1 min to 2 min. Oxide thickness should be 0 Å in openings.

5. Photoresist removal

    (a) Remove photoresist with standard acetone, methanol, isopropanol and DI water clean

    (b) Dry wafer with nitrogen gun

6. Wafer clean

    - **Tool:** CMOS Cleaning Station and Spin Rinse Dryer
    - **Recipe:**
        (a) Set pirahna bath to 120 °C
        (b) Pour 80 mL into pirahna bath
        (c) Transfer wafers to CMOS boat
        (d) Place boat and wafers into piraha bath for 10 min
        (e) Place waferes in dump rinser for five cycles
        (f) Place wafer in BOE for 30 s with mild agitation
        (g) Place waferes in dump rinser for five cycles
        (h) Dry wafer in CMOS spin rinse dryer
    - **Notes:** The pirahna bath should be fresh, this can be tested using a glass dipping rod and a texwipe. A drop from the dipping rod should burn a hole through the texwipe within a couple seconds.

7. Boron pre-dep diffusion

    - **Tool:** Tystar Nitride Tube 2
    - **Recipe:** pdopcomm.002
        (a) Ensure tool at idle temperature
        (b) Load pdopcomm.002

(c) *Temperature:* 930 °C

(d) *Time:* 40 min

- **Verification:** Logging computer
- **Notes:** Verify age and conditioning of Boron sources prior to doping.

8. Oxide mask removal

(a) Spin photoresist onto wafer *backside* (to protect thermal oxide)

- **Tool:** Spinner
- **Recipe:** Standard spin on wafer backside
- **Verification:** Visual inspection
- **Notes:** Assure conformal backside coat to prevent oxide removal.

(b) BOE strip oxide

- **Tool:** BOE compatible container and fume-hood
- **Recipe:**

i. Dip wafer, topside up in BOE until oxide is completely removed

ii. Rinse 3x in DI water.

iii. Verify oxide removal with Nanospec Reflectometer

- **Verification:** Nanospec Reflectometer $\approx$0 Å SiO_2 on front-side
- **Notes:** As always with BOE and other acids, PPE is essential. Water should bead off topside surface (hydrophobic) once oxide is removed.

9. Wafer clean

(a) Remove photoresist with standard acetone, methanol, isopropanol and DI water clean

(b) Dry wafer with nitrogen gun

10. Boron drive-in

    - **Tool:** Tystar Nitride Tube 3
    - **Recipe:** lukeox.003 or lukeox.067 (not lukeoxx.067)
        (a) 950 °C wet oxidation for 30 min
        (b) 1000 °C dry oxidation for 30 min
    - **Verification:** Nanospec Reflectometer
    - **Notes:** Verify ≈2000 Å SiO_2

11. PECVD oxide deposition

    - **Tool:** STS PECVD 2 or 3
    - **Recipe:** Standard Oxide-1 µm (can use less)
    - **Verification:** Nanospec Reflectometer
    - **Notes:** Record final oxide thickness.

12. Lithography for contact opening

    - **Tool:** Karl Suss MA-6, Spinner, Optical Microscope, oven
    - **Recipe:** Standard lithography steps with Shipley 1827
    - **Mask:** CONTACT OPENING
    - **Verification:** Optical microscope
    - **Notes:** Critical alignment step, use highest magnification possible on Karl Suss with alignment check. Might need to realign multiple times to assure good alignment. Hard bake in oven at 110 °C for 40 min.

13. Contact opening etch

    - **Tool:** Plasma Therm ICP
    - **Recipe:** c4f8_lab.bch
    - **Verification:** Nanospec Reflectometer
    - **Notes:** With cleanroom swab and acetone, remove PR from edge of wafer corresponding to clamped area (check tool cleaning wafer). Etch rate ≈1500 Å/min. Over etch for 1 min to 2 min. Oxide thickness should be 0 Å in openings.

14. Photoresist removal

    (a) Remove photoresist with standard acetone, methanol, isopropanol and DI water clean

    (b) Dry wafer with nitrogen gun

15. Pre-metalization wafer clean

    - **Tool:** Fumehood and Unifilm Sputterer
    - **Recipe:**

      (a) Create pirahna bath in fumehood according to CR guidelines in standard glass container for single wafer processing

      (b) Place single wafer in piranha bath for 10 min

      (c) Rinse with DI water and dry with N_2 gun

      (d) Dip wafer in BOE for 15 s to strip native oxide from contact openings

      (e) Rinse immediately

      (f) Dry wafer with N_2 gun

      (g) Immediately transfer wafer to load-lock of Unifilm Sputterer and pump down to vacuum

(h) Repeat for other wafers, check max wafer capabilities of Unifilm

- **Notes:** This step should be performed in tandem with the metalization step. The Unifilm Sputterer target should already be pumped down with the correct AlCu target installed.

16. Metal deposition

- **Tool:** Unifilm Sputterer
- **Recipe:** AlCu-450 Å/s, 750 nm
- **Verification:** Visual inspection
- **Notes:** iSenSys lab Al/Cu target should be used for this step, swap out target according to training procedure, when finished store in dry box.

17. Lithography for metalization

- **Tool:** Karl Suss MA-6, Spinner, Optical Microscope
- **Recipe:** Standard lithography steps with Shipley 1813
- **Mask:** METAL
- **Verification:** Optical microscope
- **Notes:** Essential to use 1813. Remove wafer promptly on full development, ≈20 s, to avoid over developing

18. Metal etch

- **Tool:** Plasma Therm ICP
- **Recipe:** SMITAL2E.bch-3 min to 4 min
- **Verification:** Optical microscope
- **Notes:** Important to submerge wafer in DI water after etching for a few minutes to remove trace chlorine and prevent corrosion. BCl_3 etch is not selective and

aggressively etches photoresist. Characterize etch rate with dummy wafer prior to etching SOI wafers. Assure the etch completely removes electrical contact between traces with a resistance check in lab. Aluminum etchant type-A can remove non-visible residual amounts of Al/Cu (dispose in waste container).

19. Clean wafer

    (a) Remove photoresist with standard acetone, methanol, isopropanol and DI water clean

    (b) Dry wafer with nitrogen gun

    (c) Run standard descum

    - **Tool:** Vision RIE or PT-RIE
    - **Recipe:** Descum
    - **Verification:** Optical Microscope
    - **Notes:** Photoresist should be completely removed prior to next steps.

20. Anneal

    - **Tool:** Lindberg Furnace Tube 1
    - **Recipe:**
        (a) *Gas:* Nitrogen
        (b) *Ramp Rate:* 8 °C/min to 350 °C
        (c) *Time:* 15 min
        (d) *Ramp Rate:* 3 °C/min to 450 °C
        (e) *Time:* 150 min
    - **Verification:** None.
    - **Notes:** Place wafer boat in center of tube, where temperature is more stable.

21. Resistance check

    (a) Test structure resistance with iSenSys lab probe station, should be 5 Ω to 10 Ω

    (b) Resistor resistances should be 400 Ω to 1000 Ω (depending on the resistor). Short circuit resistances indicate incomplete metal etching. Can repeat lithography and etch with aluminum etchant type-A.

22. Clean wafer

    (a) Clean with standard acetone, methanol, isopropanol and DI water clean

    (b) Dry wafer with nitrogen gun

    (c) Run standard descum

        - **Tool:** Vision RIE or PT-RIE
        - **Recipe:** Descum
        - **Verification:** Optical Microscope
        - **Notes:** Photoresist should be completely removed prior to next steps.

23. Topside passivation

    - **Tool:** STS PECVD 2 or 3
    - **Recipe:** Standard Oxide (bottom layer, deposited first)-0.5 µm, Standard Nitride (top layer, deposited last)-0.5 µm
    - **Verification:**
    - **Notes:** Deposit half of the oxide or nitride at a time to prevent pinholes. STS sequencer can run all depositions sequentially.

24. Backside passivation

    - **Tool:** STS PECVD 2 or 3
    - **Recipe:** Standard Oxide-2 µm
    - **Verification:**
    - **Notes:** Deposit half of the oxide at a time to prevent pinholes. STS sequencer can run all depositions sequentially. Clean step between wafers according to tool usage rules.

25. Lithography for passivation etch to metal contacts

    - **Tool:** Karl Suss MA-6, Spinner, Optical Microscope
    - **Recipe:** Standard lithography steps with Shipley 1827 or SPR 220
    - **Mask:** PASSIVATION
    - **Verification:** Optical microscope
    - **Notes:** Can hard-bake if necessary (110 °C for 40 min).

26. Passivation etch

    - **Tool:** Plasma Therm ICP
    - **Recipe:** c4f8_lab.bch
    - **Verification:** Nanospec Reflectometer
    - **Notes:** With cleanroom swab and acetone, remove PR from edge of wafer corresponding to clamped area (check tool cleaning wafer). Etch rate ≈1500 Å/min. Over etch for 1 min to 2 min. Oxide thickness on metal contact openings should be ≈0 Å in openings. The fit will not perfectly match as the substrate is aluminum.

27. Clean wafer

    (a) Remove photoresist with standard acetone, methanol, isopropanol and DI water clean

    (b) Dry wafer with nitrogen gun

    (c) Run standard descum

        - **Tool:** Vision RIE or PT-RIE
        - **Recipe:** Descum
        - **Verification:** Optical Microscope
        - **Notes:** Photoresist should be completely removed prior to next steps.

28. Lithography for device definition

    - **Tool:** Karl Suss MA-6, Spinner, Optical Microscope
    - **Recipe:** Standard lithography steps with Shipley 1827 or SPR 220.
    - **Mask:** SI RELEASE
    - **Verification:** Optical microscope
    - **Notes:** Essential hard-bake at 110 °C for 40 min. Do not remove edge of photoresist for the PT-ICP.

29. Hard-bake at 110 °C for 40 min

30. Passivation etch

    - **Tool:** Plasma Therm ICP
    - **Recipe:** c4f8_lab.bch
    - **Verification:** Nanospec Reflectometer
    - **Notes:** Do not remove PR from edge of wafer corresponding to clamped area. Etch rate ≈1500 Å/min. Over etch for 2 min. Oxide thickness should be ≈0 Å in openings.

31. DRIE etch

    - **Tool:** STS ICP, STS ICP HRM, PT-ICP (right)
    - **Recipe:** Bosch process
    - **Verification:** Visual inspection and Tencor P15 Profilometer
    - **Notes:** Etch rates vary by tool and maintenance history. Use a low frequency power supply if available (STS ICP). Depth varies by device layer specifications of SOI wafer.

32. Clean wafer

    (a) Remove photoresist with standard acetone, methanol, isopropanol and DI water clean

    (b) Dry wafer with nitrogen gun

    (c) Run standard descum

        - **Tool:** Vision RIE or PT-RIE
        - **Recipe:** Descum
        - **Verification:** Optical Microscope
        - **Notes:** Photoresist should be completely removed prior to next steps.

33. Backside lithography for device release

    - **Tool:** Karl Suss MA-6, Spinner, Optical Microscope
    - **Recipe:** Standard lithography steps with SPR 220 on wafer backside, with modifications below for backside alignment

        (a) Switch to BSA mode before loading wafer

        (b) Take picture of mask alignment marks before loading the wafer “grab image”

(c) Align

- **Mask:** BACKSIDE
- **Verification:** IR Microscope
- **Notes:** HMDS is essential for backside pillar structures (for a thermal pre-concentrator not used in this work). Alignment check is not necessary as the grabbed image likely shifts if released from the hard contact from a bad alignment. Extra care should be done to assure that the alignment is accurate prior to exposure. Do not move camera beyond boundary of chuck opening. Hard-bake 110 °C for 40 min.

34. Hard-bake at 110 °C for 40 min

35. Backside passivation etch

    - **Tool:** Plasma Therm ICP
    - **Recipe:** c4f8_lab.bch
    - **Verification:** Nanospec Reflectometer
    - **Notes:** Do not remove PR from edge of wafer corresponding to clamped area. Etch rate ≈1500 Å/min. Over etch for 3 min. Oxide thickness should be ≈0 Å in openings.

36. Protect wafer with photoresist

    - Spin SPR 220 or Shipley 1827 onto wafer frontside and backside
    - Protects wafer during dicing

37. Partial Kit-Kat Dicing

    - **Tool:** Dicing Saw
    - **Recipe:** Standard 4-inch recipe with nickel blade, cut depth 9 mil

- **Verification:** Visual Inspection
- **Notes:** The cut depth should be deep enough to allow for manual cleavage, but still allow the wafer to be handled and processed whole.

38. Clean wafer

    (a) Soak wafer in acetone for 30 min, dicing tape side up (tape will float to surface, remove with tweezers)

    (b) Rinse wafer gently with isopropanol then DI water

    (c) Air dry

    (d) Run standard descum on both sides

        - **Tool:** Vision RIE or PT-RIE
        - **Recipe:** Descum
        - **Verification:** Optical Microscope
        - **Notes:** Photoresist should be completely removed prior to next steps.

39. Backside DRIE etch

    - **Tool:** STS ICP, STS ICP HRM, PT-ICP (right)
    - **Recipe:** Bosch process
    - **Verification:** Visual Inspection and Optical Microscope
    - **Notes:** Use cool grease or another thermal paste (such as a low-melting point crystal bond paste) that dissolves in solvent to mount wafer (front-side down) to a carrier wafer. Cool grease does not dissolve and is difficult to remove, contact IEN staff. Etch rates vary by tool and maintenance history. Use standard high frequency power. Etch depth varies by handle layer specifications of SOI wafer. DRIE will stop at buried oxide layer, will be able to see through transparent BOX layer.

40. Backside buried oxide etch and device release

    - **Tool:** Plasma Therm ICP
    - **Recipe:** c4f8_lab.bch
    - **Verification:** Visual Inspection and Optical Microscope
    - **Notes:** Etch rate ≈1500 Å/min, thickness defined by wafer BOX thickness. Over etch for 2 min. Make sure edges are clean, not jagged and cracked.

41. Clean wafer

    (a) Separate device wafer from carrier wafer

    (b) Soak wafer in acetone for 30 min

    (c) Rinse wafer gently with isopropanol then DI water

    (d) Dry with nitrogen gun

    (e) Run standard descum on both front-side, if needed

        - **Tool:** Vision RIE or PT-RIE
        - **Recipe:** Descum
        - **Verification:** Optical Microscope
        - **Notes:** Photoresist should be completely removed prior to next steps.

The standard lithography steps used for this process are as follows. This can be performed on any spinner and Karl Suss mask aligner in the Georgia Tech cleanrooms, provided the recipe can be followed.

1. Set oven to 110 °C
2. Remove photoresist from storage location and wait until at room temperature (if removing from refrigeration)
3. Check spinner chuck and vacuum pressure

4. Enter recipe parameters

    - *Speed:* 3500 rpm
    - *Ramp Rate:* 3 s
    - *Time:* 40 s

5. Apply adhesion promoter (HMDS) with same recipe as photoresist for simplicity if needed for features

6. Apply photoresist and start spin

7. Soft bake at 110 °C for ≈100 s

8. Test and record intensity of CI2 on Karl Suss aligner and set exposure times according to dose

    - **Shipley 1813:** 180 mJ/cm^2. Expected thickness 1.5 µm
    - **Shipley 1827:** 230 mJ/cm^2. Expected thickness 2.5 µm
    - **SPR 220:** 530 mJ/cm^2. Expected thickness 5.5 µm

9. Set parameters for a *Hard Contact* alignment with a 20 µm alignment gap

10. Check alignment prior to exposure, release alignment check if alignment accuracy is not acceptable

11. Expose

12. Check datasheet or notes for any delays prior to development. SPR 220 performs best with a 10 min to 30 min delay before developing.

13. Rinse out development tub with DI water

14. Develop with MF-319 for ≈45 s or until development is complete.

15. Rinse low pressure stream of DI water immediately to stop over-development

16. Inspect with optical microscope to verify development and alignment,

    - Bad alignment or overdeveloped: remove remaining photoresist with acetone, methanol and isopropanol clean to start over
    - Incomplete development: redevelop with fresh developer until completely developed

APPENDIX B

OPEN LOOP TRANSFER CHARACTERISTICS

This appendix contains the open loop transfer characteristics for the devices used in this thesis. The left figure shows the open loop amplitude transfer characteristics of the device over a large frequency range 100 kHz to 1000 kHz. Clearly visible are the first out-of-plane and first in-plane modes at ≈390 kHz and ≈750 kHz, respectively. The right figure shows a higher resolution frequency sweep around the first in-plane mode's resonant frequency with added phase information. Figures of coated devices' transfer characteristics display both the original, uncoated transfer function (dashed line) and post-coating (solid line) sweeps.

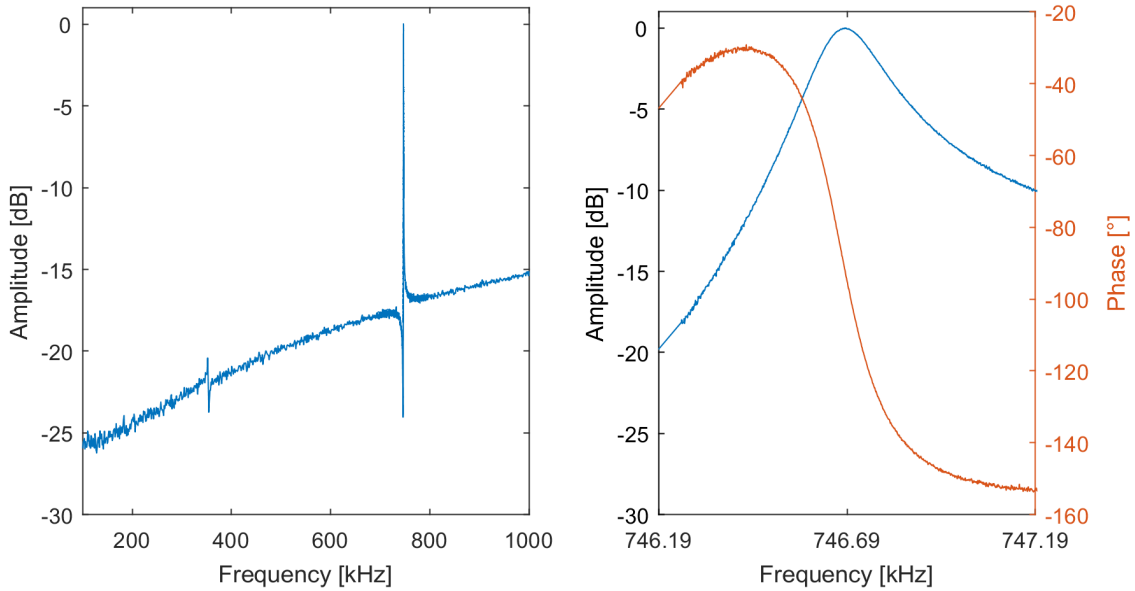

(a) **(b)**

Figure B.1: *Die number 032, uncoated reference device for Figure B.3 and Figure B.2.*

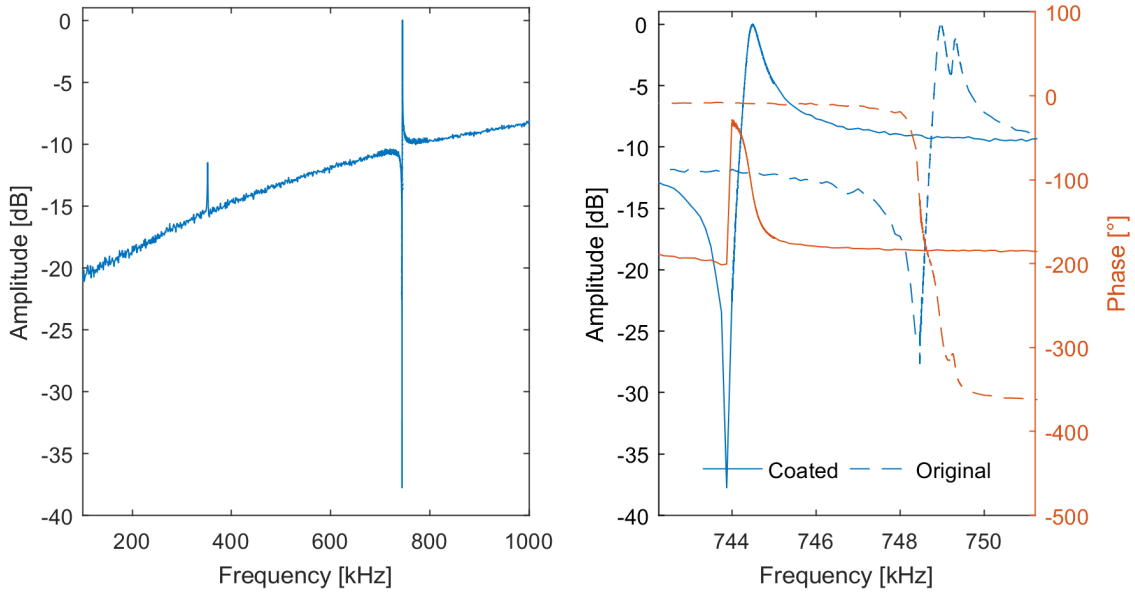

Figure B.2: *Die number 032, sensing device coated with OV-1. The measured resonant frequency shift is* 4.48 kHz*, corresponding to an added mass of* 29 ng *from Figure 3.7c.*

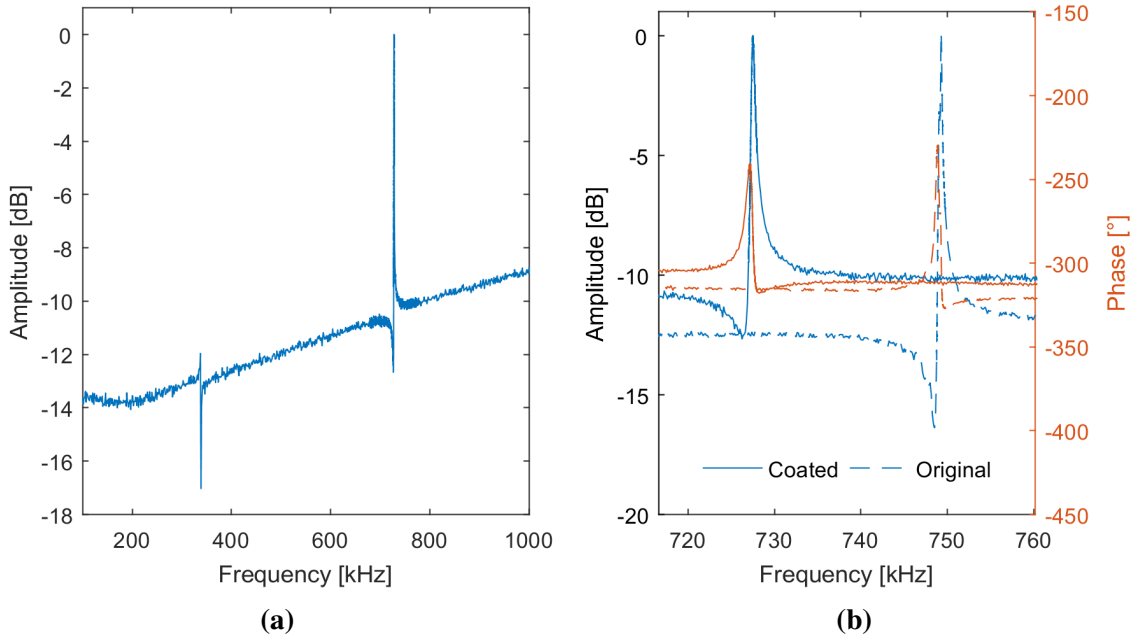

Figure B.3: *Die number 032, sensing device coated with PEUT. The measured resonant frequency shift is* 21.8 kHz*, corresponding to an added mass of* 147 ng *from Figure 3.7c.*

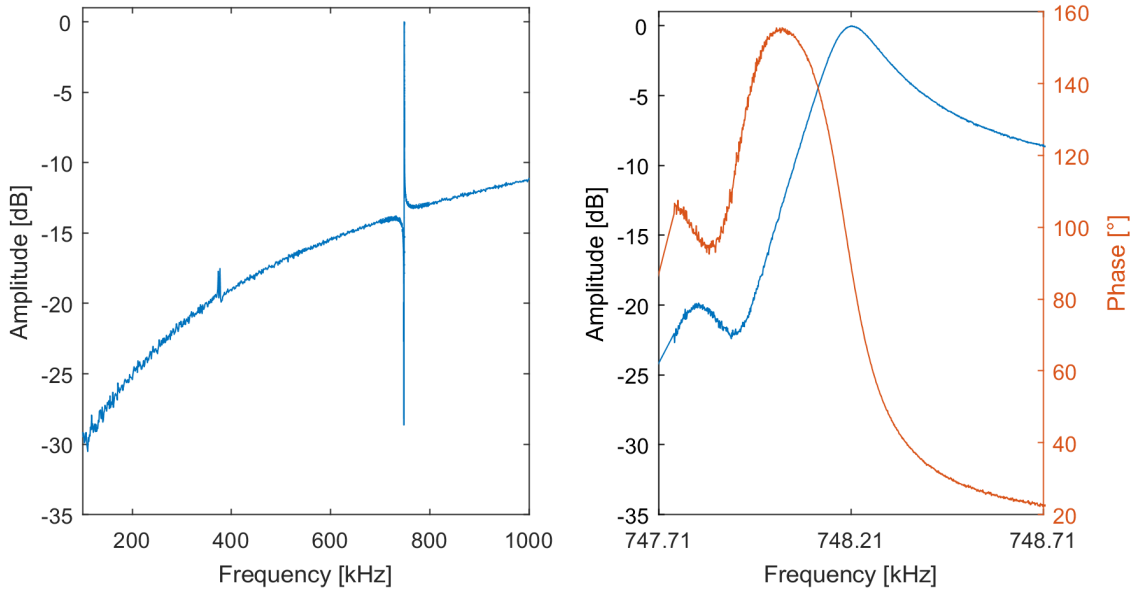

Figure B.4: *Die number 037, uncoated reference device for Figure B.5.*

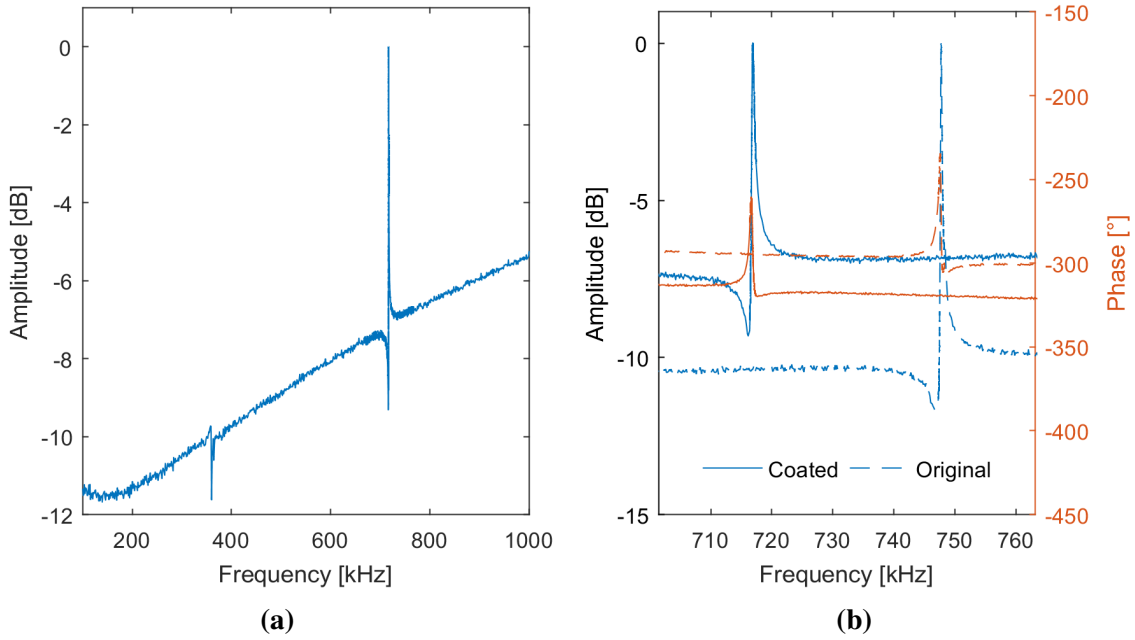

Figure B.5: *Die number 037, sensing device coated with PIB. The measured resonant frequency shift is* 30.8 kHz*, corresponding to an added mass of* 213 ng *from Figure 3.7c.*

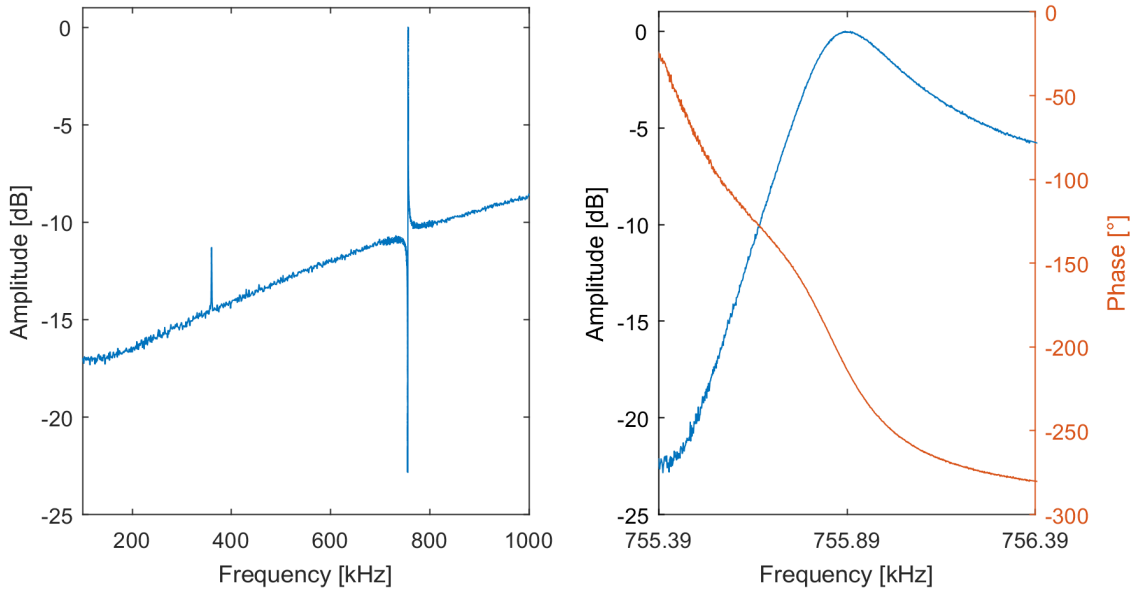

Figure B.6: *Die number 044, uncoated reference device for Figure B.7.*

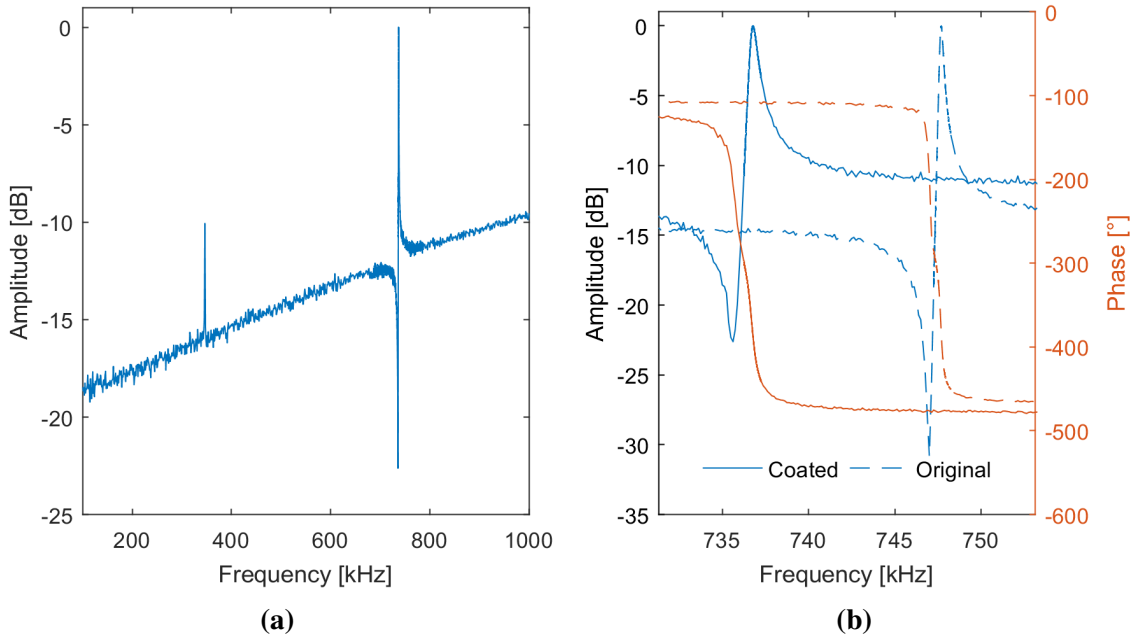

Figure B.7: *Die number 044, sensing device coated with OV-1. The measured resonant frequency shift is* 10.9 kHz*, corresponding to an added mass of* 72 ng *from Figure 3.7c.*

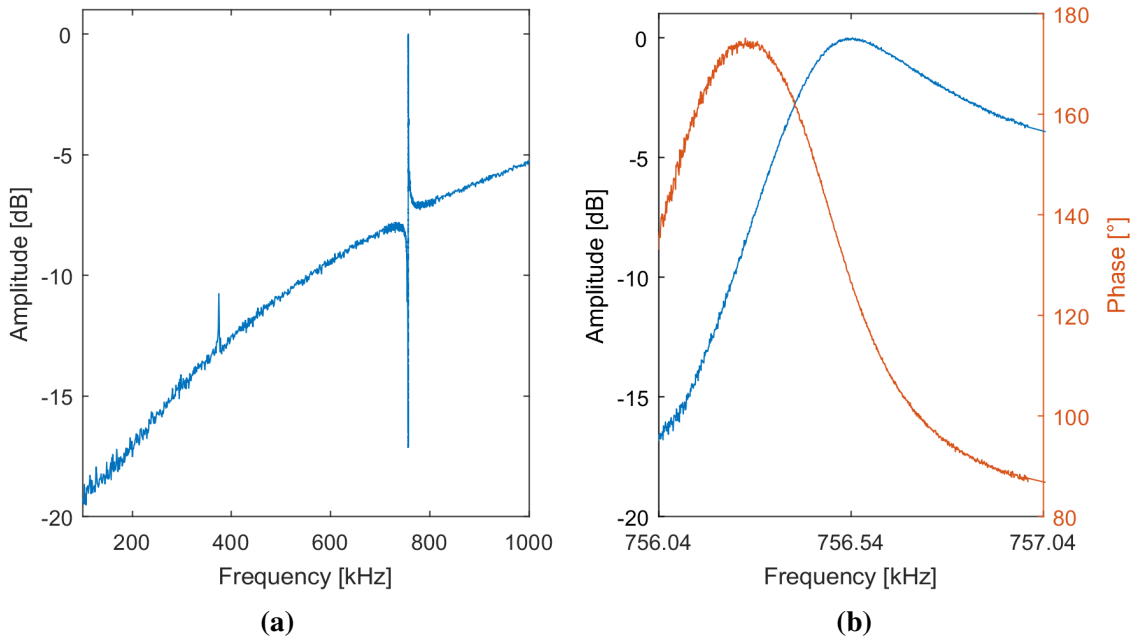

Figure B.8: *Die number 046, uncoated reference device for Figure B.9*

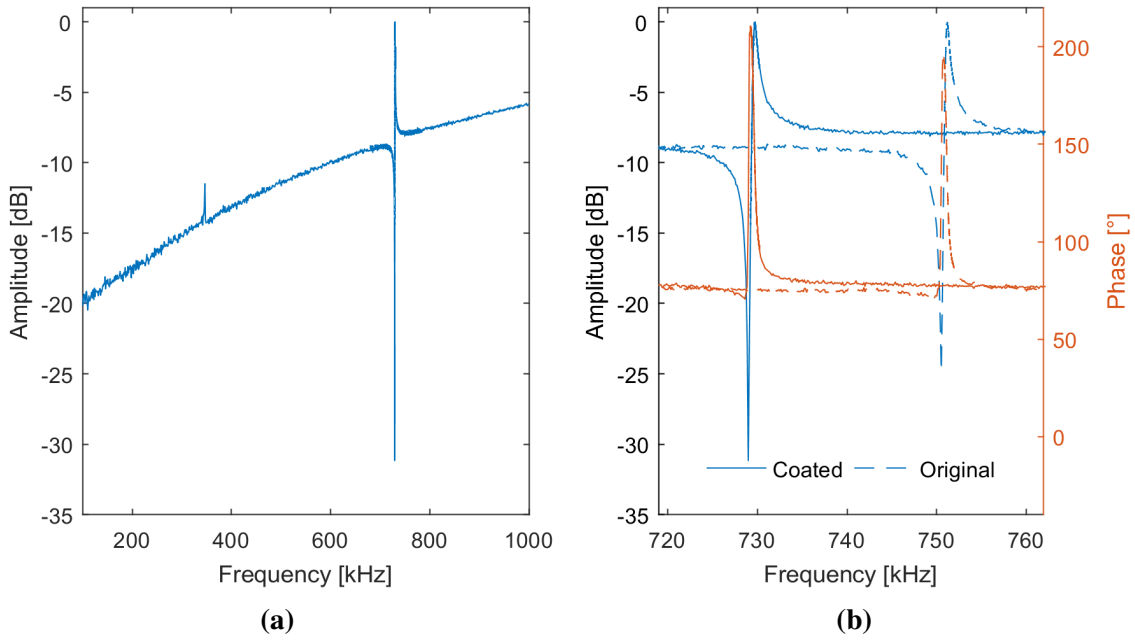

Figure B.9: *Die number 046, sensing device coated with PIB. The measured resonant frequency shift is* 21.4 kHz*, corresponding to an added mass of* 144 ng *from Figure 3.7c.*

APPENDIX C

PCB AMPLIFYING FEEDBACK LOOP

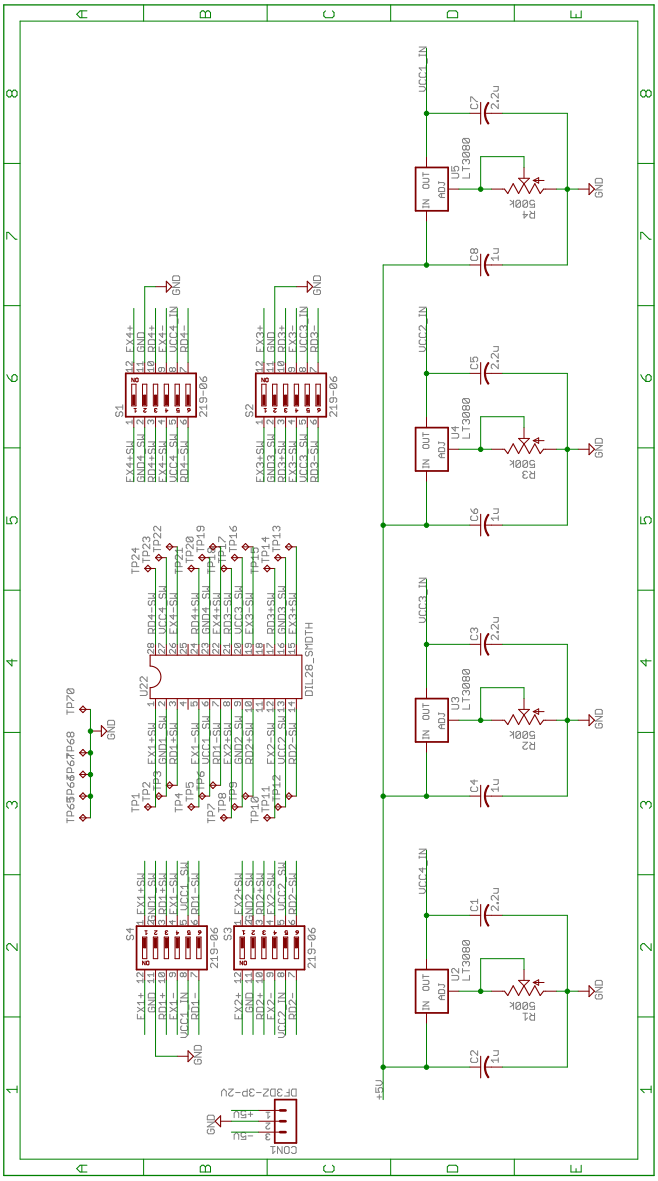

Figure C.1: *Schematic of closed-loop resonant PCB-page 1.*

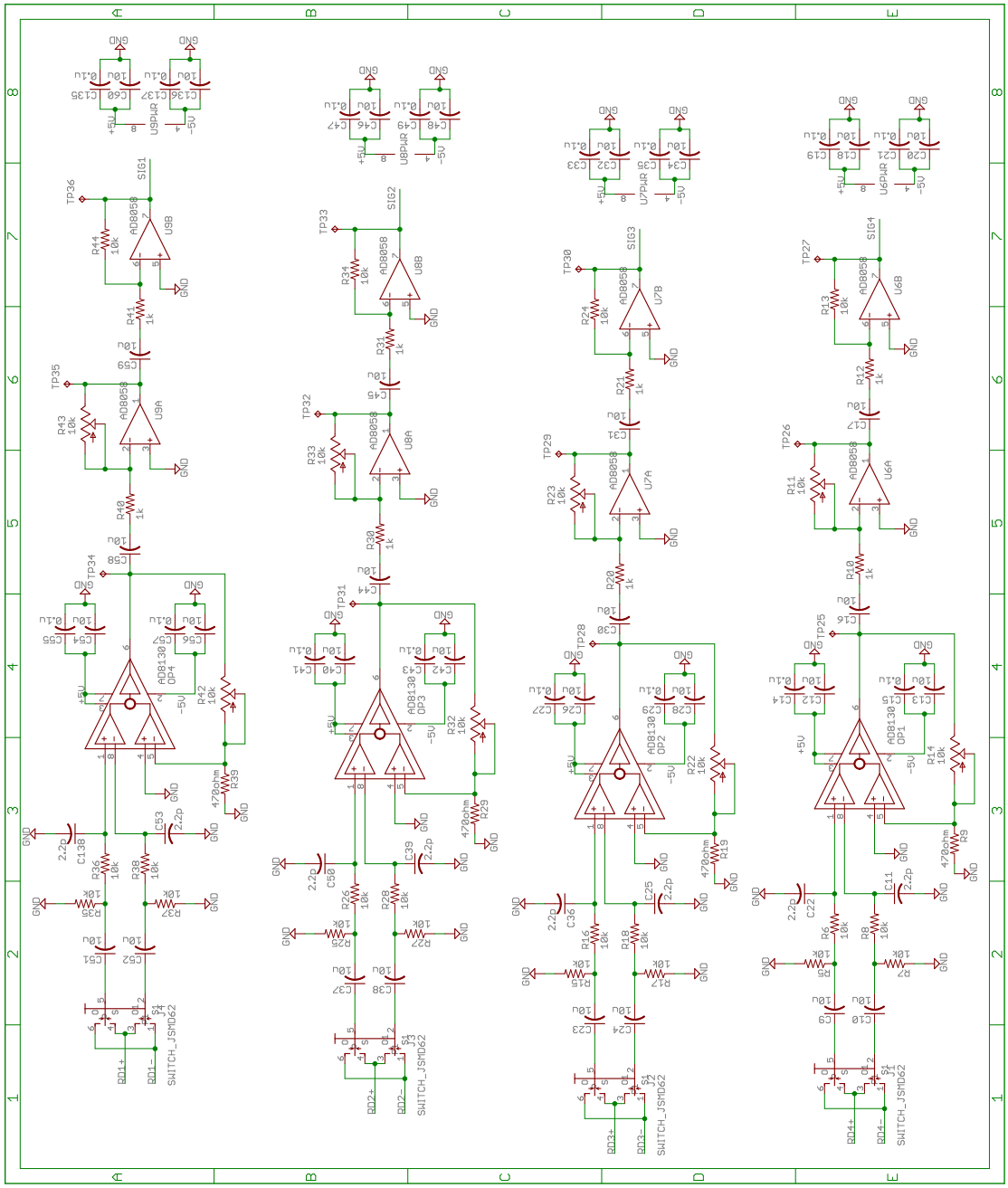

Figure C.2: *Schematic of closed-loop resonant PCB-page 2.*

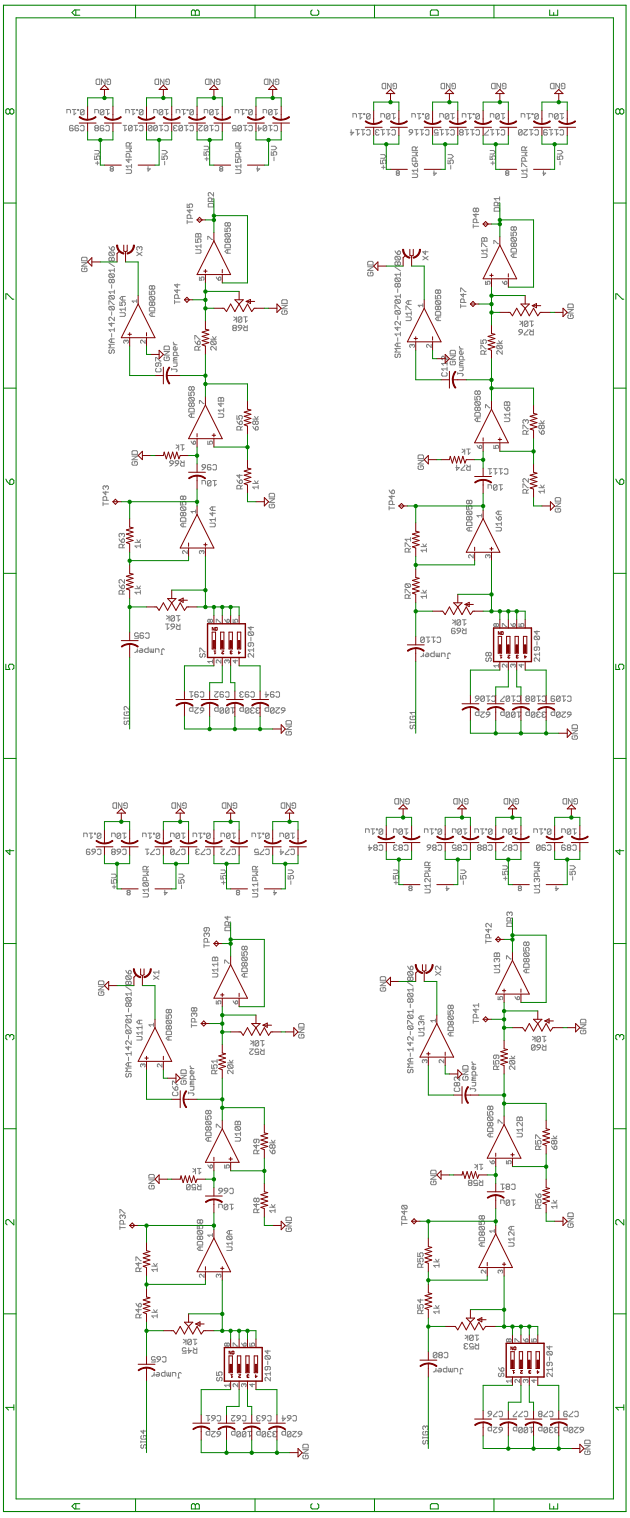

Figure C.3: *Schematic of closed-loop resonant PCB-page 3.*

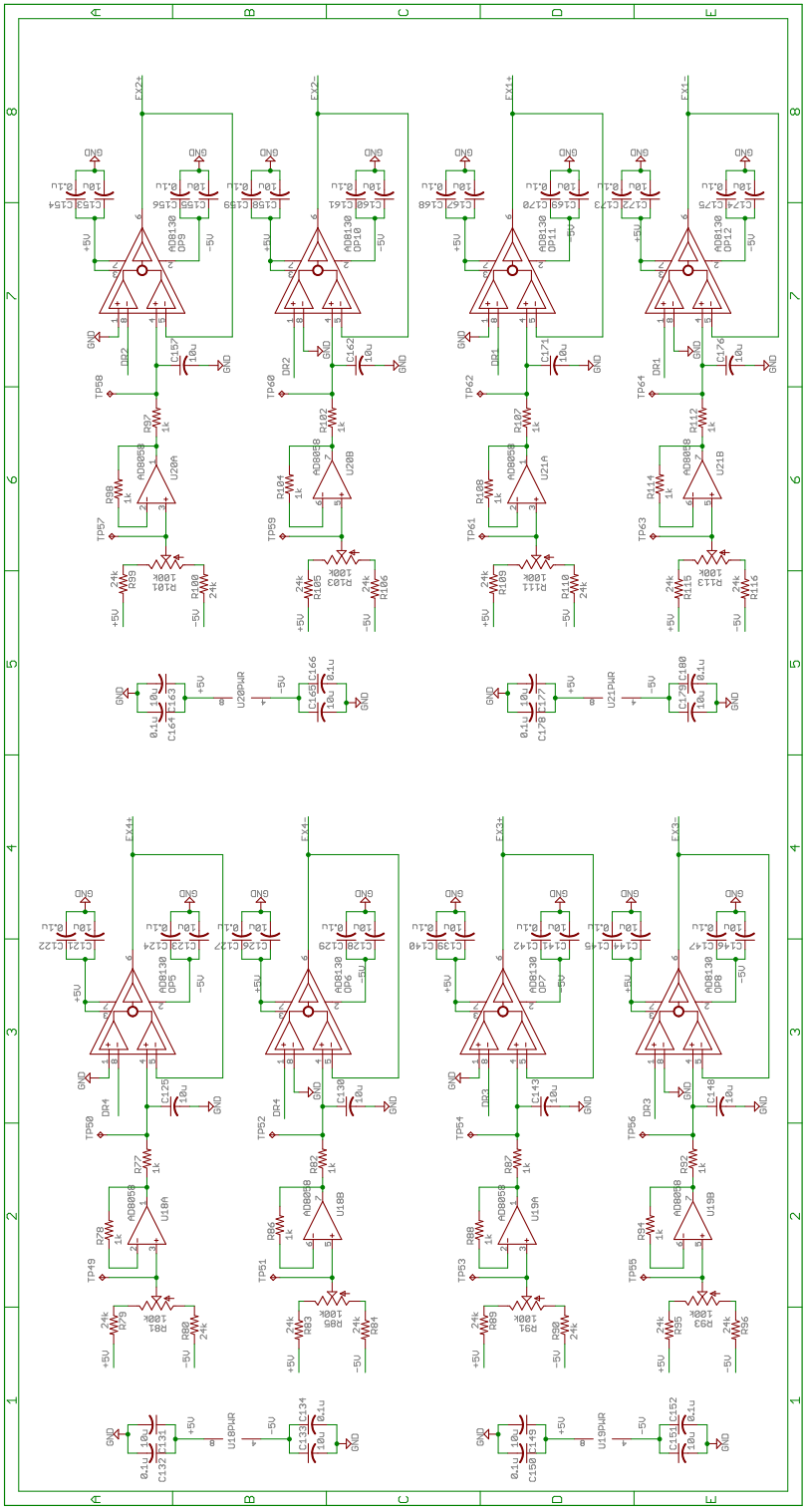

Figure C.4: *Schematic of closed-loop resonant PCB-page 4.*

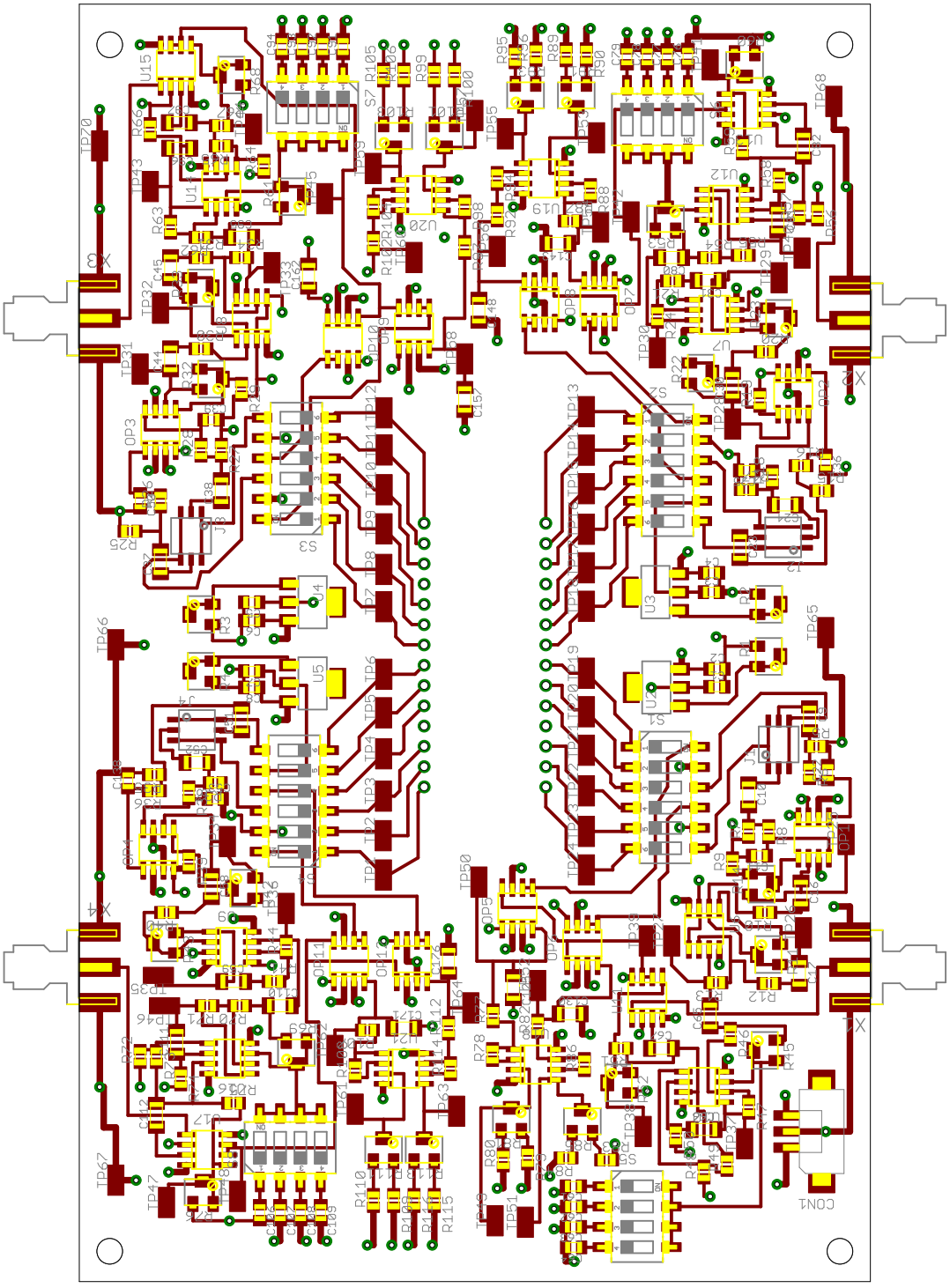

Figure C.5: *PCB layout-front side view.*

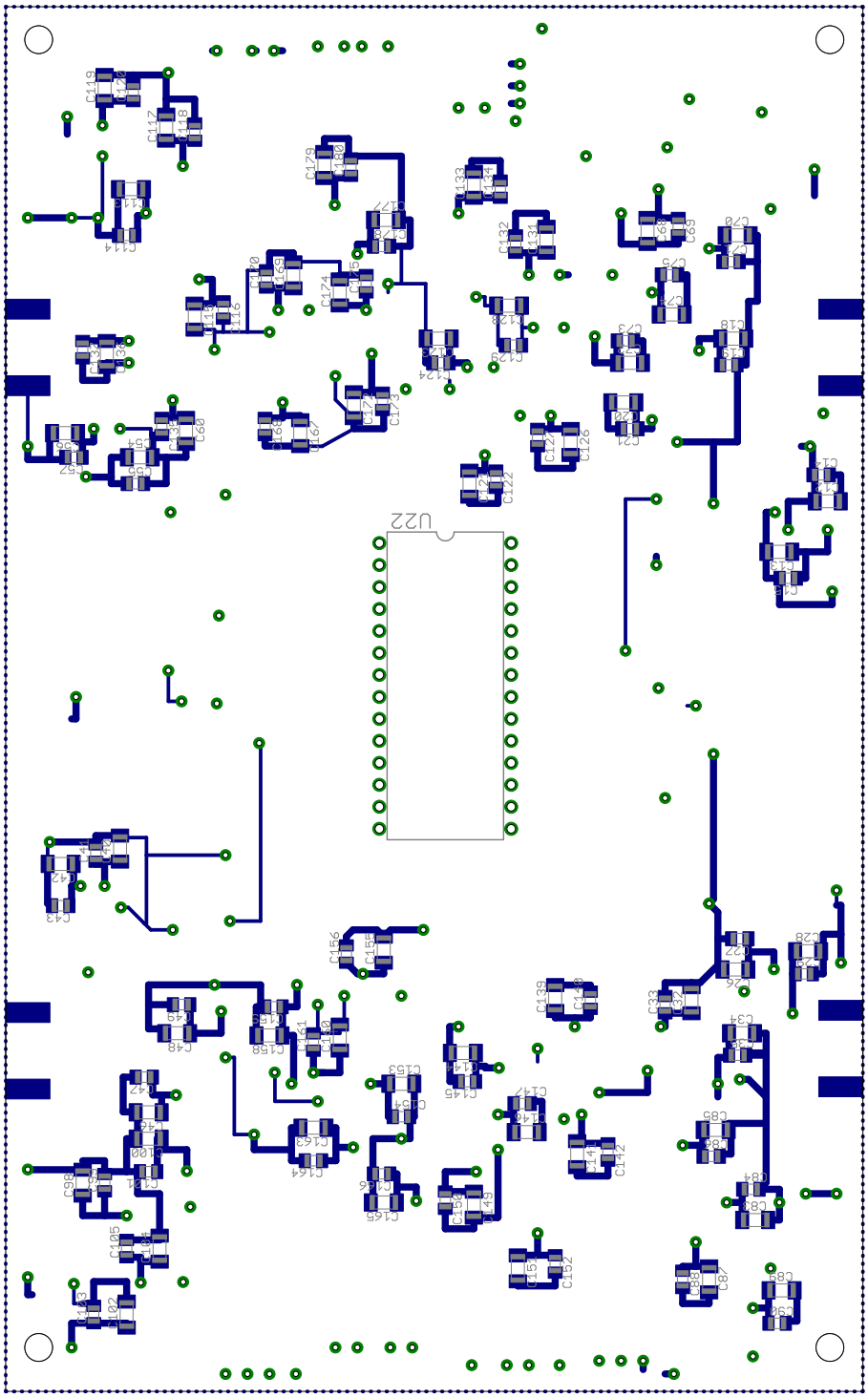

Figure C.6: *PCB layout-back side view.*

REFERENCES

[1] Prabal Dutta et al. “Common Sense”. In: *Proceedings of the 7th ACM Conference on Embedded Networked Sensor Systems - SenSys ’09*. New York, New York, USA: ACM Press, 2009, p. 349. ISBN: 9781605585192. DOI: 10.1145/1644038.1644095.

[2] Clifford K. Ho et al. “Overview of Sensors and Needs for Environmental Monitoring”. In: *Sensors* 5.1 (Feb. 2005), pp. 4–37. ISSN: 1424-8220. DOI: 10.3390/s5010004.

[3] Mervin F. Fingas and Carl E. Brown. “Review of oil spill remote sensing”. In: *Spill Science & Technology Bulletin* 4.4 (Jan. 1997), pp. 199–208. ISSN: 13532561. DOI: 10.1016/S1353-2561(98)00023-1.

[4] Christina Krantz-Rülcker et al. “Electronic tongues for environmental monitoring based on sensor arrays and pattern recognition: a review”. In: *Analytica Chimica Acta* 426.2 (2001), pp. 217–226. ISSN: 00032670. DOI: 10.1016/S0003-2670(00)00873-4.

[5] Patrick Harding and Patricia H. Field. “Breathalyzer® Accuracy in Actual Law Enforcement Practice: A Comparison of Blood- and Breath-Alcohol Results in Wisconsin Drivers”. In: *Journal of Forensic Sciences* 32.5 (Sept. 1987), 11174J. ISSN: 00221198. DOI: 10.1520/JFS11174J.

[6] R. F. Borkenstein and H. W. Smith. “The Breathalyzer and its Applications”. In: *Medicine, Science and the Law* 2.1 (Oct. 1961), pp. 13–22. ISSN: 0025-8024. DOI: 10.1177/002580246200200103.

[7] Peter J Mazzone. “Analysis of volatile organic compounds in the exhaled breath for the diagnosis of lung cancer.” In: *Journal of thoracic oncology : official publication of the International Association for the Study of Lung Cancer* 3.7 (2008), pp. 774–780. ISSN: 1556-1380. DOI: 10.1097/JTO.0b013e31817c7439.

[8] Wolfram Miekisch, Jochen K Schubert, and Gabriele F E Noeldge-Schomburg. “Diagnostic potential of breath analysis–focus on volatile organic compounds.” In: *Clinica chimica acta; international journal of clinical chemistry* 347.1-2 (Sept. 2004), pp. 25–39. ISSN: 0009-8981. DOI: 10.1016/j.cccn.2004.04.023.

[9] Xiaohua Sun, Kang Shao, and Tie Wang. “Detection of volatile organic compounds (VOCs) from exhaled breath as noninvasive methods for cancer diagnosis”. In: *Analytical and Bioanalytical Chemistry* 408.2016 (Apr. 2015), pp. 1–22. ISSN: 16182650. DOI: 10.1007/s00216-015-9200-6.

[10] R. G. Ewing et al. “A critical review of ion mobility spectrometry for the detection of explosives and explosive related compounds”. In: *Talanta* 54.3 (2001), pp. 515–529. ISSN: 00399140. DOI: 10.1016/S0039-9140(00)00565-8.

[11] Sameer Singh and Maneesha Singh. "Explosives detection systems (EDS) for aviation security". In: *Signal Processing* 83.1 (2003), pp. 31–55. ISSN: 01651684. DOI: 10.1016/S0165-1684(02)00391-2.

[12] Adam Hulanicki, Stanislav Glab, and Folke Ingman. "Chemical sensors: definitions and classification". In: *Pure and applied chemistry* 63.9 (1991), pp. 1247–1250.

[13] Faisal I Khan and Aloke Kr. Ghoshal. "Removal of Volatile Organic Compounds from polluted air". In: *Journal of Loss Prevention in the Process Industries* 13.6 (2000), pp. 527–545. ISSN: 09504230. DOI: 10.1016/S0950-4230(00)00007-3.

[14] A. P. Jones. *Indoor air quality and health*. Dec. 1999. DOI: 10.1016/S1352-2310(99)00272-1.

[15] Meggie Hakim et al. "Volatile Organic Compounds of Lung Cancer and Possible Biochemical Pathways". In: *Chemical Reviews* 112.11 (Nov. 2012), pp. 5949–5966. ISSN: 0009-2665. DOI: 10.1021/cr300174a.

[16] Edgar R. Stephens et al. "Reactions of Nitrogen Dioxide and Organic Compounds in Air". In: *Industrial & Engineering Chemistry* 48.9 (Sept. 1956), pp. 1498–1504. ISSN: 0019-7866. DOI: 10.1021/ie51400a036.

[17] OECD. *Air and climate: Air emissions by source*. 2017. DOI: 10.1787/db7b6796-en.

[18] EPA. *EPA's Report on the Environment*. Tech. rep. US Environmental Protecetion Agency, 2015.

[19] J Lelieveld et al. "The contribution of outdoor air pollution sources to premature mortality on a global scale." In: *Nature* 525.7569 (2015), pp. 367–71. ISSN: 1476-4687. DOI: 10.1038/nature15371. arXiv: arXiv:1011.1669v3.

[20] Markku Kulmala. "Atmospheric chemistry: China's choking cocktail". In: *Nature* 526.7574 (Oct. 2015), pp. 497–499. ISSN: 0028-0836. DOI: 10.1038/526497a.

[21] H Guo et al. "Risk assessment of exposure to volatile organic compounds in different indoor environments". In: *Environmental Research* 94.1 (Jan. 2004), pp. 57–66. ISSN: 00139351. DOI: 10.1016/S0013-9351(03)00035-5.

[22] OSHA. *Direct-Reading Instruments*. Tech. rep. United States Environmental Protection Agency, 2017.

[23] L. Mølhave, B Bach, and O F. Pedersen. "Human reactions to low concentrations of volatile organic compounds". In: *Environment International* 12.1-4 (1986), pp. 167–175. ISSN: 01604120. DOI: 10.1016/0160-4120(86)90027-9.

[24] Dimosthenis A. Sarigiannis et al. *Exposure to major volatile organic compounds and carbonyls in European indoor environments and associated health risk*. 2011. DOI: 10.1016/j.envint.2011.01.005.

[25] Sabit Cakmak et al. "Residential exposure to volatile organic compounds and lung function: Results from a population-based cross-sectional survey". In: *Environmental Pollution* 194 (2014), pp. 145–151. ISSN: 18736424. DOI: 10.1016/j.envpol.2014.07.020.

[26] United States Department of Labor. *TABLE Z-1 Limits for Air Contaminants. - 1910.1000 TABLE Z-1 — Occupational Safety and Health Administration*. 2017.

[27] United States Environmental Protection Agency. *Indoor Exposure Product Testing Protocols*. Tech. rep. September. 2015.

[28] Clifford K Ho et al. "Review of Chemical Sensors for In-Situ Monitoring of Volatile Contaminants". In: *Contract* 2001.March (2001), p. 34. DOI: 10.2172/780299.

[29] United States Department of Labor. *Chemical Sampling Information — Toluene — Occupational Safety and Health Administration*. 2017.

[30] United States Department of Labor. *Chemical Sampling Information — Xylene — Occupational Safety and Health Administration*. 2017.

[31] United States Department of Labor. *Chemical Sampling Information — Pentane — Occupational Safety and Health Administration*. 2017.

[32] United States Department of Labor. *Chemical Sampling Information — Hexane (n-Hexane) — Occupational Safety and Health Administration*. 2017.

[33] United States Department of Labor. *Chemical Sampling Information — Ethyl Benzene — Occupational Safety and Health Administration*. 2013.

[34] United States Department of Labor. *Chemical Sampling Information — Chloroform — Occupational Safety and Health Administration*. 2012.

[35] United States Department of Labor. *Chemical Sampling Information — Benzene — Occupational Safety and Health Administration*. 2016.

[36] Spyros P. Karakitsios et al. "Exposure modeling of benzene exploiting passive-active sampling data". In: *Environmental Modeling and Assessment* 15.4 (Aug. 2010), pp. 283–294. ISSN: 14202026. DOI: 10.1007/s10666-009-9206-6.

[37] A. T. James, A. J. P. Martin, and G. H. Smith. "Gas-liquid partition chromatography: the separation and micro-estimation of ammonia and the methylamines." In: *Biochemical Journal,* 52.2 (1952), pp. 238–242. ISSN: 0264-6021.

[38] Keith D. Bartle and Peter Myers. *History of gas chromatography*. Sept. 2002. DOI: 10.1016/S0165-9936(02)00806-3.

[39] Julian W Gardner and Philip N Bartlett. "A brief history of electronic noses". In: *Sensors and Actuators B* (1994), pp. 18–19. ISSN: 09254005. DOI: 10.1016/0925-4005(94)87085-3.

[40] Dirk Lange et al. "Complementary Metal Oxide Semiconductor Cantilever Arrays on a Single Chip: Mass-Sensitive Detection of Volatile Organic Compounds". In: *Analytical Chemistry* 74.13 (July 2002), pp. 3084–3095. ISSN: 0003-2700. DOI: 10.1021/ac011269j.

[41] Andreas Hierlemann et al. "Microfabrication techniques for chemical/biosensors". In: *Proceedings of the IEEE* 91.6 (June 2003), pp. 839–863. ISSN: 0018-9219. DOI: 10.1109/JPROC.2003.813583.

[42] Jiri Janata. "Chemical Sensors". In: *Anal. Chem.* (1990), pp. 33–44.

[43] Andreas Hierlemann and Henry Baltes. “CMOS-based chemical microsensors”. In: *The Analyst* 128.1 (Dec. 2003), pp. 15–28. ISSN: 00032654. DOI: 10.1039/b208563c.

[44] Jiri Janata. *Principles of chemical sensors*. Springer Science & Business Media, 2010.

[45] Luke A Beardslee, Oliver Brand, and Fabien Josse. “Modeling of Resonant Microcantilever Chemical Sensors”. In: *Resonant MEMS*. Ed. by Oliver Brand et al. Weinheim: WILEY-VCH Verlag, 2015. Chap. 15, pp. 355–390. ISBN: 978-3-527-33545-9.

[46] Roberto Trivino et al. “Challenges to embed an electronic nose on a mobile robot”. In: *Proceedings of the 2016 IEEE ANDESCON, ANDESCON 2016*. IEEE, Oct. 2017, pp. 1–4. ISBN: 9781509025312. DOI: 10.1109/ANDESCON.2016.7836251.

[47] W.Patrick Carey. “Multivariate sensor arrays as industrial and environmental monitoring systems”. In: *TrAC Trends in Analytical Chemistry* 13.5 (1994), pp. 210–218. ISSN: 01659936. DOI: 10.1016/0165-9936(94)85041-0.

[48] By Brooke F Connor et al. *Methods of Analysis by the U . S . Geological Survey National Water Quality Laboratory Determination of 86 Volatile Organic Compounds in Water by Gas Chromatography / Mass Spectrometry , Including Detections Less Than Reporting Limits*. Tech. rep. Denver: U.S. Department of the Interior, 1998.

[49] T.A. Bellar and J. J. Lichtenberg. “Determining Volatile Organics at Microgram-per-Litre Levels by Gas Chromatography”. In: *American Water Works Association* 66.12 (1974), pp. 739–744.

[50] Joanna Rudnicka et al. “Determination of volatile organic compounds as potential markers of lung cancer by gas chromatography mass spectrometry versus trained dogs”. In: *Sensors and Actuators B: Chemical* 202 (2014), pp. 615–621. ISSN: 09254005. DOI: 10.1016/j.snb.2014.06.006.

[51] A. G. Bunch et al. “Evaluation of impact of shale gas operations in the Barnett Shale region on volatile organic compounds in air and potential human health risks”. In: *Science of the Total Environment* 468-469 (2014), pp. 832–842. ISSN: 18791026. DOI: 10.1016/j.scitotenv.2013.08.080.

[52] Michael Phillips et al. “Volatile organic compounds in breath as markers of lung cancer: A cross-sectional study”. In: *Lancet* 353.9168 (1999), pp. 1930–1933. ISSN: 01406736. DOI: 10.1016/S0140-6736(98)07552-7.

[53] Michael Phillips. “Method for the collection and assay of volatile organic compounds in breath.” In: *Analytical biochemistry* 247.2 (May 1997), pp. 272–278. ISSN: 0003-2697. DOI: 10.1006/abio.1997.2069.

[54] Yoav Y Broza and Hossam Haick. “Nanomaterial-based sensors for detection of disease by volatile organic compounds”. In: *Nanomedicine* 8.5 (May 2013), pp. 785–806. ISSN: 1743-5889. DOI: 10.2217/nnm.13.64.

[55] Stefan Zimmermann et al. “Miniaturized flame ionization detector for gas chromatography”. In: *Sensors and Actuators, B: Chemical* 83.1-3 (2002), pp. 285–289. ISSN: 09254005. DOI: 10.1016/S0925-4005(01)01060-7.

[56] Kátia Duarte et al. “Direct-reading methods for analysis of volatile organic compounds and nanoparticles in workplace air”. In: *TrAC Trends in Analytical Chemistry* 53 (2014), pp. 21–32. ISSN: 01659936. DOI: 10.1016/j.trac.2013.08.008.

[57] A Jordan et al. “A high resolution and high sensitivity proton-transfer-reaction time-of-flight mass spectrometer (PTR-TOF-MS)”. In: *International Journal of Mass Spectrometry* 286.2-3 (Sept. 2009), pp. 122–128. ISSN: 13873806. DOI: 10.1016/j.ijms.2009.07.005.

[58] Eric Denoyer. “Improving Return on Innovation in Gas Chromatography”. 2017.

[59] Agilent Technologies. *Agilent — Intuvo 9000 GC System*. 2017.

[60] Te-hsuen Tzeng et al. “A Portable Micro Gas Chromatography System for Lung Cancer Associated Volatile Organic Compound Detection”. In: *IEEE Journal of Solid-State Circuits* 51.1 (Jan. 2016), pp. 259–272. ISSN: 0018-9200. DOI: 10.1109/JSSC.2015.2489839.

[61] Christopher John Carron et al. “Cantilever-based resonant microsensors with integrated temperature modulation for transient chemical analysis”. In: *Transducers 2015, 18th International Conference on Solid-State Sensors, Actuators and Microsystems*. 2015, pp. 1511–1514. DOI: 10.1109/TRANSDUCERS.2015.7181223.

[62] Karthik Reddy et al. “Rapid, sensitive, and multiplexed on-chip optical sensors for micro-gas chromatography”. In: *Lab on a Chip* 12.5 (2012), p. 901. ISSN: 1473-0197. DOI: 10.1039/c2lc20922e.

[63] S Zimmermann, S Wischhusen, and J Müller. “Micro flame ionization detector and micro flame spectrometer”. In: *Sensors and Actuators, B: Chemical* 63.3 (2000), pp. 159–166. ISSN: 09254005. DOI: 10.1016/S0925-4005(00)00353-1.

[64] Eric Wapelhorst, Jan Peter Hauschild, and Jörg Müller. “Complex MEMS: a fully integrated TOF micro mass spectrometer”. In: *Sensors and Actuators, A: Physical* 138.1 (2007), pp. 22–27. ISSN: 09244247. DOI: 10.1016/j.sna.2007.04.041.

[65] F. J. Santos and M. T. Galceran. *The application of gas chromatography to environmental analysis*. Sept. 2002. DOI: 10.1016/S0165-9936(02)00813-0.

[66] Jing Liu et al. “Smart multi-channel two-dimensional micro-gas chromatography for rapid workplace hazardous volatile organic compounds measurement”. In: *Lab on a Chip* 13.5 (2013), pp. 818–825. ISSN: 1473-0189. DOI: 10.1039/C2LC41159H.

[67] Xudong Fan et al. “Portable multi-dimensional gas chromatography device for rapid field analysis of chemical compounds”. In: *Transducers 2017*. 2017.

[68] Xudong Fan et al. “Portable Multi-Dimensional Gas Chromatography Device For Rapid Field Analysis Of Chemical Compounds”. In: *Transducers 2017*. IEEE, June 2017, pp. 654–659. ISBN: 9781538627327. DOI: 10.1109/TRANSDUCERS.2017.7994134.

[69] Jing Liu et al. “Demonstration of motionless Knudsen pump based micro-gas chromatography featuring micro-fabricated columns and on-column detectors”. In: *Lab on a Chip* 11.20 (2011), p. 3487. ISSN: 1473-0197. DOI: 10.1039/c1lc20511k.

[70] Andreas Hierlemann. “CMOS-based Chemical Sensors”. In: *Advanced Micro and Nanosystems. Vol. 2. CMOS-MEMS*. Ed. by Henry Baltes et al. Weinheim: WILEY-VCH Verlag, 2005. Chap. 7, pp. 335–390. ISBN: 3-527-31080-0.

[71] Patrick Getz et al. “Transient analysis of analyte desorption due to thermal cycling with varying pulse duration”. In: *13th International Workshop on Nanomechanical Sensing*. Delft, 2016.

[72] Robert Bogue. “Recent developments in MEMS sensors : a review of applications, markets and technologies”. In: *Sensor Review* 33.15 (2014), pp. 300–304. DOI: 10.1108/SR-05-2013-678.

[73] Oliver Brand and Gary K. Fedder. *CMOS-MEMS: Advanced micro and nanosystems*. Vol. 2. 2008, pp. 1–595. ISBN: 9783527616718. DOI: 10.1002/9783527616718.

[74] Henry Baltes and Dirk Lance. “The electronic nose in Lilliput”. In: *IEEE Spectrum* 35.9 (1998), pp. 35–38. ISSN: 00189235. DOI: 10.1109/6.715182.

[75] J.S. Suehle et al. “Tin oxide gas sensor fabricated using CMOS micro-hotplates and\nin-situ processing”. In: *IEEE Electron Device Letters* 14.3 (Mar. 1993), pp. 118–120. ISSN: 0741-3106. DOI: 10.1109/55.215130.

[76] Christoph Hagleitner et al. “CMOS single-chip gas detection system comprising capacitive, calorimetric and mass-sensitive microsensors”. In: *IEEE Journal of Solid-State Circuits*. Vol. 37. Dec. 2002, pp. 1867–1878. ISBN: 0-7803-7335-9. DOI: 10.1109/JSSC.2002.804359.

[77] Alireza Mahdavifar et al. “Transient thermal response of micro-thermal conductivity detector (TCD) for the identification of gas mixtures: An ultra-fast and low power method”. In: *Microsystems & Nanoengineering* 1 (2015), p. 15025. ISSN: 2055-7434. DOI: 10.1038/micronano.2015.25.

[78] Alina Segal et al. “Development of membrane extraction with a sorbent interface-micro gas chromatography system for field analysis”. In: *Journal of Chromatography A* 873.1 (Mar. 2000), pp. 13–27. ISSN: 00219673. DOI: 10.1016/S0021-9673(99)01318-7.

[79] Siyka I Shopova et al. “On-column micro gas chromatography detection with capillary-based optical ring resonators”. In: *Analytical Chemistry* 80.6 (2008), pp. 2232–2238. ISSN: 00032700. DOI: 10.1021/ac702389x.

[80] Jianhai Sun et al. “An improved photoionization detector with a micro gas chromatography column for portable rapid gas chromatography system”. In: *Sensors and Actuators, B: Chemical* 188 (2013), pp. 513–518. ISSN: 09254005. DOI: 10.1016/j.snb.2013.07.066.

[81] Shree Narayanan, Gary Rice, and Masoud Agah. “A micro-discharge photoionization detector for micro-gas chromatography”. In: *Microchimica Acta* 181.5-6 (Apr. 2014), pp. 493–499. ISSN: 14365073. DOI: 10.1007/s00604-013-1146-9.

[82] Apoorva Garg et al. “Zebra GC: A mini gas chromatography system for trace-level determination of hazardous air pollutants”. In: *Sensors and Actuators, B: Chemical* 212 (2015), pp. 145–154. ISSN: 09254005. DOI: 10.1016/j.snb.2014.12.136.

[83] S Zampolli et al. “Real-time monitoring of sub-ppb concentrations of aromatic volatiles with a MEMS-enabled miniaturized gas-chromatograph”. In: *Sensors and Actuators, B: Chemical* 141.1 (2009), pp. 322–328. ISSN: 09254005. DOI: 10.1016/j.snb.2009.06.021.

[84] Cheng Chen et al. “A wireless hybrid chemical sensor for detection of environmental volatile organic compounds”. In: *IEEE Sens. J* 13.5 (May 2013), pp. 1748–1755. ISSN: 1530-437X. DOI: 10.1109/JSEN.2013.2239472.A.

[85] William R. Collin et al. “Microfabricated gas chromatograph for rapid, trace-level determinations of gas-phase explosive marker compounds”. In: *Analytical Chemistry* 86.1 (Jan. 2014), pp. 655–663. ISSN: 00032700. DOI: 10.1021/ac402961t.

[86] Henry Baltes. “CMOS as sensor technology”. In: *Sensors and Actuators: A. Physical* 37-38.C (1993), pp. 51–56. ISSN: 09244247. DOI: 10.1016/0924-4247(93)80011-5.

[87] Marc J Madou. *Fundamentals of microfabrication : the science of miniaturization / Marc J. Madou*. 2nd ed. Boca Raton : CRC Press, c2002. 2nd ed., 2002. ISBN: 0849308267 9780849308260.

[88] Andreas Hierlemann et al. “Application-specific sensor systems based on CMOS chemical microsensors”. In: *Sensors and Actuators, B: Chemical* 70.1-3 (2000), pp. 2–11. ISSN: 09254005. DOI: 10.1016/S0925-4005(00)00546-3.

[89] Ying Dong et al. “Characterization of the gas sensors based on polymer-coated resonant microcantilevers for the detection of volatile organic compounds”. In: *Analytica Chimica Acta* 671.1 (2010), pp. 85–91. ISSN: 00032670. DOI: 10.1016/j.aca.2010.05.007.

[90] Bob Henderson. “Gas Detection for VOC Measurement”. In: *Occupational Health & Safety* (Oct. 2004).

[91] Hongyu Ma, Enjie Ding, and Wenjuan Wang. “Power reduction with enhanced sensitivity for pellistor methane sensor by improved thermal insulation packaging”. In: *Sensors and Actuators, B: Chemical* 187 (Oct. 2013), pp. 221–226. ISSN: 09254005. DOI: 10.1016/j.snb.2012.10.121.

[92] Konrad Maier, Andreas Helwig, and Gerhard Müller. "Towards MEMS Pellistor Spectrometers". In: *Procedia Engineering* 120 (2015), pp. 142–145. ISSN: 18777058. DOI: 10.1016/j.proeng.2015.08.587.

[93] Sampath Kommandur et al. "A microbridge heater for low power gas sensing based on the 3-Omega technique". In: *Sensors and Actuators, A: Physical* 233 (2015), pp. 231–238. ISSN: 09244247. DOI: 10.1016/j.sna.2015.07.011.

[94] V. Palmisano et al. "Evaluation of selectivity of commercial hydrogen sensors". In: *International Journal of Hydrogen Energy*. Vol. 39. 35. 2014, pp. 20491–20496. DOI: 10.1016/j.ijhydene.2014.03.251.

[95] Shailesh Pawar et al. "Fabrication of Nanocrystalline TiO2 Thin Film Ammonia Vapor Sensor". In: *Journal of Sensor Technology* 01.March (2011), pp. 9–16. ISSN: 2161-122X. DOI: 10.4236/jst.2011.11002.

[96] Ruiqing Xing et al. "Preparation and Gas Sensing Properties of In2O3/Au Nanorods for Detection of Volatile Organic Compounds in Exhaled Breath." In: *Scientific reports* 5.October 2014 (2015), p. 10717. ISSN: 2045-2322. DOI: 10.1038/srep10717.

[97] Kwan Ting Ng, Farid Boussaid, and Amine Bermak. "A CMOS single-chip gas recognition circuit for metal oxide gas sensor arrays". In: *IEEE Transactions on Circuits and Systems I: Regular Papers* 58.7 (July 2011), pp. 1569–1580. ISSN: 15498328. DOI: 10.1109/TCSI.2011.2143090.

[98] A Mirzaei, S G Leonardi, and G Neri. *Detection of hazardous volatile organic compounds (VOCs) by metal oxide nanostructures-based gas sensors: A review*. 2016. DOI: 10.1016/j.ceramint.2016.06.145.

[99] Xiao Liu et al. "A Survey on Gas Sensing Technology". In: *Sensors* 12.7 (2012), pp. 9635–9665. ISSN: 1424-8220. DOI: 10.3390/s120709635. arXiv: 1305.7427.

[100] B T Raut et al. "Novel method for fabrication of polyaniline-CdS sensor for H2S gas detection". In: *Measurement: Journal of the International Measurement Confederation* 45.1 (2012), pp. 94–100. ISSN: 02632241. DOI: 10.1016/j.measurement.2011.09.015.

[101] J.-J. Su et al. "Assessing polymer sorption kinetics using micromachined resonators". English. In: *2011 16th International Solid-State Sensors, Actuators and Microsystems Conference*. IEEE, June 2011, pp. 1420–1423. ISBN: 978-1-4577-0157-3. DOI: 10.1109/TRANSDUCERS.2011.5969584.

[102] Sanjay V. Patel et al. "Chemicapacitive microsensors for volatile organic compound detection". In: *Sensors and Actuators B: Chemical* 96.3 (2003), pp. 541–553. ISSN: 09254005. DOI: 10.1016/S0925-4005(03)00637-3.

[103] T. Boltshauser and H. Baltes. "Capacitive humidity sensors in SACMOS technology with moisture absorbing photosensitive polyimide". In: *Sensors and Actuators: A. Physical* 26.1-3 (Mar. 1991), pp. 509–512. ISSN: 09244247. DOI: 10.1016/0924-4247(91)87041-Z.

[104] C. Cornila et al. “Capacitive sensors in CMOS technology with polymer coating”. In: *Sensors and Actuators: B. Chemical* 25.1-3 (Apr. 1995), pp. 357–361. ISSN: 09254005. DOI: 10.1016/0925-4005(95)85080-5.

[105] Robert Blue and Deepak Uttamchandani. *Chemicapacitors as a versatile platform for miniature gas and vapor sensors*. Feb. 2017. DOI: 10.1088/1361-6501/28/2/022001.

[106] Tahereh Arezoo Emadi et al. “Polymer-based chemicapacitor sensor for 1-octanol and relative humidity detections at different temperatures and frequencies”. In: *IEEE Sensors Journal* 13.2 (Feb. 2013), pp. 519–527. ISSN: 1530437X. DOI: 10.1109/JSEN.2012.2220760.

[107] Christopher John Carron. “System-level approaces for improving performance of cantilever-based chemical sensors”. PhD thesis. Georgia Institute of Technology, 2015.

[108] Edward T Zellers and Mingwei Han. “Effects of Temperature and Humidity on the Performance of Polymer-Coated Surface Acoustic Wave Vapor Sensor Arrays”. In: *Analytical Chemistry* 68.14 (1996), pp. 2409–2418. ISSN: 0003-2700.

[109] Jay W Grate. “Acoustic wave microsensor arrays for vapor sensing”. In: *Chemical Reviews* 100.7 (2000), pp. 2627–2648. ISSN: 00092665. DOI: 10.1021/cr980094j.

[110] Jay W Grate, Stephen J Martin, and Richard M White. “Acoustic Wave Microsensors”. In: *Analytical Chemistry* 65.21 (1993), 940A–948A. ISSN: 0003-2700. DOI: 10.1021/ac00069a728.

[111] M S Nieuwenhuizen and A J Nederlof. “A silicon-based SAW chemical sensor for NO 2 by applying a silicon nitride passivation layer”. In: *Sensors and Actuators B: Chemical* 9.3 (1992), pp. 171–176. ISSN: 0925-4005.

[112] T. Thundat et al. “Vapor Detection Using Resonating Microcantilevers”. In: *Analytical Chemistry* 67.3 (Feb. 1995), pp. 519–521. ISSN: 0003-2700. DOI: 10.1021/ac00099a006.

[113] Roberto Raiteri et al. “Micromechanical cantilever-based biosensors”. In: *Sensors and Actuators B: Chemical* 79.2-3 (Oct. 2001), pp. 115–126. ISSN: 09254005. DOI: 10.1016/S0925-4005(01)00856-5.

[114] Genki Yoshikawa et al. “Sub-ppm detection of vapors using piezoresistive microcantilever array sensors.” In: *Nanotechnology* 20.1 (Jan. 2009), p. 015501. ISSN: 0957-4484. DOI: 10.1088/0957-4484/20/1/015501.

[115] F. M. Battiston et al. “A chemical sensor based on a microfabricated cantilever array with simultaneous resonance-frequency and bending readout”. In: *Sensors and Actuators, B: Chemical* 77.1-2 (2001), pp. 122–131. ISSN: 09254005. DOI: 10.1016/S0925-4005(01)00683-9.

[116] Larry Senesac and Thomas G. Thundat. *Nanosensors for trace explosive detection*. 2008. DOI: 10.1016/S1369-7021(08)70017-8.

[117] Andreas Hierlemann et al. “Effective use of molecular recognition in gas sensing: Results from acoustic wave and in situ FT-IR measurements”. In: *Analytical Chemistry* 71.15 (1999), pp. 3022–3035. ISSN: 0003-2700. DOI: 10.1021/AC981311J.

[118] B. H. Kim et al. “Multicomponent analysis and prediction with a cantilever array based gas sensor”. In: *Sensors and Actuators, B: Chemical* 78.1-3 (2001), pp. 12–18. ISSN: 09254005. DOI: 10.1016/S0925-4005(01)00785-7.

[119] H P Lang et al. “An Artificial Nose Based on Microcantilever Array Sensors”. In: *Journal of Physics: Conference Series* 61.1 (Mar. 2007), pp. 663–667. ISSN: 1742-6588. DOI: 10.1088/1742-6596/61/1/133.

[120] A.S. Pavluchenko et al. “Estimation of multicomponent organic solvent vapor mixture composition with electroconducting polymer chemiresistors”. In: *Sensors and Actuators B: Chemical* 232 (Sept. 2016), pp. 203–218. ISSN: 09254005. DOI: 10.1016/j.snb.2016.03.111.

[121] Andreas Hierlemann et al. “Pattern Recognition and Multicomponent Analysis”. In: *Sensors Update* 2.1 (Oct. 1996), pp. 119–180. ISSN: 1432-2404. DOI: 10.1002/1616-8984(199610)2:1<119::aid-seup119>3.0.co;2-6.

[122] U Durig et al. “”Millipede” - an AFM data storage system at the frontier of nanotribology”. In: *Tribology Letters* 9.1-2 (2000), pp. 25–32. ISSN: 10238883. DOI: 10.1023/A:1018844124754.

[123] Philip S Waggoner and Harold G Craighead. “Micro- and nanomechanical sensors for environmental, chemical, and biological detection.” en. In: *Lab on a chip* 7.10 (Oct. 2007), pp. 1238–55. ISSN: 1473-0197. DOI: 10.1039/b707401h.

[124] Thomas Thundat and Eric Wachter. *Microcantilever sensor*. 1995.

[125] T Thundat, P I Oden, and R J Warmack. “Microcantilever sensors”. In: *Microscale Thermophysical Engineering* 1 (July 1997). ISSN: 1089-3954. DOI: 10.1080/108939597200214.

[126] Oliver Brand and Henry Baltes. “Micromachined Resonant Sensors an Overview”. In: *Sensors Update* 4.1 (Aug. 1998), pp. 3–51. ISSN: 1432-2404. DOI: 10.1002/1616-8984(199808)4:1<3::AID-SEUP3>3.0.CO;2-T.

[127] Luke A Beardslee et al. “On the relative sensitivity of mass-sensitive chemical microsensors”. In: *2011 16th International Solid-State Sensors, Actuators and Microsystems Conference, TRANSDUCERS’11*. IEEE, June 2011, pp. 1112–1115. ISBN: 9781457701573. DOI: 10.1109/TRANSDUCERS.2011.5969290.

[128] J P Cleveland et al. “A nondestructive method for determining the spring constant of cantilevers for scanning force microscopy”. In: *Review of Scientific Instruments* 64.2 (1993), pp. 403–405. ISSN: 00346748. DOI: 10.1063/1.1144209.

[129] Mo Li, H X Tang, and M L Roukes. “Ultra-sensitive NEMS-based cantilevers for sensing, scanned probe and very high-frequency applications”. In: *Nature nanotechnology* 2.2 (2007), pp. 114–20. ISSN: 1748-3395. DOI: 10.1038/nnano.2006.208.

[130] M Maute et al. “Detection of volatile organic compounds (VOCs) with polymer-coated cantilevers”. In: *Sensors and Actuators B: Chemical* 58.1-3 (Sept. 1999), pp. 505–511. ISSN: 09254005. DOI: 10.1016/S0925-4005(99)00110-0.

[131] Dirk Lange et al. “CMOS chemical microsensors based on resonant cantilever beams”. In: *Conference on Smart Structures and Materials 1998*. Ed. by Vijay K. Varadan et al. Vol. 3328. Zurich: International Society for Optics and Photonics, July 1998, pp. 233–243. ISBN: 0277786X. DOI: 10.1117/12.320174.

[132] K Naeli and O Brand. “Cancellation of environmental effects in resonant mass sensors based on resonance mode and effective mass”. In: *Rev Sci Instrum* 80.6 (2009), p. 63903. DOI: 10.1063/1.3143567.

[133] Agilent Technologies. *Gas Chromatographs*. Tech. rep. Agilent Technologies, 2002, p. 60.

[134] Adrian M Kummer, Thomas P Burg, and Andreas Hierlemann. “Transient signal analysis using complementary metal oxide semiconductor capacitive chemical microsensors”. In: *Analytical Chemistry* 78.1 (2006), pp. 279–290. ISSN: 00032700. DOI: 10.1021/ac051430g.

[135] Naoki Matsunaga et al. “Diffusion equation-based study of thin film semiconductor gas sensor-response transient”. In: *Sensors and Actuators B: Chemical* 83 (2002). DOI: 10.1016/S0925-4005(01)01043-7.

[136] Woodfin V. Ligon and Marcia C. George. “Analysis of volatile constituents in commercial polymers by direct thermal desorption and gas chromatography-mass spectrometry”. In: *Journal of Polymer Science: Polymer Chemistry Edition* 16.10 (Oct. 1978), pp. 2703–2709. ISSN: 03606376. DOI: 10.1002/pol.1978.170161029.

[137] John C Little, Alfred T Hodgson, and Ashok J Gadgil. “Modeling emissions of volatile organic compounds from new carpets”. In: *Atmospheric Environment* 28.2 (1994), pp. 227–234. ISSN: 13522310. DOI: 10.1016/1352-2310(94)90097-3.

[138] A. Bodalal, J.S. Zhang, and E.G. Plett. “A method for measuring internal diffusion and equilibrium partition coefficients of volatile organic compounds for building materials”. In: *Building and Environment* 35.2 (2000), pp. 101–110. ISSN: 03601323. DOI: 10.1016/S0360-1323(99)00005-0.

[139] Steven S. Cox, John C. Little, and Alfred T. Hodgson. “Measuring concentrations of volatile organic compounds in vinyl flooring.” In: *Journal of the Air & Waste Management Association (1995)* 51.8 (Aug. 2001), pp. 1195–201. ISSN: 1096-2247. DOI: 10.1080/10473289.2001.10464349.

[140] Christopher John Carron et al. “Cantilever-based resonant gas sensors with integrated recesses for localized sensing layer deposition”. In: *2013 IEEE SENSORS*. IEEE, Nov. 2013, pp. 1–4. ISBN: 978-1-4673-4642-9. DOI: 10.1109/ICSENS.2013.6688335.

[141] Andreas Koll. “CMOS capacitive chemical microsystems for volatile organic compounds”. PhD thesis. Swiss Federal Institute of Technology Zurich, 1999. ISBN: 3-89649-524-0. DOI: 10.3929/ethz-a-003925538.

[142] Vladimir. Majer et al. *Enthalpies of vaporization of organic compounds : a critical review and data compilation*. Blackwell Scientific, 1985, p. 300. ISBN: 0632015292.

[143] Andreas Hierlemann. “Massensensitive detektion flüchtiger organischer substanzen mit modifizierten polysiloxanen”. PhD thesis. Eberhard-Karls-Universität Tübingen, 1996.

[144] James S Chickos and William E Acree. *Enthalpies of vaporization of organic and organometallic compounds, 1880-2002*. 2003. DOI: 10.1063/1.1529214.

[145] J L Duda et al. “Prediction of diffusion coefficients for polymer-solvent systems”. In: *AIChE Journal* 28.2 (1982), pp. 279–285. DOI: 10.1002/aic.690280217.

[146] A. Koll et al. “Micromachined CMOS calorimetric chemical sensor with on-chip low noise amplifier”. In: *Technical Digest. IEEE International MEMS 99 Conference. Twelfth IEEE International Conference on Micro Electro Mechanical Systems (Cat. No.99CH36291)*. IEEE, 1999, pp. 547–551. ISBN: 0-7803-5194-0. DOI: 10.1109/MEMSYS.1999.746887.

[147] Tom Harner and Terry F Bidleman. “Measurements of OctanolAir Partition Coefficients for Polychlorinated Biphenyls”. In: *Journal of Chemical & Engineering Data* 41.4 (1996), pp. 895–899. ISSN: 0021-9568. DOI: 10.1021/je960097y.

[148] Tom Harner and Terry F Bidleman. “Measurement of OctanolAir Partition Coefficients for Polycyclic Aromatic Hydrocarbons and Polychlorinated Naphthalenes”. In: *Journal of Chemical & Engineering Data* 43.1 (1998), pp. 40–46. ISSN: 0021-9568. DOI: 10.1021/je970175x.

[149] W.E. Acree and J.S. Chickos. “Phase Transition Enthalpy Measurements of Organic and Organometallic Compounds”. In: *NIST Chemistry WebBook, NIST Standard Reference Database Number 69*. Ed. by P.J. Linstrom and W.G. Mallard. 69th ed. Gaithersburg, MD: National Institute of Standards and Technology, 2016. Chap. Phase Tran.

[150] John M Zielinski and J L Duda. “Predicting Polymer / Solvent Diffusion Coefficients Using Free - Volume Theory”. In: *AIChE Journal* 38.3 (1992). DOI: 10.1002/aic.690380309.

[151] Luke A Beardslee et al. “Liquid-phase chemical sensing using lateral mode resonant cantilevers”. In: *Analytical Chemistry* 82.18 (2010), pp. 7542–7549. ISSN: 00032700. DOI: 10.1021/ac1010102.

[152] Stuart B Truax et al. “Mass-Sensitive Detection of Gas-Phase Volatile Organics Using Disk Microresonators”. In: *Analytical Chemistry* 83.9 (2011), pp. 3305–3311. DOI: 10.1021/ac1029902.

[153] Luke A Beardslee et al. “Detection of anti-IgG using cantilever-type resonant microstructures vibrating in in-plane flexural modes”. In: *Proceedings of IEEE Sensors*. IEEE, Oct. 2012, pp. 1–4. ISBN: 9781457717659. DOI: 10.1109/ICSENS.2012.6411338.

[154] Jae Hyeong Seo et al. “Temperature compensation method for resonant microsensors based on a controlled stiffness modulation”. In: *Journal of Applied Physics* 104.1 (2008), p. 14911. DOI: 10.1063/1.2952050.

[155] Isabelle Dufour et al. “Effect of Coating Viscoelasticity on Quality Factor and Limit of Detection of Microcantilever Chemical Sensors”. In: *IEEE Sensors Journal* 7.2 (Feb. 2007), pp. 230–236. ISSN: 1530-437X. DOI: 10.1109/JSEN.2006.888600.

[156] D. Allan et al. “Standard terminology for fundamental frequency and time metrology”. In: *Proceedings of the 42nd Annual Frequency Control Symposium, 1988.* IEEE, 1988, pp. 419–425. DOI: 10.1109/FREQ.1988.27634.

[157] MathWorks Inc. *Train models to classify data using supervised machine learning - MATLAB - MathWorks Benelux*. 2018.